A comprehensive high resolution 3D *P*- and *S*-wave velocity model for the Alpine mountain chain using local earthquake data

Zur Erlangung des akademischen Grades eines

DOKTORS DER NATURWISSENSCHAFTEN (Dr. rer. nat.)

von der KIT-Fakultät für Physik des
Karlsruher Instituts für Technologie (KIT)

genehmigte

DISSERTATION

von

M.Sc. Benedikt Braszus

Tag der mündlichen Prüfung:	26.07.2024
Referent:	Prof. Dr. Andreas Rietbrock
Korreferent:	apl. Prof. Dr. Joachim Ritter

Abstract

Between 2016 and 2022 the dense and uniformly spaced AlpArray Seismic Network as part of the AlpArray-4DMB project provided an unprecedented seismic data set for the Greater Alpine region (GAR) with an average broad-band station spacing of ≈50 km. Complementary deployments such as the EASI, CIFALPS2 and SWATH-D networks provided further increased spatial sampling of ground motions in regions of special research interest.

Contemporary, the revolutionary development of machine learning applications in key societal and economic sectors such as finance, medicine and transport was accompanied by ground-breaking progress in AI based seismological signal processing.

This thesis combines the unique seismic data set from the GAR with cutting-edge neural network based seismic picking algorithms to calculate the first comprehensive high resolution crustal 3D *P*- and *S*-wave velocity model for the GAR based on Local Earthquake Tomography.

Research questions directly linked to this study cover the benchmarking of the most commonly used neural network based seismic picking algorithms against a manually picked high precision reference catalog and their applicability to waveforms recorded at epicentral distances of up to 1000 km. I show that the deep neural network *PhaseNet* is most suitable for this study and that it performs as consistently as human analysts. In terms of number of detected phases it significantly outperforms manual picking approaches especially on seismic traces recorded at larger distances with lower signal-to-noise ratio. In order to remove outliers in the automatically generated arrival time catalog, I developed a data-driven pre-inversion pick selection method which requires only minor manual supervision and is applicable throughout the crustal triplication zone. I relocate 384 events with local magnitudes $M_L \geq 2.5$ while simultaneously inverting for the first comprehensive 1D *P*- and *S*-wave velocity model of the GAR including station correction terms. Results from the well established *VELEST* and the recently developed probabilistic *Markov chain Monte Carlo (McMC)* algorithms are within their respective uncertainty range and generally agree with previous models of the region. By comparing my event locations to results from two recent studies, I quantify the hypocentre accuracy as ≈2.0 km in horizontal and ≈6.0 km in vertical direction when using a 1D velocity model including station corrections. Subsequently, I invert for the 3D *P*- and *S*-wave velocity structure of the GAR and northern Apennines using the *SIMUL2023* inversion algorithm. This inversion is based on 173,841 *P*- and 68,967 *S*-phase arrivals from 2553 events with $M_L \geq 1.5$ recorded at 989 seismic broad-band stations.

Main features of the 3D model are in good agreement with previous active as well as passive seismic studies of the region. In the uppermost crust the foreland basins North and South of the Alpine arc are

showing up as prominent low velocity anomalies. The crustal root is deepest in the Western and Central Alps while consistently shallowing towards the East which matches the previously proposed model of eastwards lateral extrusion of crustal material. A striking novel feature is the consistent presence of anomalously low velocities at mid crustal depths throughout the Western and Central Alps which I interpret as stacked European and Adriatic crust. Furthermore, the seismic signature of the Adriatic indenter indicates a thickened and deformed crust in its northern part, while the southern part appears to be mainly undeformed.

The final 3D velocity model and the arrival time data base including pick probabilities will be made available publicly and thus will contribute to a wide range of future geophysical studies within the region. The inferred crustal velocity structure will be crucial to refine the resolution of related studies such as teleseismic tomographies of the upper mantle and receiver functions investigating the precise topography of the crust-mantle boundary (Moho) across the orogen. Until now these studies are using a combination of simplified or heterogeneously processed crustal models. This leads to ambiguities in their images of the configuration of subducted lithosphere beneath the mountain chain and thus results in major disagreement in key questions regarding the evolution of the Alpine orogen such as the potential presence of a slab tear or detachment and a subduction polarity switch along the Alpine arc.

Contents

1. Introduction

1.1. AlpArray & 4DMB project

The presented thesis has been conducted within the scope of the Priority Programme "Mountain Building Processes in Four Dimensions (MB-4D)" (*http://www.spp-mountainbuilding.de/; last accessed 10th June 2024*) funded by the German Science foundation which has been part of the European AlpArray (*http://www.alparray.ethz.ch/; last accessed 10th June 2024*) research initiative. Within AlpArray a wide interdisciplinary range of geoscientifical methods were applied to collaboratively answer the most debated questions regarding the orogenesis of the European Alps and its connection to underlying mantle dynamics. In order to link surface observations to past and present processes at depth, the AlpArray Seismic Network (AASN) (AlpArray Seismic Network, 2015) consisting of over 600 seismic broadband stations has been installed from 2015-2022 as a densification of the permanent networks which are mainly run by national agencies. Additionally, complementary networks such as the EASI (AlpArray Seismic Network, 2014) and SWATH-D (Heit et al., 2021) have been set up to target research questions with a more local focus in even greater detail. At the same time, the CIFALPS2 network (Zhao et al., 2018) was recording along a transect through the Western Alps. In combination, this yields a waveform data set of unprecedented quality for the region and led to numerous geophysical studies improving the understanding of seismic activity, separation of crustal tectonic units and the configuration of subducted plates in the Earth's mantle.

1.2. Goals & deliverables of this study

The main goal of this study is the combination of the extraordinary seismic data set of the AlpArray project with recent rapid advances in machine learning algorithms to compute the first comprehensive high resolution 3D *P*- and *S*-wave travel time tomography of the Greater Alpine region. A further goal is the compilation of an AI based accurate *P*- and *S*-phase arrival time data base including far distance observations of up to 1000 km for stations of the AASN including the associated raw waveforms. Additionally, the seismic events will be consistently relocated and published as an earthquake catalog including uncertainties.

The main deliverable to other studies within the AlpArray project and for future research is the first comprehensive 3D *P*- and *S*-wave crustal velocity model of the entire Alpine arc and its foreland regions. This will be of use for various future applications such as teleseismic tomographies, receiver function studies and full waveform inversion. Teleseismic tomographies are imaging the upper and mid-mantle

which is the area they are most sensitive to. Therefore, they require accurate crustal correction terms based on a crustal velocity model to prevent vertical smearing of shallow anomalies which they are not able to resolve. A recent teleseimic tomography by Paffrath et al. (2021) had to combine two different crustal models of varying resolution and parametrization. My model is uniformly processed, based on significantly more data and covers the entire Alpine arc. Thus, it will help to obtain more accurate crustal corrections and sharpen teleseismic tomography images resolving the configuration of subducted plates and plate fragments in the mantle. The location of these subducted plates is of high importance for unravelling the history of Alpine orogenesis and answering the intensely debated question of a subduction polarity switch.
Moreover, receiver function studies require an accurate image of crustal velocities to migrate imaged velocity contrasts along interfaces to the correct depth and therefore will benefit from this model as well. Additionally, my model will serve as an improved starting model for full waveform inversion applications. Instead of merely the first arrival, this method uses the information along the entire seismic trace and hence has the potential to substantially increase model resolution.
Aside from contributing to future seismic studies, my well resolved 3D model directly addresses geological research questions regarding the crustal velocity structure of the GAR. Are there large scale differences in the velocity structure along the mountain chain, especially at mid and lower crustal depths ? Can the seismic signature of the Adriatic indenter be resolved further ?

1.3. Dissertation Outline

The following gives an outline of this work. Chapter 2 summarizes the geological evolution of the Greater Alpine region and describes the present seismotectonic setting. In chapter 3, I elaborate on the applied data processing steps and inversion methodology. I discuss the assessment of machine learning algorithms for seismic phase picking and present a novel technique for data-driven removal of outliers from the automatic arrival time catalog. Furthermore, I introduce the fundamental concept and challenges of Local Earthquake Tomography (LET) such as the coupled hypocentre-velocity problem and ray tracing. Subsequently, the *SIMULPS* inversion algorithm and its application in this study is described.
Chapter 4 is published entirely as 'AI based 1-D *P*- and *S*-wave velocity models for the Greater Alpine region from local earthquake data, *Geophysical Journal International*' (Braszus et al., 2024). It contains a detailed evaluation of several neural network based picking algorithms and presents the first comprehensive crustal 1D *P*- and *S*-wave velocity model of the GAR including station correction terms. This serves as an initial model for the subsequent inversion of the 3D crustal *P*- and *S*-wave velocity structure of the GAR based on LET. This is presented in chapter 5 which is currently in preparation for submission to *Earth and Planetary Science Letters*.
Finally, chapter 6 concludes the thesis by summarizing the presented work while highlighting the new insights it provides.

2. Seismotectonical setting of the Greater Alpine region

2.1. Evolution of the Alpine orogen

Since at least the Late Cretaceous the European and African plates have been converging with the Adriatic microplate wedged in-between (Stampfli and Borel, 2002; Handy et al., 2010). This initiated oceanic subduction of the Alpine Tethys along the Europe-Adria plate boundary around 84 Ma (Handy et al., 2010). Subduction continued until 35 Ma when the closing of the Alpine Tethys transformed the plate interface into a NW–SE oriented continental collision zone along which the Alpine mountain chain began to form (Handy et al., 2010; Carminati et al., 2012). This was followed by counterclockwise rotation of the Adriatic plate and thus a change in convergence direction from NW–SE to WNW–ESE and a decrease in convergence velocity in the Central and Eastern Alps relative to the Western Alps (Dewey et al., 1989). As a result, increased crustal shortening in the Western and Western Central Alps has lead to the development of a thicker crustal root than in the Eastern Alps (Spada et al., 2012). A simplified geological map including the main tectonic units and fault lines is shown in Figure 2.1. During collision, the Adriatic plate largely overthrusted the southward subducting European plate which resulted in the Austroalpine nappes of Adriatic orogen in the Eastern Alps (light brown). Here, a small part of European accreted units has been exhumed along the Tauern window. The northern and southern forelands are characterized by the sedimentary Molasse and Po basin, respectively. In the Southeastern Alps a rigid part of the northern Adriatic plate indented into the European plate causing the W-E striking Periadriatic fault to be offset sinistrally by the Giudicarie line. This was accompanied by eastwards extrusion of the Eastern alpine crust towards to Pannonian basin (Ratschbacher et al., 1991; Horvath et al., 2006). The seismic signature of this Adriatic indenter has been investigated by various seismological studies in the past (Bianchi and Bokelmann, 2014; Jozi Najafabadi et al., 2022; Kästle et al., 2024) and will be reassessed in this work. Another notable and well-known geological feature is the Ivrea body at the western end of the Po basin which is seen clearly in seismic (Diehl et al., 2009a; Zhao et al., 2016a; Solarino et al., 2018) and gravity studies (Bayer et al., 1989) and thus can be used as a benchmark-feature for this work.

2.2. Seismic activity of the area

This section is mainly based on the findings of the most recent comprehensive assessment of seismicity in the GAR from Bagagli et al. (2022).

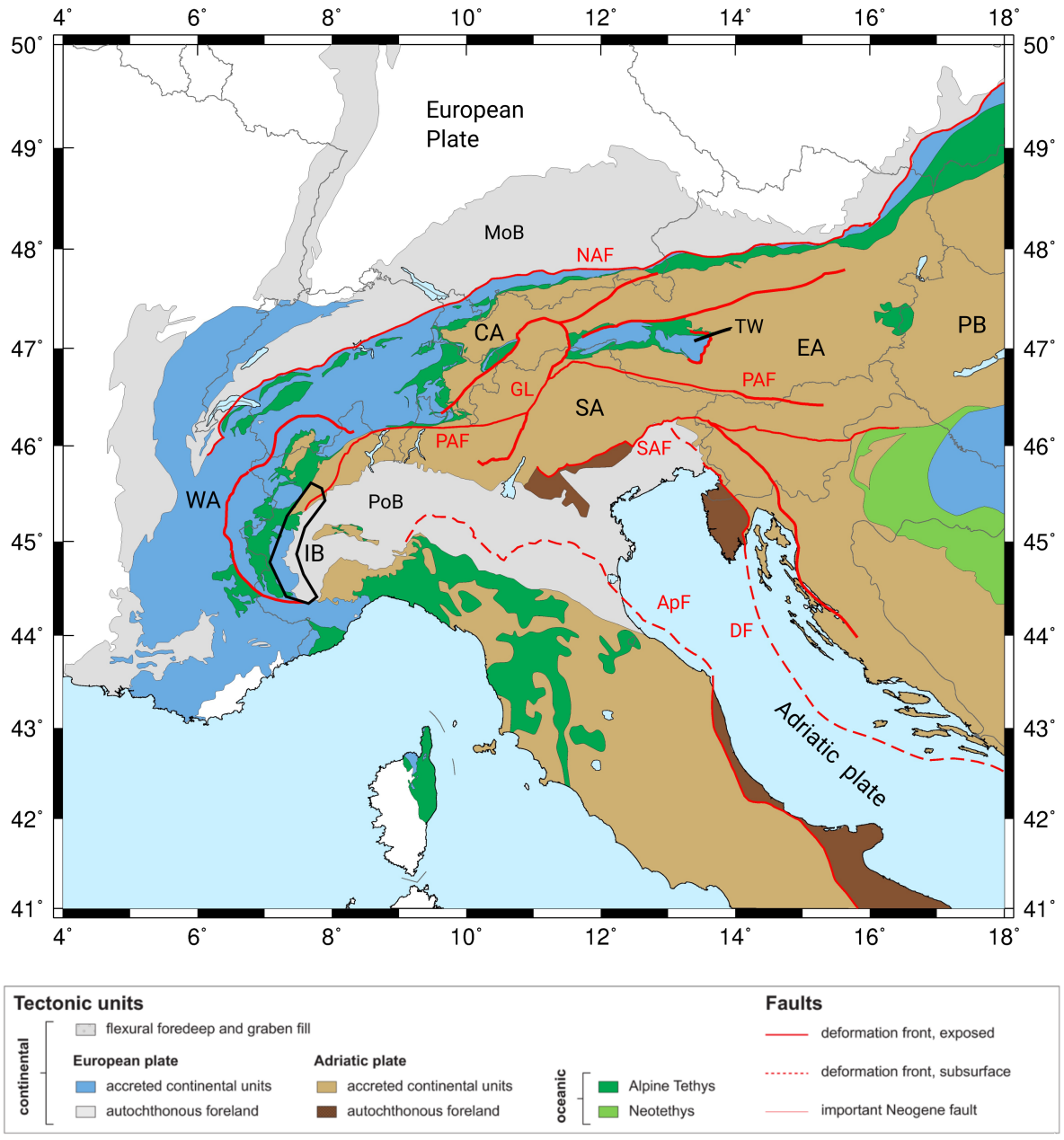

Figure 2.1.: Tectonic map for the Greater Alpine region based on units and major lineaments simplified from Schmid et al. (2004, 2008); Handy et al. (2010, 2014, 2019); Bigi et al. (1990); Froitzheim et al. (1996); Bousquet et al. (2012). NAF - Northern Alpine Front, PAF - Periadriatic Fault, GF - Giudicarie Line, DF - Dinaric Front, ApF - Apenninic Front, TW - Tauern Window, PoB - Po Basin, MoB - Molasse Basin, PB - Pannonian Basin, WA - Western Alps, CA - Central Alps, SA - Southern Alps, EA - Eastern Alps, IB - Ivrea body.

The Alpine arc ranges over various countries and earthquake monitoring generally is a national task. Therefore, there are a number of event catalogs within the GAR based on different processing workflows and often overlapping in the border regions. This chapter summarizes the analysis of recent seismicity in the GAR based on the densified station network of the AASN. The AlpArray Research Seismicity-Catalogue (AARSC) from Bagagli et al. (2022) merges event catalogs from national agencies and additionally detects new events reaching a magnitude of completeness of $M_c = 2.4$. Their seismicity distribution from 2016-2019 is displayed in Figure 2.2 and shows areas of increased seismicity rate that are in general agreement with previous studies. The Western Alps show two seismic arcs which are closing in on each other towards the South which matches previously analyzed seismicity (Eva and Solarino, 1998). Compared to the rest of the study area they show a high rate of rather well distributed seismicity. Moving towards the Western Central Alps the seismicity rate decreases until it begins to cluster at 10.5°E. Eastwards from here events are clearly aligned along two W-E oriented bands of seismicity. The first is following the Southern Alpine front at the transition from Southern Alps to the Po basin in Northern Italy. This fault marks the currently active plate boundary along which most of the convergence between European and Adriatic plate is accommodated resulting in the observed high seismicity (Handy et al., 2014). Similarly, there is a band of seismicity slightly South of the Northern Alpine front along the northern outline of the orogen. The area of the Eastern Alps in-between these two major faults is characterized by sparse seismicity as recently confirmed by Hofman et al. (2023). In agreement with Bagagli et al. (2022) they find an area of high seismicity in the Friaul and Slovenia region along the Dinaric fault system and the Montello–Friuli thrust belt. South of the Alps there is the relatively aseismic Po plain followed by the highly seismogenic Northern Apennines on the southern edge of the research area. Seismicity north of the Alpine arc is highest along the upper Rhine graben and the Hohenzollern graben with otherwise low seismicity rates in Southern Germany, Northeastern Austria and the Southern Czech Republic.

With only few exceptions the seismicity across the entire GAR is confined to the upper 25 km (Fig. 2.2). Firstly, due to this lack of seismic events in the mantle, it is not possible to trace subducted plates along the Wadati-Benioff zone. This leaves room for ambiguous interpretations of teleseimic tomographies regarding subduction history and current slab configurations in the upper mantle (e.g. Zhao et al., 2016a; Paffrath et al., 2021; Plomerová et al., 2022). Secondly, the given geometry with mostly shallow seismicity is similar to an active refraction seismic experiment with predominantly sub-horizontal head waves at Moho depths and close to vertical refracted ray paths in the lower crust. In this regard, this study is different from LETs in subduction zone regimes, where a more continuous seismicity throughout the crust and upper mantle provides a more uniform illumination of the model space. Fortunately, the large amount of available arrivals and the ability to include onsets from the crustal triplication zone using the *2-fit method* (chapters 3.2 & 4.4.4) ensure a good resolution with only marginal vertical smearing in the main areas of interest as the reconstruction test in section 5.4 are showing.

Since I do not detect seismic events myself, I use hypocentral parameters from the AARSC as initial

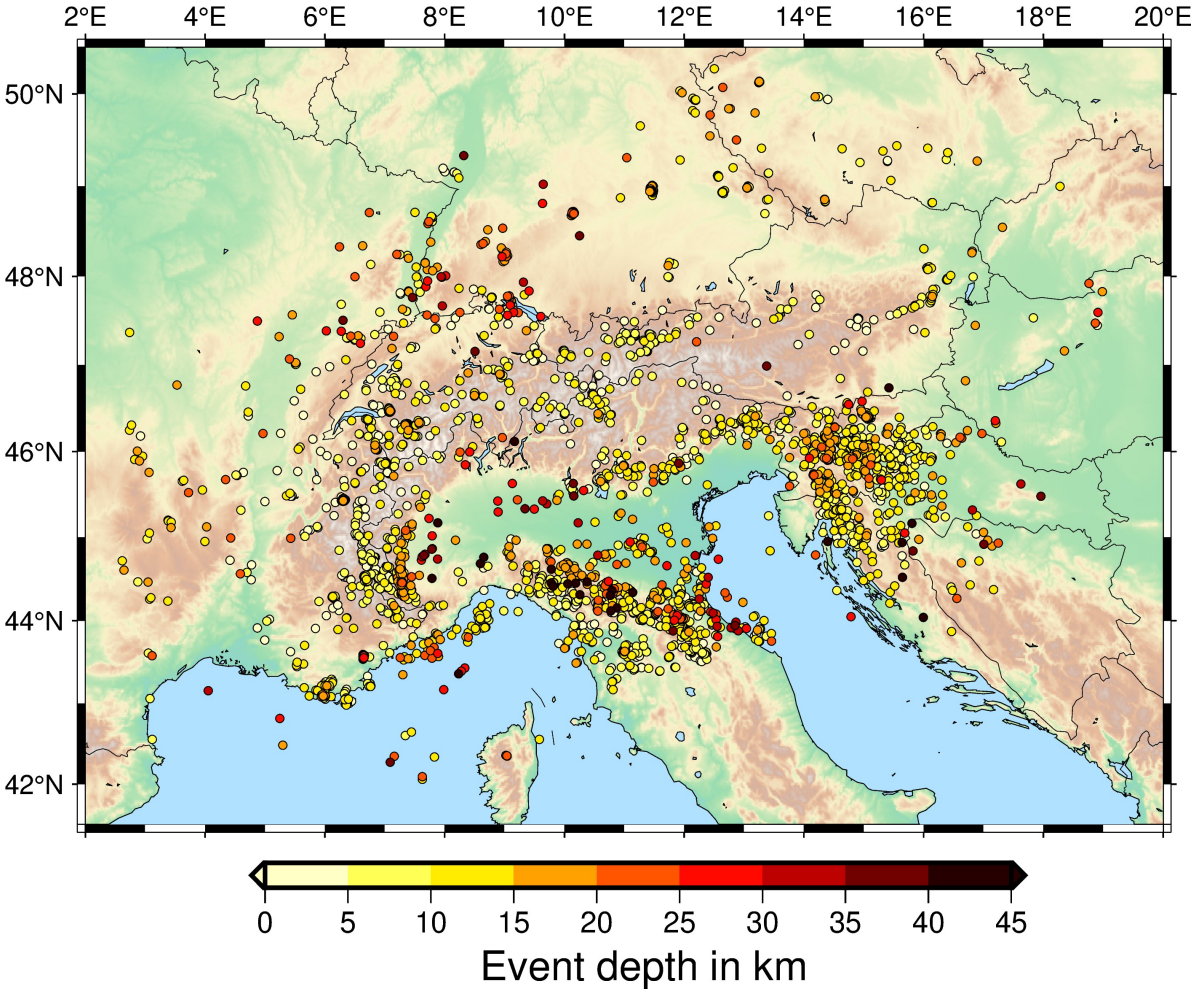

Figure 2.2.: Seismicity distribution of the AlpArray Research Seismicity-Catalogue (Bagagli et al., 2022) consisting of 3293 events between January 2016 - December 2019.

values for the coupled hypocentre-velocity inversion. For the time period from 2020-2022 which is not covered by the AARSC, I compiled an initial event catalog based on detections of the EPOS-EMSC (*https://www.seismicportal.eu/*), RESIF (*https://franceseisme.fr/*), INGV (Arcoraci et al., 2020) and ISC (*https://www.isc.ac.uk/iscbulletin/*) agencies and removed duplicates between the catalogs. This results in 2553 seismic events shown in Figure 5.1 upon which the 3D velocity model is based.

3. Data and Methods

3.1. Seismic Phase Picking

Accurate determination of seismic phase arrival times is a crucial task for the seismological fields of hypocentre localization and LET. Thus, over the past decades a variety of methods have been explored to extract phase onset times and associated uncertainties from continuous waveform recordings. Over the last few years, machine learning has lead to fundamental changes in the way the seismological community analyses waveform data. This paragraph gives an overview of the most commonly used conventional picking algorithms and summarizes the advances of recent years based on machine learning techniques.
Traditionally, many picking algorithms were developed based on the fundamental work of Allen (1978) who introduced characteristic functions (CF) based on the ratio of short-term-average to long-term-average (STA/LTA) of the waveform signal. These CFs are calculated by non-linear transformations of the time series and are predominantly sensitive to changes in the signal amplitude. Baer and Kradolfer (1987) improved the CF by implementing sensitivity to signal frequency and phase.
Based on this, the *MannekenPix (MPX)* algorithm was developed which includes an automatic quality weighting (Aldersons, 2004; Di Stefano et al., 2006; Diehl et al., 2009b). While it does achieve the quality and consistency of manual picks, it does require a significant amount of parameter fine-tuning to reach its optimal performance. Diehl et al. (2009a) applied the *MPX* picker in their regional scale LET of the Western and Central Alps and compiled a high accuracy manual *P*-phase arrival time catalog including pick uncertainties based on which the *MPX* parameters were tuned.
In recent years, machine learning (ML) techniques have fundamentally pushed the boundaries regarding accuracy and efficiency of automatic picking algorithms. A number of neural-network based pickers have been published (Weiqiang and Beroza, 2018; Ross et al., 2018; Woollam et al., 2019; Mousavi et al., 2020; Soto and Schurr, 2021) reaching the approximate accuracy and consistency of manual analysts. Münchmeyer et al. (2022) performed a benchmark testing on these most commonly used ML pickers assessing their performance on event detection, onset time determination and phase identification based on the *SeisBench* toolbox (Woollam et al., 2022). They find *PhaseNet* (Weiqiang and Beroza, 2018) to perform best, closely followed by *EQTransformer* (Mousavi et al., 2020) and *GPD (Generalized Phase Detector)* (Ross et al., 2018). Based on this, I compare the outputs of *PhaseNet*, *EQTransformer* and *GPD* to the high quality manual *P*-phase pick catalog of the GAR from Diehl et al. (2009a) (see section 4.4.1). After evaluating pick accuracy, recall rate and number of additional picks I find *PhaseNet* to perform best and thus use it for all further phase picking in this study.

3.2. Crustal triplication zone & 2-fit-method

Local Earthquake Tomography (LET) is based on ray theory which is a high frequency approximation of the elastic wave equation. The energy transported by a wave field is described by ray paths which are orthogonal to the respective wave front (Lay and Wallace, 1995). The crust-mantle boundary is commonly referred to as Moho and is mainly located at depths of 25 - 50 km beneath the Alps (Spada et al., 2012). According to Snell's law, the vertical velocity contrast along the Moho causes the downgoing ray from a crustal earthquake to split into a refracted (*Pn* phase) and reflected (*PmP* phase) ray. At the angle of critical refraction the *Pn* phase travels along the Moho interface while constantly emitting parts of its energy towards the surface (Lay and Wallace, 1995). Since these *Pn* phases are travelling with an increased velocity along the Moho they are overtaking the direct Pg phases at a certain distance defined as cross-over distance. Therefore, beyond the cross-over distance *Pn* phases are the first arriving phases. *PmP* phases never are first arrivals since their ray path is always longer than the one of the *Pg* phase. Diehl et al. (2009b) (their Fig. 3) illustrate this including observed and synthetic onsets for an exemplary event in Northeastern Switzerland at 13 km depth. Based on a 1D model with a Moho depth of 35 km, they define the epicentral distance range from 110 - 180 km as triplication zone since the crustal *Pg*, *PmP* and *Pn* phases are arriving shortly after each other. Their cross-over distance lies between 140 - 150 km. This value can vary strongly, though, depending on event depth and Moho topography.

Although, for LET it is not necessary to assign the correct seismic phase to each individual arrival, it is crucial to determine whether a picked onset is a first or secondary arrival. This is especially complicated in the distance range just beyond the cross-over distance where the rather small amplitude of the *Pn* can be hard to detect in the background noise prior to the usually more pronounced *Pg* arrival. If secondary arrivals were consistently mislabelled as first onsets, this could lead to an erroneous increase of observed travel times causing systematic errors in the subsequent velocity inversion. An option to avoid this issue would be to categorically exclude arrivals from the triplication zone (Wagner et al., 2013; Escudero, 2022). However, this would mean dismissing a substantial part of the determined arrival times resulting in a less homogeneous illumination of the model space.

In the following, I will elaborate on how I was able to robustly select first arrivals throughout the cross-over distance by developing the data-driven pre-inversion *2-fit-method* pick selection workflow. The dense station spacing of the AASN and *PhaseNet's* ability to consistently pick crustal phases of up to more than 700 km for many events with $M_L \geq 2.5$ yields an extraordinary number of *P*- and *S*- phases per event (Fig. 4.4). The *2-fit-method* uses this large number of data points to identify outliers in the automatic *PhaseNet* picks based on the (in)consistency with observations from the same event using two weighted linear regressions. A step by step illustration of this process is given in Figure 3.1. All panels show the reduced travel time of *PhaseNet's P*-phase picks plotted over their hypocentral distance for an exemplary $M_L = 3.8$ event in Northeastern Italy at 2.0 km depth. Blue crosses mark the synthetic onset based on the slightly modified 1D velocity model from Diehl et al. (2009a). A corridor of ± 7 s around

this synthetic onset is denoted by green crosses and defines the picks which are considered for further processing. All arrivals outside this corridor are discarded due to their unreasonably large deviation from the predicted arrival time. Figure 3.1a is showing the initial picks before the selection process. In a first step, a weighted linear regression is fit through arrivals up to 100 km and picks deviating by more than 2σ are discarded. Another weighted regression is fit through the remaining picks up to 100 km. The inverse of the slope of this fit corresponds to the average velocity of *Pg* phases for this event. The process at this stage is shown in Figure 3.1b. Starting at 150 km a corridor (blue shaded area) of $\pm 4\sigma$ around the extrapolation of this fit marks the range of the expected overcritical *Pg* phase onset. Arrivals within this corridor are not considered for the next step in which a second weighted linear regression is fit through onsets from 250 - 700 km (Fig. 3.1c). Similarly to the first fit, picks deviating by more than 2σ are discarded and another weighted regression is fit through the remaining onsets. Lastly, both regression lines are extrapolated until they intersect and picks at distances from 100 - 250 km are selected or discarded depending on whether they lie within 2σ of the corresponding fit. On traces with multiple arrivals within this 2σ range, only the first pick is selected. Onsets later than the blue corridor are labelled as *PmP* since this phase is expected to arrive in this part of the diagram and therefore discarded. This final stage of the pick selection is shown in Figure 3.1d. All final plots are manually inspected and events with unreasonably sloped regression lines due to many pick outliers are discarded entirely. The workflow is applied to the *S* arrivals in the same way as illustrated in Figure A.5. For further processing only events with $\geq$8 *Pg* phases and $\geq$4 *Sg* phases are considered. For the poorly resolved are in the Po plain (Fig. 5.5) this criteria is loosened to only $\geq$8 *Pg* phases. For events with less than 5 *Pn/Sn* arrivals between 250 - 750 km no *Pn/Sn* fit is calculated and only *Pg/Sg* arrivals are selected.

The *2-fit-method* as described above refers to its final version (section 5.3.4) as applied to selected picks used for the 3D velocity inversion. An earlier version of the *2-fit-method* (section 4.4.4) which plotted the epicentral distance on the x-axis and excluded the corridor of the potential overcritical *Pg* arrivals has been used to select picks for the minimum 1D velocity model. Due to the smaller number of free parameters in the 1D model, it is still possible to obtain an overdetermined inverse problem with more strict selection criteria. Therefore, the focus lied on minimizing the number of falsely selected secondary arrivals and it could be afforded to discard the potentially overcritical *Pg* arrivals entirely.

The 3D inverse problem is mixed-determined, though, consisting of overdetermined and underdetermined parts of the model space. Thus, a higher number of picks improves model resolution significantly which counterbalances the low number of falsely selected secondary arrivals from within this range.

In summary, I developed a data-driven pre-inversion pick selection algorithm which automatically removes outliers from the initial arrival time catalog based on their (in)consistency with other data from the same seismic event. With a minimum of manual supervision it is able to select *P*- and *S*-phase first arrivals of up to 1000 km distance including the crustal triplication zone. Since its performance significantly improves with an increasing number of arrivals it requires a densely spaced seismic network over

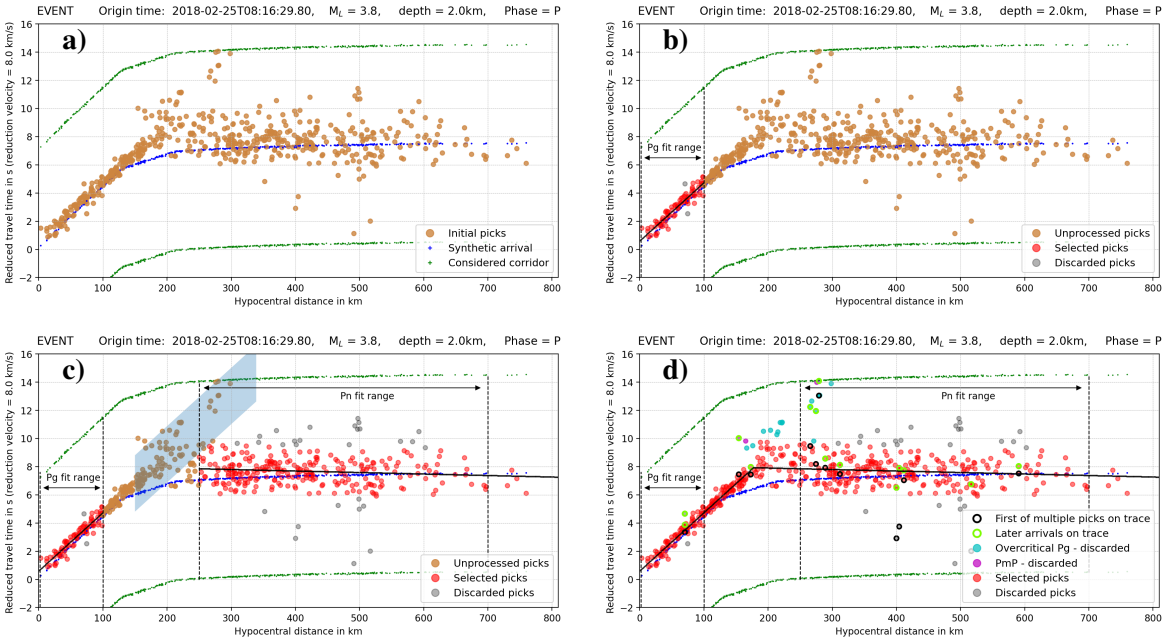

Figure 3.1.: Step-by-step explanation of the developed *2-fit-method*. This data-driven pre-inversion pick selection technique fits two weighted linear regression lines through the *Pg* and *Pn* arrivals plotted over hypocentral distances. Thus, first arrivals are selected based on the consistency with other onsets throughout the crustal distance range. For a detailed description of the applied workflow I refer to the main text.

a rather large area.

3.3. Inverse theory

3.3.1. Coupled hypocentre-velocity problem

The following section is mainly based on the description of inverse theory from Lay and Wallace (1995). The coupled hypocentre-velocity problem in Local Earthquake tomography refers to the simultaneous determination of hypocentral parameters and the velocity structure of the surrounding material through which the rays travel before they are recorded at the seismic stations. On the one side, calculation of the velocity requires knowledge of the ray path which depends on the hypocentre. On the other side, determination of the hypocentre is based on the velocity structure. Thus, this poses a non-linear problem in which the travel time t of each ray from source i to receiver j can be expressed as the integrated inverse of the velocity v along the ray segments ds with

$$t_{ij} = \int_{source}^{station} \frac{1}{v} \, \mathrm{ds} \tag{3.1}$$

The absolute arrival time of each seismic onset is given by

$$T_{ij}^{obs} = t_0 + t_{ij}(x_i, y_i, z_i, v(s), x_j, y_j, z_j) \tag{3.2}$$

with the origin time t_0, the travel time t_{ij} from source (x_i, y_i, z_i) to receiver (x_j, y_j, z_j) and the velocity distribution $v(s)$ along the ray path.
In order to solve this non-linear problem, a reference model with estimated values of the velocity structure and hypocentral parameters based on *a priori* information is created. Differences between the observed arrival times T_{ij}^{obs} and the reference model arrival times T_{ij}^{ref} are defined as travel time residuals

$$r_{ij} = T_{ij}^{obs} - T_{ij}^{ref} \tag{3.3}$$

During the inversion the reference velocity model and hypocentral parameters are updated iteratively in a way that the residuals r_{ij} are minimized. Since the residuals r_{ij} are depending on the model and hypocentral parameters in a non-linear way the problem can be linearized using a first order Taylor series expansion

$$r_{ij} = \Delta T_0 + \sum_{k=1}^{3} \left[\frac{\partial t_{ij}}{\partial x_{kj}} \Delta x_{kj} \right] + \sum_{l=1}^{L} \left[\frac{\partial t_{ij}}{\partial v_l} \Delta v_l \right] \tag{3.4}$$

where ΔT_0 and Δx_{kj} are describing the update of origin time and hypocentre location, respectively. Similarly, the update of the velocity parameters is given as Δv_l. Equation 3.4 is used to express the influence of hypocentral and model parameters on the residual of each arrival. This system of equations also can be written in matrix notation as

$$\vec{d} = \mathbf{G}\Delta\vec{m} \tag{3.5}$$

where travel time residuals r_{ij} are summarized in the data vector $\vec{d}$, model and hypocentral parameter updates are represented by the model vector $\Delta\vec{m}$ and their relation is defined by the Jacobi matrix $\mathbf{G}$. For cases where the number of independent observations in $\vec{d}$ equals the length of $\Delta\vec{m}$ a single unique solution can be found for the inverse problem. Due to the inevitable inconsistencies in real data and the overdetermination of seismological inverse problems there is always a part of the observed data which can not be explained by the model. Therefore, the misfit term $\vec{\varepsilon}$ is introduced to equation 3.5

$$\vec{d} = \mathbf{G}\Delta\vec{m} + \vec{\varepsilon} \tag{3.6}$$

which leads to

$$\vec{\varepsilon} = \vec{d} - \mathbf{G}\Delta\vec{m} \tag{3.7}$$

The goal of the inverse problem is to find the set of model parameters $\vec{m}$ which explains the observed data $\vec{d}$ as good as possible and thus minimizes the misfit $\vec{\varepsilon}$. A common way to do this is to express the squared misfit as

$$\vec{\varepsilon}^2 = \sum_{i=1}^{n} \left[d_i - \sum_{j=1}^{m} G_{ij} m_j \right]^2 \tag{3.8}$$

and find its minimum by setting its derivative with respect to the model parameters v_l to zero

$$\frac{\partial \vec{\varepsilon}^2}{\partial v_l} = \frac{\partial}{\partial v_l} (\vec{d} - \mathbf{G}\Delta\vec{m})^2 = 0 \tag{3.9}$$

This can be written as

$$\Delta\vec{m} = (\mathbf{G}^T\mathbf{G})^{-1}\mathbf{G}^T\vec{d} \tag{3.10}$$

The irregular distribution of seismic sources and receivers causes the ray paths to sample the model space heterogeneously. Due to this redundancy in the data, the generally overdetermined problem with more observables than model parameters also contains model parameters that can not be determined independently. This combination of over- and under-determination of the model space is referred to as mixed-determined (Menke, 1989). Adding a damping value λ^2 to the diagonal elements of $\mathbf{G}^T\mathbf{G}$ ensures a more stable inversion result and avoids strong updates of poorly resolved model parameters. This yields the equation for the damped least squares solution of the inverse problem

$$\Delta\vec{m} = (\mathbf{G}^T\mathbf{G} + \lambda^2\mathbf{I})^{-1}\mathbf{G}^T\vec{d} \tag{3.11}$$

as incorporated in the *SIMULPS* algorithm (Thurber, 1983). In order to keep the system matrix $\mathbf{G}$ at a manageable size, *SIMULPS* applies parameter separation as introduced by Pavlis and Booker (1980) and Spencer and Gubbins (1980). This study uses the most recent version *SIMUL2023* (Eberhart-Phillips et al., 2024).

3.3.2. Ray tracing

Ray tracing is a key part to the solution of the seismic forward problem in which the travel time of a seismic ray along its initially unknown path for a given source-receiver pair is determined. Similar to equation 3.1, the travel time t along a ray path $\vec{r}$ can be expressed as the integrated inverse of the velocity v along the ray segments ds with

$$t = \int_s \frac{1}{v(\vec{r})} ds \tag{3.12}$$

This poses a non-linear problem, since the ray path itself is depended on the velocity structure of the medium.
From equation 3.12 the ray path equation

$$\frac{d}{ds}\left(\frac{1}{v(\vec{r})}\frac{d\vec{r}}{ds}\right) = \nabla\left(\frac{1}{v(\vec{r})}\right) \tag{3.13}$$

can be derived (Lay and Wallace, 1995). In seismology, this second-order differential equation can be solved in two different ways (Julian and Gubbins, 1977). It can be transformed into a initial value problem (shooting method) by assuming a take-off angle of the ray from the source location. This take-off angle then is varied until the ray hits the receiver location within a given error margin.
Alternatively, the ray path equation can be solved with a two point boundary value problem by assuming an approximated initial ray path and iteratively solving the differential equation (bending method).
In this study I use the *SIMUL2023* inversion algorithm which implemented an approximation of the bending method based on Um and Thurber (1987). This method starts with a circular arc segment as initial ray path which connecting source and receiver. It is discretized by a finite number of points along the path which are connected by a straight line. Considering three adjacent points on the path, the central point is shifted in a way that the travel time along the two ray segments defined by the three points is minimized. This is done iteratively until the decrease in synthetic travel time becomes negligible.

3.3.3. SIMULPS inversion algorithm for LET

The *SIMUL* inversion algorithm was developed by Thurber (1983) who used it to derive the crustal 3D *P*-wave velocity structure of the Coyote Lake Area in Central California. Over the last four decades, it has been improved consistently and applied in numerous LET studies (e.g. Haberland et al., 2009; Hicks et al., 2014; León-Ríos et al., 2021) making it a well established tool in crustal seismic tomography. Subsequently, Eberhart-Phillips (1990) included the possibility to invert for *vs* based on *S*-wave arrival times and Rietbrock (2001) incorporated the *Q* inversion based on t^* observations. Due to their higher signal-to-noise ratio *P*-phase arrivals generally outnumber the *S*-phases leading to a significantly poorer resolution in the resulting *vs* and *vp/vs* models. Thus, it is advisable to solve for *vp* and *vp/vs* inverting *S-P* travel times (Eberhart-Phillips and Reyners, 1997) in order to obtain a robust *vp/vs* result with values close to the initial model in areas of sparse *S*-wave coverage.
In this work, I am using the most recent *SIMUL2023* version (Eberhart-Phillips et al., 2024). *SIMUL2023* requires initial values for each velocity and hypocentral parameter. These define the reference model around which the damped least squares problem of equation 3.11 is linearized iteratively. In each iteration step the reference model is updated by adding the model update $\Delta\vec{m}$ which minimizes the remaining travel time residuals $\vec{d}$. This is repeated until one of the following four criteria is reached (Evans et al., 1994):

1. the F-test yields a negative result

2. the solution norm falls below a pre-defined value *snrmct*

3. the number of iterations has reached a pre-defined value *nitmax*

4. the weighted data RMS falls below a pre-defined value *rmstop*

Diehl et al. (2021) showed that arrivals observed at large distances potentially decrease the accuracy of the obtained hypocentral parameters. Therefore, I am relocating the seismicity in a first *SIMUL* run including *P*-arrivals from $\Delta \leq 130$ km and *S*-arrivals from $\Delta \leq 80$ km. Initial event location are taken from Bagagli et al. (2022) where possible and otherwise from the EMSC, INGV, RESIF and ISC agencies. Starting v_p values at each nodal plane are based on the *GAR1D_McMC* model from Braszus et al. (2024) with a constant v_p/v_s ratio of 1.71 representing the average value of their v_p/v_s model. Based on the limited epicentral distance of the considered arrivals the strongest updates to the initial velocity model are made in the upper and middle crust. Below a depth of 25 km the output model is very close to the initial 1D structure. This velocity model is taken as input for a second inversion run including picks from all distances. Hypocentre locations are fixed while the origin time is inverted freely. No station corrections are used in either of the two inversions.

The damping value λ has no consistent unit, since it depends on the type of model parameter (v_p, v_p/v_s, event hypocentre or origin time) to which it is applied. In the following, all damping parameters refer to the numerical value of λ as it is given in the *CNTL* file of *SIMUL*. Its value is determined based on trade-off curves in a way that it minimizes the remaining data variance as well as the model update variance. These trade off curves are computed separately for v_p and v_p/v_s for both inversion runs as shown in Figure B.4. An overview of other important parameters in the *CNTL* file for both runs is given in Table 3.1.

The velocity model is parametrized in a cartesian coordinate system on nodes defined by the model spacing arrays in x-, y- & z-direction. The number of nodes and their ideal horizontal and vertical spacing is unique to each inversion geometry and mainly depends on the number of observations and their spatial distribution. I used checkerboard reconstruction tests to determine the finest model spacing with which the synthetic model can still be recovered with sufficient quality. Based on these tests I use a horizontal spacing of 25 km in the area of interest for all inversions. In areas of sparse ray coverage towards the edges of the model and beneath the Ligurian and Adriatic sea neighbouring nodes are linked and treated as a single model parameter in the inversion (Thurber and Eberhart-Phillips, 1999). This prevents strong model updates in poorly constrained areas with low ray coverage. Linking is performed only within the horizontal nodal planes.

The spread value quantifies the resolution of each model parameter by assessing the distribution of values along each row of the model resolution matrix (MRM). Model parameters with high diagonal elements in the MRM thus have a small spread value. Figure B.3 shows the node distribution including linked and fixed nodes at $z = 18$ km depth.

Table 3.1.: Selection of most important parameters in the *SIMUL2023 CNTL* file. Run1 refers to the first inversion run in which the events are relocated using *P*-arrivals from $\Delta \leq 130$ km and *S*-arrivals from $\Delta \leq 80$ km. Here, the residual weighting (res1, res2, res3) is not explicitly defined in the *CNTL* file, but picks with a remaining residual of $\geq \pm 1.0$s are discarded and thus not considered for Run2. In Run2 observations from all distances are included, event locations are kept fix and only the origin time is updated.

parameter in *CNTL* file	Run1	Run2
vpdamp	1000	5000
vsdamp	1000	4000
nitmax	10	13
ifix1	4	13
res1		1.5
res2		2.0
res3		2.5

While the location of stations and events is given in latitude and longitude of a geographical coordinate system, the model parametrization and ray tracing requires a cartesian coordinate system. Since the *SIMUL2017* version (Eberhart-Phillips et al., 2021), the Transverse Mercator projection is used as a transform operation between the two coordinate systems replacing the previously implemented short distance conversion.

3.3.4. Towards a Monte-Carlo 3D inversion

The previously described workflow including trade-off curves for damping value selection, fixing and linking of nodes and the determination of horizontal grid spacing based on the quality of reconstruction tests is well established in LET applications (e.g. Eberhart-Phillips, 1986; Diehl et al., 2009a). Furthermore, hypocentre shift tests are a common tool to assess the stability of the inversion result and the dependency of the final hypocentral and velocity parameters on the initial event locations (Haslinger et al., 1999; Husen et al., 1999).

This work strongly expands this approach by perturbing not only starting event locations but also the initial 1D velocity structure and the vertical and horizontal parametrization of the model space within reasonable bounds. Thus, the inversion problem is linearized around a large number of varying starting models. This increases the likelihood to overcome local minima close to the initial model and furthermore allows a statistical assessment of model parameter uncertainties.

Based on the accuracy estimate of the initial hypocentres located in a 1D model including station corrections (section 4.6.3) the event locations are shifted prior to each individual by $\sigma_{hor} = 2.0$ km and $\sigma_{ver} = 6.0$ km in horizontal and vertical direction, respectively. Additionally, the initial 1D v_p structure is varied within the uncertainty of the *GAR1D_McMC* model (section 4.5.1). The parametrization of the model space has a strong influence on the resulting model and thus has to be chosen carefully. I evaluated

the quality of checkerboard reconstruction tests for a range of reasonable grid spacings. Generally, coarse grids are showing well reconstructed synthetic inputs but also have a higher remaining data misfit due to fewer model parameters. Finer grids with more free parameters are reducing the misfit significantly but are more likely to show smearing effects or unreasonable small scale oscillations due to overfitting. The best compromise for this trade-off is unique to each inversion problem and mainly depends on ray density within the model space and thus on the number of observations and the distribution of sources and receivers.

Section 5.3.5 describes the workflow based on which I chose a final parametrization of 7 nodal planes between 0 - 70 km and a horizontal node spacing of 25 km. I run 750 inversions each with a random horizontal shift of the entire grid by $\pm$12.5 km, almost arbitrary vertical node spacing and perturbation of initial hypocentres and velocity structure as described above.

This can be seen as a first step towards a probabilistic 3D inversion using the *SIMULPS* code which would probe an even wider set of initial model parameters. Furthermore, transdimensionality could be introduced to automatically optimize the number of model parameters in a data-driven way based on estimated pick accuracy and remaining data misfit. One option to implement this would be a *Markov chain Monte Carlo (McMC)* approach similar to the 1D inversion algorithm developed by Ryberg and Haberland (2019). I used this method to calculate the minimum 1D *P*- and *S*-wave velocity structure of the GAR including station corrections while simultaneously relocating seismicity (section 4.5.1). The efficiency of the implemented forward calculation based on the 2D finite difference eikonal solver of Podvin and Lecomte (1991) allows to assess the misfit of a few million models within days. Such an extensive testing of initial models and grid spacings is not possible for the computationally much more expensive 3D inversion. Nevertheless, the calculation of a few tens of thousands of models is feasible already with current high performance computational infrastructure and most likely will be further facilitated in the future.

4. Minimum 1D velocity model

The following chapter describes the data processing steps and inversion details towards the first comprehensive minimum 1D *P*- & *S*-wave velocity model of the Alpine mountain chain. For future studies, this will provide consistent synthetic travel times and facilitate the (re)location of seismicity including *P*- and *S*-phases throughout the Greater Alpine region. Furthermore, it serves as an initial model for the subsequent computation of a high resolution 3D velocity model (see chapter 5).
A special focus is laid on the performance assessment of the most commonly used neural network based seismic phase picking algorithms. I developed a new data-driven method to systematically discard outliers in the AI based arrival time catalog applicable to *P*- and *S*-phase onsets up to at least 900 km epicentral distance. Based on the final pick catalog, I simultaneously relocate seismic events and invert for the 1D velocity structure including station correction terms with the established *VELEST* and the recently developed *Markov chain Monte Carlo (McMC)* algorithm.

This chapter is entirely published as:

> **Braszus, B**., Rietbrock, A., Haberland, C., and Ryberg, T. (2024). AI based 1-D P- and S-wave velocity models for the greater alpine region from local earthquake data. *Geophysical Journal International*, 237(2):916–930. DOI: https://doi.org/10.1093/gji/ggae077

4.1. Abstract

The recent rapid improvement of machine learning techniques had a large impact on the way seismological data can be processed. During the last years several machine learning algorithms determining seismic onset times have been published facilitating the automatic picking of large data sets. Here we apply the deep neural network *PhaseNet* to a network of over 900 permanent and temporal broad band stations that were deployed as part of the AlpArray research initiative in the Greater Alpine Region (GAR) during 2016-2020. We selected 384 well distributed earthquakes with $M_L \geq 2.5$ for our study and developed a purely data-driven pre-inversion pick selection method to consistently remove outliers from the automatic pick catalog. This allows us to include observations throughout the crustal triplication zone resulting in 39,599 *P* and 13,188 *S* observations. Using the established *VELEST* and the recently developed *McMC* codes we invert for the 1D *P*- and *S*-wave velocity structure including station correction terms while simultaneously relocating the events. As a result we present two separate models differing in the maximum included observation distance and therefore their suggested usage. The model *AlpsLocPS*

is based on arrivals from ≤ 130 km and therefore should be used to consistently (re)-locate seismicity based on *P* & *S* observations. The model *GAR1D_PS* includes the entire observable distance range of up to 1000 km and for the first time provides consistent *P*- & *S*-phase synthetic travel times for the entire Alpine orogen. Comparing our relocated seismicity with hypocentral parameters from other studies in the area we quantify the absolute horizontal and vertical accuracy of event locations as ≈ 2.0 km and ≈ 6.0 km, respectively.

4.2. Introduction

While the underlying cause for the Alpine orogeny can be attributed to the collision of the Eurasian and African continental plates, the complex interactions and reorganizations of wedged microplates such as the Adriatic plate is yet not fully understood (Schmid et al., 2004; Handy et al., 2010).
This collision did not only form the present day surface topography of the orogen but also caused the formation of a crustal root beneath the mountain belt leading to strong variations in Moho depths ranging from 20-25 km in the Northern and Northwestern foreland to 50-55 km beneath the Central and Western Alps (Spada et al., 2012). The European *AlpArray* research initiative (AlpArray Seismic Network, 2015) aims to gain novel insights into the Alpine orogeny in space and time. The central part of this interdisciplinary and international project (involving 36 institutions from 11 countries) was to densify the existing permanent seismic networks by the temporary AlpArray Seismic Network (Hetényi et al., 2018). Additional networks with a more local focus such as the SWATH-D (Heit et al., 2021) were also deployed to study in high resolution specific aspects of the Alpine orogeny. Based on this unprecedented data set a wide range of seismological methods was applied to sharpen our understanding of plate/microplate reorganization, mantle dynamics and their relation to surface processes.
Recent studies have leveraged the AlpArray data set to (re)-assess seismicity as well as to refine the *P*- and *S*-wave 1D & 3D velocity structure in the Greater Alpine Region (GAR) . Recently, a comprehensive analysis of the seismicity in the entire GAR between 2016 and 2019 has been conducted by Bagagli et al. (2022). They used observations from distances of up to of 300 km to invert for a 1D *P*-wave velocity model and hypocentral parameters with the well-established VELEST code (Kissling et al., 1994). On a more local scale Jozi Najafabadi et al. (2021) inverted *P*- & *S*-phases with epicentral distances of up to 160 km for a 1D velocity model resolving the upper and mid crust beneath the Central Eastern Alps using an Markov chain Monte Carlo (McMC) algorithm from Ryberg and Haberland (2019). Using data from the Swiss seismic network Diehl et al. (2021) published a local 3D *P*- & *S*-wave velocity model for the broader Swiss region. Complimentary, ambient noise studies obtaining 3D crustal and upper mantle *S*-wave velocity models of the GAR have been conducted by Kästle et al. (2018) and Sadeghi-Bagherabadi et al. (2021).
In this study we invert travel time observations from the 384 events and 958 seismic stations displayed in Fig. 4.1 in order to obtain for the first time a joined 1D *P*- & *S*-wave velocity model for the GAR including station correction terms while simultaneously relocating the seismicity. A very basic task inherent to earthquake location and seismological tomographic studies is the determination of seismic phase arrival times. Considering the huge amount of waveforms available nowadays the application of automatic picking tool is indispensable. Accompanied by the recent rapid advances in research and application of artificial intelligence in general several deep neural network based seismic picking algorithms have been developed. They were found to reach the level of accuracy of human analysts (Weiqiang and Beroza, 2018; Woollam et al., 2019) and have been used for various seismological task such as monitoring of

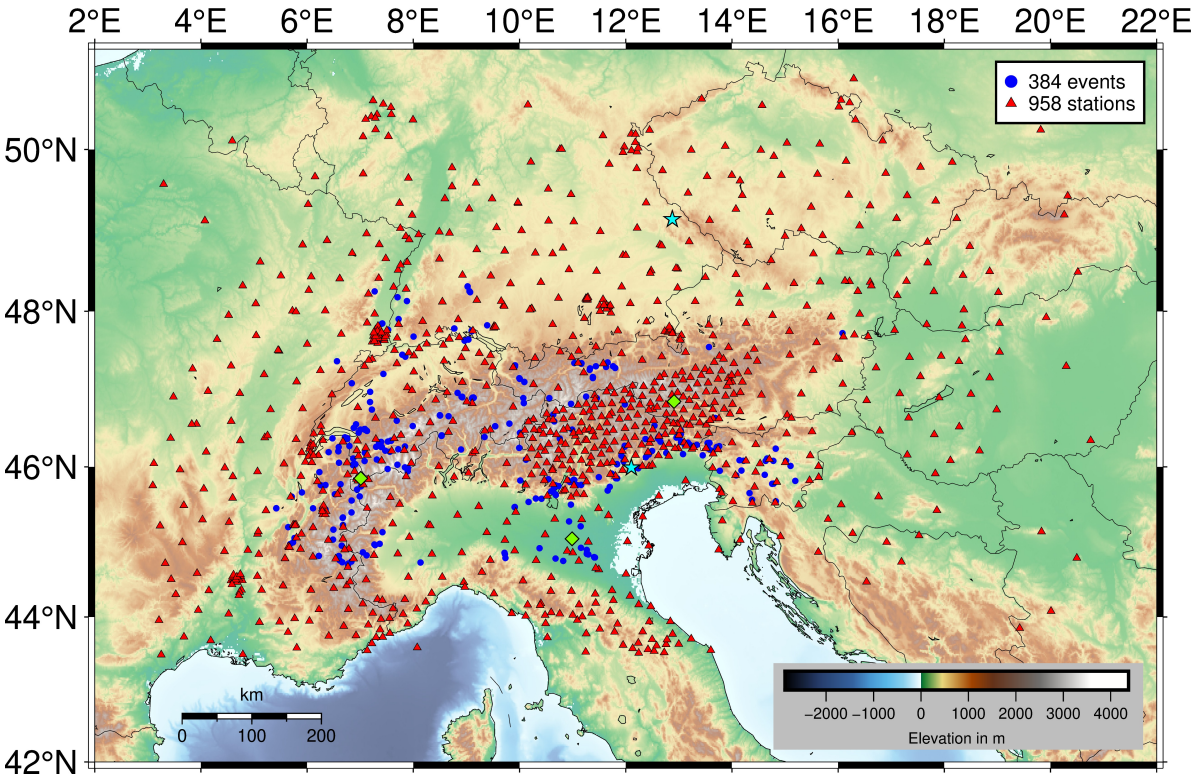

Figure 4.1.: Overview map of the Greater Alpine region showing locations of the 958 broadband seismic stations (red triangles) and 384 events (blue dots) with $M_L \geq 2.5$ used in this study. Stations *VARN* (NE Italy) and *WETR* (SE Germany) referred to in Fig. 4.9 are highlighted with cyan stars, locations at which 1D v_s profiles (Fig. 4.11) are extracted from the 3D *S*-wave models from Kästle et al. (2018) and Sadeghi-Bagherabadi et al. (2021) are marked with lightgreen diamonds.

volcanoes (Lapins et al., 2021) and real-time analysis of seismograms (Münchmeyer et al., 2021; Kuang et al., 2021). We carefully assess the performance of the most widely used neural network pickers on our data set using *Seisbench - A toolbox for machine learning in seismology* based on Woollam et al. (2022) and Münchmeyer et al. (2022).

For the inversion we apply the *McMC* and *VELEST* algorithms to our *P*- and *S*-phase data and as a result present the first orogen wide travel time based 1D *P*- and *S*-wave model of the GAR. Our *AlpsLocPS* model with resolution in the upper and mid crust is based on observations from distances of 0 - 130 km and allows consistent (re)-localization of seismicity within the GAR using *P*- and *S*-phases. The *GAR1D_PS* model incorporates arrivals from up to 1000 km and therefore resolves the entire crust and the uppermost mantle.

4.3. Data

The majority of waveforms analysed is provided by the AlpArray seismic network (Hetényi et al., 2018) which has been in operation from 2015 to 2021 as part of the European interdisciplinary AlpArray Research initiative. Due to a hexagonal packing strategy, the partially heterogeneous distribution of permanent broad band stations in the GAR could be effectively densified to a maximum station spacing of 52 km. Thus, each point within the GAR is located within a 30 km radius of a seismic broad band station. Additionally, from October 2017 until September 2019 the SWATH-D network improved the station spacing in the Eastern and Southern Alps to 15 km (Heit et al., 2021).
We used the FDSN client implemented in ObsPy (Krischer et al., 2015) to collect station metadata and seismic broad band waveform data from 958 stations in the GAR between the years of 2016 and 2020. Only data with a sampling rate of at least 100 Hz and a channel of either "HH?", "BH?" or "EH?" has been considered. We do not remove the instrument response during processing. For consistency reasons, we resample all data to *PhaseNet's* (Weiqiang and Beroza, 2018) required sampling rate of 100 Hz before feeding the waveforms to several deep learning picking algorithms. Event detections with $M_L \geq 2.5$ and corresponding initial hypocentral parameters are obtained from the European-Mediterranean Seismic Centre (EPOS-EMSC)(*https://www.seismicportal.eu/*). The used 958 stations and 384 events are shown in Fig. 4.1 as red triangles and blue circles, respectively.

4.4. Methods

4.4.1. Phase picking

Evaluation of neural network picking algorithms using *Seisbench*

The recent rapid improvement of machine learning techniques had a strong impact on seismic data analysis. We utilize this development by testing the performance of the most widely used neural network picking algorithms on our seismic waveform data. With the recently published Seismology Benchmark collection *SeisBench* (Woollam et al., 2022) we applied the deep-neural-network picking algorithms *PhaseNet* (Weiqiang and Beroza, 2018), *EarthquakeTransformer (EQT)* (Mousavi et al., 2020) and *GPD* (Ross et al., 2018) to waveforms recorded in the Swiss Alpine region for which a high quality manual reference pick catalogue from Diehl et al. (2009a) was available. This catalogue consists of 1801 *P*-phase picks recorded from 1997-2006 and was compiled for a local earthquake tomography study of the greater Swiss area (Diehl et al., 2009a).

The neural network pickers are built on different architectures and were trained on distinct training data sets yielding one final model per architecture & training data pair. Seisbench incorporates several models for each picker based on different training data such as the ETHZ (SED at ETH Zurich, 1983), SCEDC (SCEDC, 2013), NCEDC (NCEDC, 2013), INSTANCE (Michelini et al., 2021) & STEAD (Mousavi et al., 2019) data sets. In order to assess the pickers' performance we compared the picks obtained by each neural network to the high quality manually picked catalogue of phase arrival times and associated quality classes.

The performance of the picking algorithms is assessed by the mean offset μ, the standard deviation σ and recall of the neural network picks with regard to the manual catalogue. These parameters are compared in Table 4.1 for the tested combinations of network architectures and training data sets.

While μ and σ are only varying moderately between the different automatic pickers, the recall, defined as the percentage of retrieved picks from the reference data, fluctuates significantly. This parameter strongly depends on the user-defined probability threshold t_{prob}. The lower the threshold, the higher the number of picks is in general and therefore increases the recall but at the same time causes more erroneous picks.

We decided to use the neural network *PhaseNet* in its original configuration, i.e. $t_{prob} = 0.3$, trained on the *NCEDC* data set for all further analysis, since its higher recall in our opinion outweighs the slightly increased mean offset μ.

Fig. A.1 shows a comparison of 1702 matching picks from Diehl et al. (2009a) and *PhaseNet*. As the mean offset of $\mu = 0.15$ s indicates, the entire distribution is slightly shifted to negative values i.e. late *PhaseNet* picks. Furthermore, it can be observed that the number of outliers with $|\Delta_t| > 1.0$ s is significantly larger for negative values. Late *PhaseNet* picks predominantly occur in the distance range of ≈ 100 - 300 km coinciding well with the crustal cross-over distance of *Pg*, *PmP* and *Pn* phases where

Table 4.1.: Table assessing the performance based on mean μ, standard deviation σ and recall of several neural network picking algorithms trained on various benchmark data sets using *Seisbench* (Woollam et al., 2022) when compared to the manual *P*-phase pick catalogue from Diehl et al. (2009a).

Neural network	training data	μ in s	σ in s	Recall in %
PhaseNet	NCEDC (org)	-0.15	0.27	95
	ETHZ	-0.07	0.30	80
	STEAD	-0.12	0.28	64
	INSTANCE	0.02	0.37	90
EQT	INSTANCE	-0.12	0.26	80
	ETHZ	-0.05	0.27	79
	STEAD	-0.09	0.19	35
	SCEDC	-0.08	0.26	55
	original	-0.09	0.26	36
GPD	ETHZ	-0.13	0.24	91
	STEAD	-0.1	0.22	92
	SCEDC	-0.09	0.17	67

PhaseNet is not able to always pick the rather small amplitude *Pn* first arrival. In section 4.4.4 we present a purely data-driven approach to consistently remove the overcritical *Pg*/*Sg* picks while minimizing the number of discarded first arrival observations.
Seismicity in the GAR is mainly limited to the upper crust with few exceptions (Bagagli et al., 2022). This generally causes a rather pronounced appearance of the crustal *Pg*-, *PmP* & *Pn*-phases and thus creates a more complex wavefield than in e.g. a subduction zone setting.

PhaseNet vs. manual picks

As a next step we further verify the applicability of *PhaseNet* to our data set and compare its accuracy against the inevitable influence of human subjectivity when manually determining phase arrival times. Therefore, a human analyst picked *P*- and *S*-phases from 30 events with epicentres in the Central Alpine area recorded in 2018. Six of these events were picked by a second analyst to exemplarily validate the picking accuracy. Values of μ and σ are not deviating significantly between both comparisons (see Fig. A.2) supporting the conclusion that *PhaseNet*'s picks are almost as accurate and consistent as manually determined onset times. Generally, the *S*-phase discrepancies are slightly higher most likely due to the less impulsive onset within the *P*-phase coda. When comparing *PhaseNet* and manual picks over several epicentral distance ranges we observe an increase of the standard deviation with distance for picks observed between 0-300km (Fig. B.1(a)-(c)) and no further increase in deviation for picks from

distances $\geq$300km (Fig. B.1(d)).

Finally, we compare *PhaseNet* to a set of manually revised picks from Jozi Najafabadi et al. (2021) comprising 16 events from the Central Alps within the boundaries of the SWATH-D network (see Fig. A.4). *P*- and *S*-phase inconsistencies are very similar to the values from Table 4.1 and Fig. A.2.

4.4.2. Development of a weighting scheme based on *PhaseNet*'s pick probability

Most earthquake location and inversion algorithms allow the assignment of an uncertainty value or weight to each individual phase arrival in order to increase the impact of accurate picks on the inversion result. The importance of a consistent weighting of picks based on their accuracy and the influence on the resulting tomographic image has been demonstrated by Diehl et al. (2009b). Even though *PhaseNet* does not output the uncertainty of the preferred onset time, if run in default mode it outputs a probability between 0.3 - 1.0 for each pick. Thus, in order to assign a weight to each automatic pick we investigated the correlation between the *PhaseNet* probability and manually determined pick qualities based on the 1702 matching manual reference picks from Diehl et al. (2009a). Fig. 4.2 shows the deviations of manual and *PhaseNet* picks when clustering *PhaseNet* picks to the probability ranges 0.3-0.6, 0.6-0.75, 0.75-0.9 & 0.9-1.0. Picks with higher probabilities deviate significantly less from the manual reference pick indicating a correlation between probability and accuracy of the *PhaseNet* picks. Diehl et al. (2009a) assigned the classes 0, 1, 2, 3 & 4 corresponding to absolute pick uncertainties of 0.05s, 0.1s, 0.2s, 0.4s & >0.4s to each of their picks. Fig. 4.3 shows the number of picks per class for the same *PhaseNet* probability ranges as above. The most accurate manual picks predominately show up in the highest *PhaseNet* probability range, while lower class manual picks are more likely to fall into lower probability ranges. We use this correlation to estimate an average pick uncertainty ε. For each probability range the uncertainties associated to the manual pick classes 0-3 are averaged while weighted by the number of corresponding picks. Class 4 picks are not considered since they were not assigned a discrete uncertainty value. Even though the absolute values of ε seem to be an underestimation of the actual uncertainty when compared to the values of μ and σ in Fig. 4.2, the trend of increasing accuracy with increasing pick probability is systematic which suggests relative weighting of *PhaseNet* picks based on their probability.

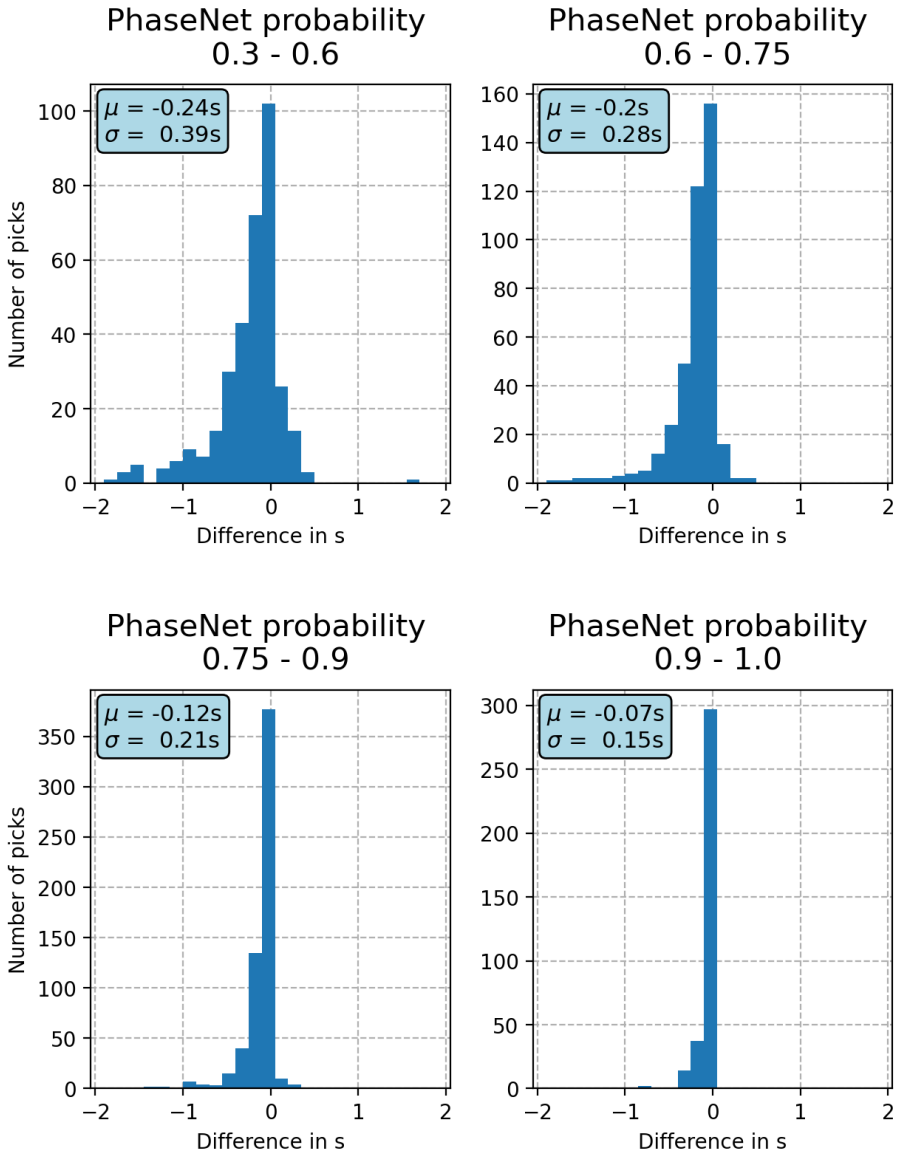

Figure 4.2.: Difference in determined *P*-phase onset time between the high precision manual pick catalog from Diehl et al. (2009a) and *PhaseNet*'s picks. Each panel corresponds to *PhaseNet* picks within the specified probability range.

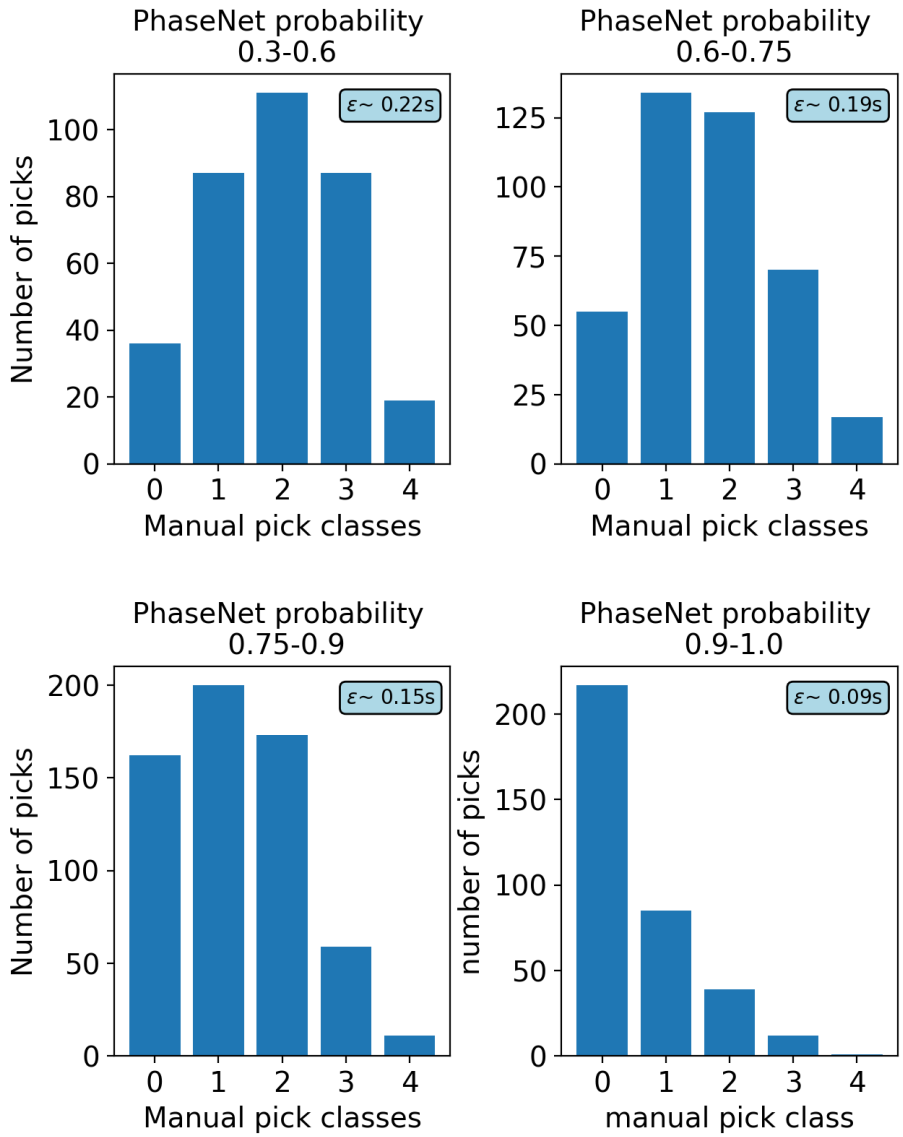

Figure 4.3.: Number of manually assigned pick classes for *P*-phases in Diehl et al. (2009a) for the four given *PhaseNet* probability ranges. The error estimate ε averages the accuracy values from 0.05 s - 0.4 s as assigned to each pick class in Diehl et al. (2009a) weighted by their occurrence in the corresponding probability range.

4.4.3. Event section plot

As an illustrative way to display the vast amount of seismic data available for this study we show an event section plot of a $M_L = 3.8$ event in NE Italy in Fig. 4.4(a). The trace normalized vertical components are shown over their epicentral distance. The travel time on the y-axis is corrected with the approximate upper-crustal *P*-wave velocity of $v_p = 6.0$ km/s, so that the arrival of the direct *Pg* wave is aligned horizontally. Synthetic onset times are computed with *NonLinLoc* (Lomax et al., 2000) based on the 1D P-wave velocity model from Diehl et al. (2009a) and a constant v_p/v_s-ratio of 1.73 and indicated with purple and pink horizontal bars for *P*- and *S*-phases, respectively. While *PhaseNet*'s *P*-phase picks as selected or discarded by the *2-fit method* (section 4.4.4) are shown in red and blue, respectively. *S*-phase picks are plotted in green (selected) and orange (discarded), accordingly. At distances from $\approx$200 - 450 km *PhaseNet* also frequently picks the later arriving direct *Pg*-phase that is often misidentified as an incoming *S*-phase (orange) possibly due to its shallow incidence angle. Similarly, the *Sn*-phase often seems to be mislabelled as a *P*-phase. Therefore, when applying the *2-fit-method* we are considering all *PhaseNet* picks at distances $\geq$200 km within $\pm$7 s of the synthetic *S*-phase onset to be *Sn*-phases regardless of their *PhaseNet* label. Those manually relabelled onsets are indicated by green circles with red edgecolor in Fig. 4.4(a).

4.4.4. Selection of a reliable data subset

The task of identifying and removing outliers in the data is of increased importance when dealing with an automatically picked catalog of arrival times usually containing more erroneous picks than manually picked data. In principle, this can be approached from the model as well as from the data side. Selecting outliers based on the model requires detailed *a priori* information of the region in order to remove picks based on their residual with respect to a certain reference model. Here, one has to be careful to not simply select picks that confirm the initial assumptions and discard data that contains valuable true signal, but deviates from the reference model.

To mitigate such a model anchoring, we developed a purely data driven approach. Fig. 4.4(b) illustrates our new *"2-fit-method"* applied to *P*-phase arrivals from the same event as in Fig. 4.4(a). Phase onsets are plotted over epicentral distance with their reduced travel time $v_{red} = 8.0$ km/s. Blue crosses mark the synthetic arrival time based on the 1D model from Diehl et al. (2009a) and green crosses draw a $\pm$ 7 s corridor around them. Since all picks outside of this corridor are discarded it has to be wider than the maximum expected signal amplitude. Initially, a weighted linear regression is fit through arrivals from 0 - 100 km and extrapolated. Picks within the blue corridor at distances $\geq$ 150 km within 4σ of this extrapolation are discarded as overcritical *Pg*-phases (cyan). Later arrivals (purple) are discarded as potential *PmP*-phases. Another weighted regression is fit through the remaining data between 250 - 700 km and extrapolated in both directions until it intersects the first fit for the direct arrivals. All arrivals

within 2σ of these two regressions are selected for the inversion and marked with red circles, while the remaining picks plotted as grey circles are not considered for further processing. In the case of multiple picks per trace, only the first arrival within the 2σ-range around the regression is selected. An example of this *"2-fit-method"* applied to *S*-arrivals is shown in Fig. A.5.
This approach requires a rather linear move-out of the direct *Pg*/*Sg*-wave which only is given for events shallower than ≈15 km. After manual inspection our *"2-fit-method"* yielded stable results for 384 events selecting a total of 39,599 *P* and 13,188 *S* observations.
Testing the *"2-fit-method"* on the reference data set from Diehl et al. (2009a) reduces μ = -0.15 s to μ = -0.09 s and σ = 0.27s to σ = 0.15s when comparing the manual picks to the initial and the selected *PhaseNet* picks, respectively.

While the number of *Pg*-phases picked by *PhaseNet* (Fig. 4.4(a)) matches the number of manually pickable onsets (see Fig. A.6) rather well, for all other phases the *PhaseNet* picks outnumber the manual ones. Out of all *PhaseNet* picks there are 410 *P*- and 178 *S*-phases selected, compared to the manual 286 *P*- and 68 *S*-onsets. Especially, the *Sn*-onset could not be manually determined at all and has been consistently picked as the overcritical *Sg*-phase, due to its low signal-to-noise ratio within the *P*-coda, in particular between ≈150 - 280 km epicentral distance (see Fig. A.6). The overcritical *Pg*- and *Sg*-phases are consistently picked by *PhaseNet* well beyond distances of 400 km. Since this study focuses purely on first arrivals we discarded them all. Nevertheless, they contain additional information that could be very valuable to studies incorporating secondary arrival picks.

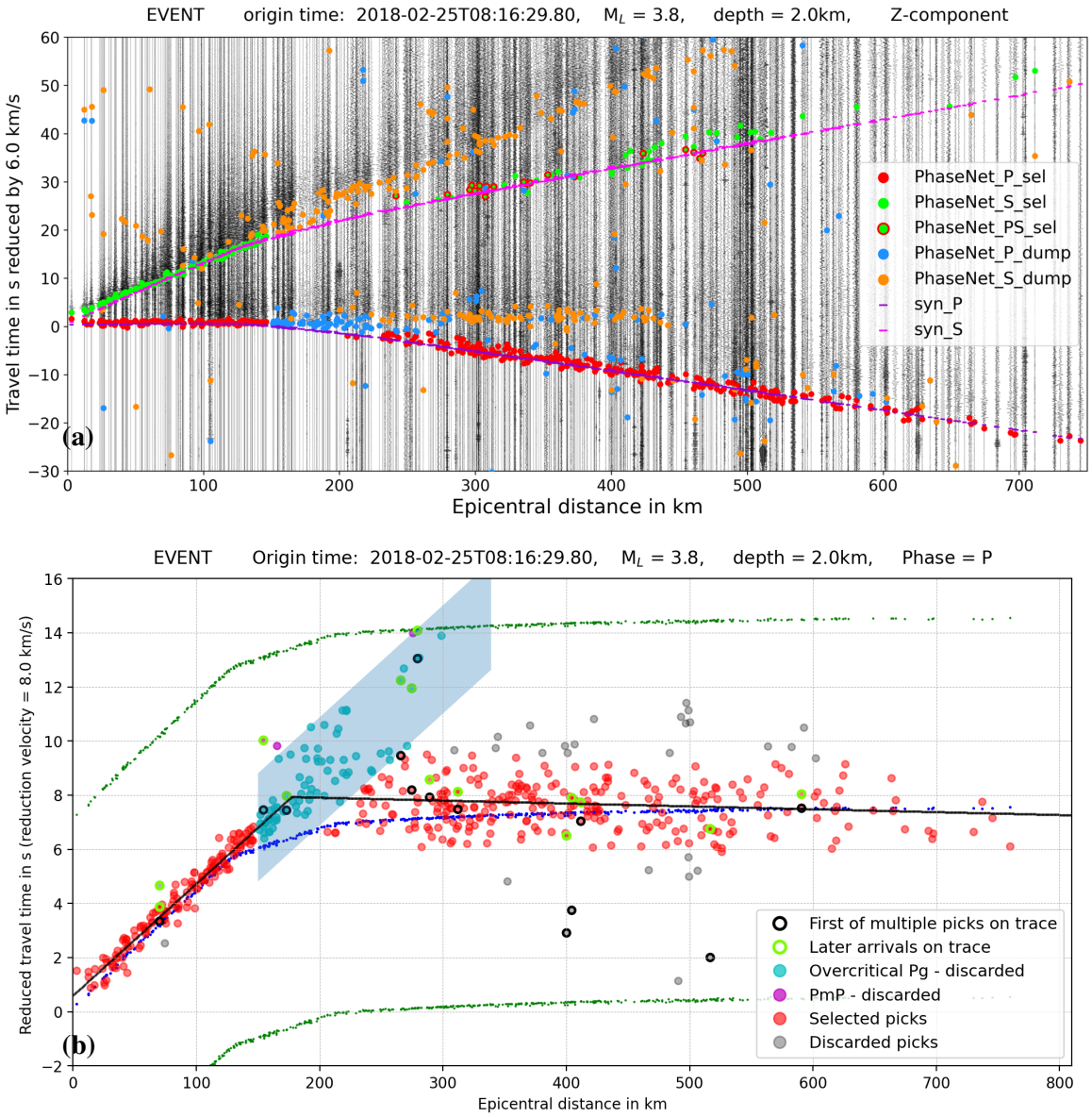

Figure 4.4.: **(a)** Event section plot showing the normalized traces of vertical components over their epicentral distance for a $M_L = 3.8$ event at 2.0 km depth in NE Italy. The travel times on the y-axes are corrected with the approximate upper-crust *P*-wave velocity of $v_p = 6.0$ km/s. Synthetic onset times based on the 1D *P*-wave velocity model from Diehl et al. (2009a) and a constant v_p/v_s-ratio of 1.73 are marked with purple and pink horizontal bars for *P*- and *S*-phases, respectively. *PhaseNet P*- and *S*-phase picks selected by the *2-fit method* are shown in red and green, while discarded *P*- and *S*-onsets are plotted in blue and orange, respectively. Green markers with red edgecolor are onsets that have been labelled as *P*-phases by *PhaseNet*, but are considered to be *Sn*-phases due to their proximity to the synthetic *S*-onset. **(b)** Illustration of the 2-fit method to discard erroneous picks. *PhaseNet P*-phase arrivals are plotted over epicentral distance with a reduction velocity of 8.0 km/s. The corridor of considered picks is marked with green crosses at ± 7 s around the synthetic onset (blue crosses) based on the 1D model from Diehl et al. (2009a). A linear regression is fit through the picks from 0 - 100 km and then extrapolated. All picks within the blue corridor at $\Delta \geq 150$ km within 4σ of this fit are labelled as overcritical *Pg*-phases (cyan) and discarded. Later phases with $\Delta \geq 150$ km are discarded as *PmP*-arrivals (purple). A second weighted linear regression is fit through arrivals from 250 - 700 km and extrapolated until its interjection point with the first fit. Arrivals within 2σ of the fits plotted in red are selected, while the remaining picks marked in grey are discarded. In the case of more than one arrival on the same trace, only the first arrival within 2σ of the fit is considered. First and later arrivals on the same trace are marked with black and lime edgecolors, respectively.

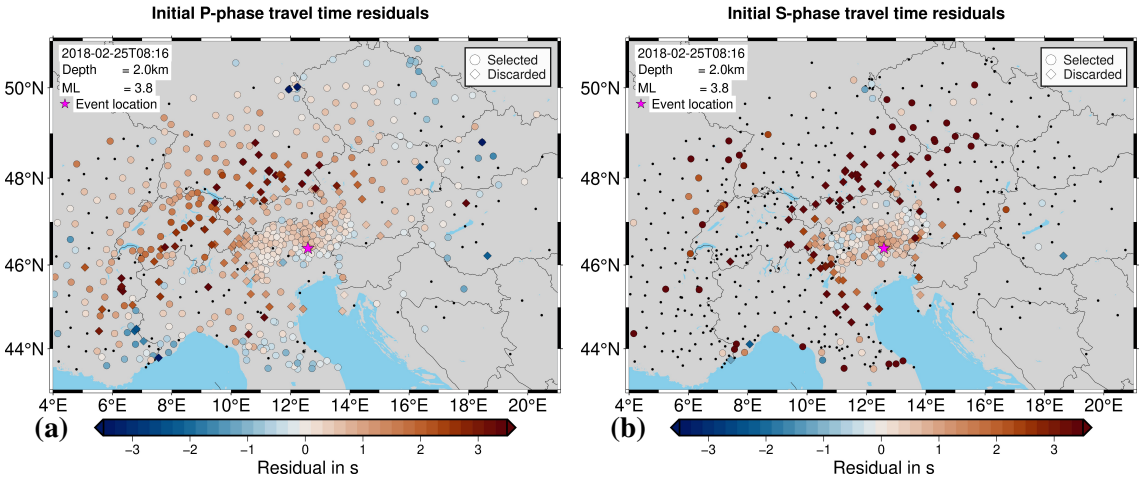

Figure 4.5.: Initial *P*- & *S*-phase travel time residuals of *PhaseNet* picks with regard to the 1D velocity model from Diehl et al. (2009a) for the same event as in Fig. 4.4. Onsets selected and discarded by the *2-fit method* are marked by circles and diamonds, respectively, while stations without phase picks despite available waveform data are denoted with black dots.

4.4.5. Spatial distribution of initial residuals

A map view of the *P* & *S*-phase residuals with respect to the 1D model from Diehl et al. (2009a) for the same event as in Fig. 4.4 is shown in Fig. 4.5. Black dots mark station locations where waveforms were recorded but no phase onset within the corridor of ± 7 s around the synthetic arrival time was detected by *PhaseNet*. Picks selected and discarded by the *2-fit-method* are marked as circles and diamonds, respectively. The map shows a rather smooth distribution of residuals with few contrasts between neighbouring stations. Overcritical *Pg*/*Sg*-phases are mostly showing up as (dark)red circles and are consistently identified and discarded. Around the cross-over distance on the western edge of the SWATH-D network some picks might have been wrongly discarded since they appear reasonable when compared to residuals from neighbouring stations. This is acceptable, though, since the main objective of this step is to select a set of reliable picks.

4.4.6. Computation of minimum1D models with *VELEST* and *McMC*

We apply two different algorithms to simultaneously invert for a minimum 1D *P*- & *S*-wave velocity model including station correction and hypocentral parameters from the selected seismic onset times. The *VELEST* (Kissling et al., 1994) code is well established for this task and requires an initial layered velocity model. While we use starting values for v_p from Diehl et al. (2009a) with slightly modified values in the upper mantle and an initial $v_p/v_s = 1.71$ based on an average of the model from Diehl et al. (2021), hypocentral parameters are taken from EPOS-EMSC. We tested ≈ 200 combinations for the 3 layer boundaries at depths between 15-45km in order to find the parametrization with the best fit for our data and did not apply additional damping to individual layers. Since the inverse problem is linearized iteratively around the given initial parameters substantial *a priori* information is necessary.

Additionally, we apply the Bayesian Markov chain Monte Carlo (*McMC*) algorithm as initially developed by Ryberg and Haberland (2019). The *McMC* approach explores the entire discretized model space for each parameter and updates one single model parameter per iteration step. While models that lead to a reduced misfit are always accepted, models with increased misfit can be accepted as well with a low probability to overcome local minima.

As a result, the model will converge towards the global minimum of the objective function within the defined model boundaries. Eventually, a certain number n of the best fitting models are statistically analyzed to obtain uncertainty bounds for each model parameter based on its variance through the final set of well fitting models. Due to the so-called transdimensionality of the algorithm the number of model layers as well as the location of layer boundaries is optimized during the inversion yielding a smooth, gradient-like velocity model.

Since no initial model is given and the model boundaries are widely set to $2.0\,\text{km/s} \leq v_p \leq 12.0\,\text{km/s}$ and $1.0 \leq v_p/v_s \leq 2.5$ only minimum *a priori* information is implemented leading to a data-driven exploration of the entire reasonable model space.

The workflow towards the minimum 1D models computed with *VELEST* and *McMC* is given in Table 4.2 and consists of three subsequent inversion runs.

The first run includes *P* and *S* phases with epicentral distances $\Delta \leq 130\,\text{km}$ for a spatially homogeneously distributed subset of 78 events in order to capture the average upper crustal *P* and *S*-wave velocity structure without introducing a bias towards areas of increased seismicity and thus denser ray coverage. In the second run we compute the final locations for all 384 events by fixing the velocities from the first run and relocating all events using a total of 16,351 *P* and 10,967 *S* phases with $\Delta \leq 130\,\text{km}$ following Diehl et al. (2021) who showed a decrease of hypocentre accuracy when including distant observations for earthquake localization. During the third run we fix the event locations and additionally include 23,248 *P* and 2,221 *S* observations with $\Delta \geq 130\,\text{km}$ in order to increase resolution in the lower crust and upper mantle. Station corrections and origin times are updated in each step and used as input for the subsequent run.

We perform one set of inversion runs with picks relatively weighted based on their *PhaseNet* probability and another one without weighting. There is no significant difference in the velocity structure and a standard deviation of $\sigma = 0.5\,\text{km}$ in the final epicentres with no systematic offset. Therefore, we decided to not include pick weights in our final models.

Table 4.2.: Overview of the workflow consisting of 3 subsequent inversion runs resulting in the final 1D v_p & v_s models, hypocentral parameters x, y, z & t_{org} and station correction terms τ^P & τ^S.

#run	model	v_p, v_s	x, y, z	t_{org}	τ^P, τ^S	#ev	Δ
run1		free	free	free	free	78	0-130 km
run2	*AlpsLocPS*	fix	free	free	free	384	0-130 km
run3	*GAR1D_PS*	free	fix	free	free	384	0-1000 km

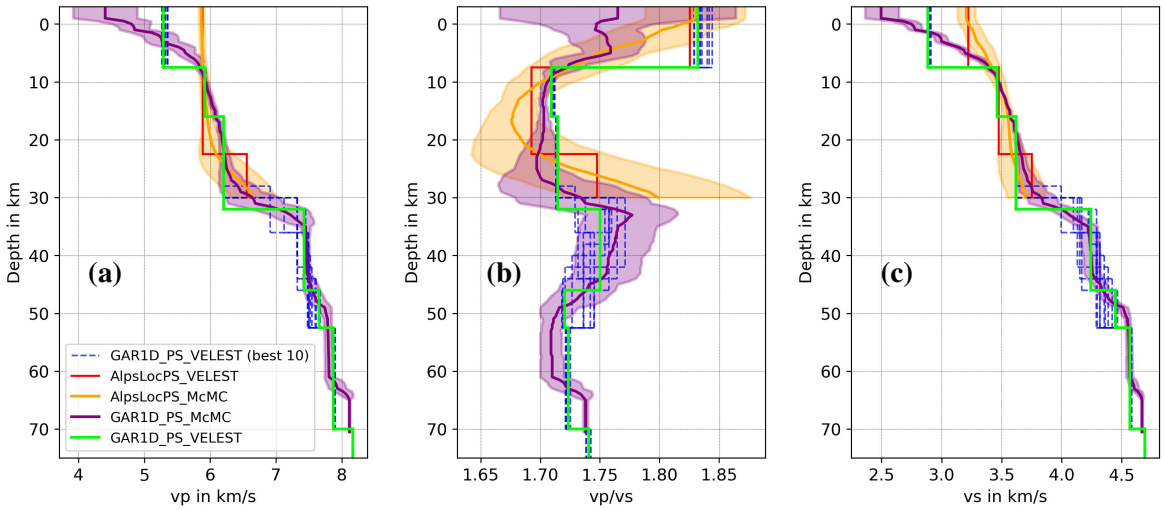

Figure 4.6.: Comparison of the *AlpsLocPS_McMC* (orange), *AlpsLocPS_VELEST* (red), *GAR1D_PS_McMC* (purple) and the 10 best fitting (blue, dashed) as well as the final best fitting (lime) *GAR1D_PS_VELEST* 1D velocity models. v_p, v_p/v_s & v_s distributions are plotted in panels (a), (b) & (c), respectively.

4.5. Results

4.5.1. *VELEST* and *McMC* minimum 1D models

Fig. 4.6 shows the 1D v_p, v_p/v_s & v_s distribution of the *AlpsLocPS_McMC* (orange), *AlpsLocPS_VELEST* (red), *GAR1D_PS_McMC* (purple) and the 10 best fitting (blue, dashed) as well as the final best fitting (lime) *GAR1D_PS_VELEST* models.

In general the resulting *P*-wave velocity models (Fig. 4.6(a)) match quite well, except for the uppermost crust where both *AlpsLocPS* models exhibit increased values and the *GAR1D_PS_McMC* model shows a gradual velocity increase contrary to the *GAR1D_PS_VELEST* model. The large velocity jump at 32 km depth in the *VELEST* model is somewhat smoother in the *McMC* model, which still contains a rapid increase of v_p between 28 - 34 km depth. In this depth range the uncertainty in the *GAR1D_PS_McMC* model as well as the deviation of the 10 best fitting *GAR1D_PS_VELEST* models is highest.

In the comparison of the derived v_p/v_s models (Fig. 4.6(b)) the largest discrepancy between all models again is present in the uppermost crust. For the remaining depth range the models are matching within their error margins with the highest uncertainty between 25 - 50 km depth.

Similar to v_p, the v_s structure of the *McMC* models (Fig. 4.6(c)) shows a gradual increase in the upper crust in contrast to the layered *VELEST* models with no systematic shift between the two, though. Below 10 km depth the models are matching very well with the highest uncertainty again between 25 - 50 km depth.

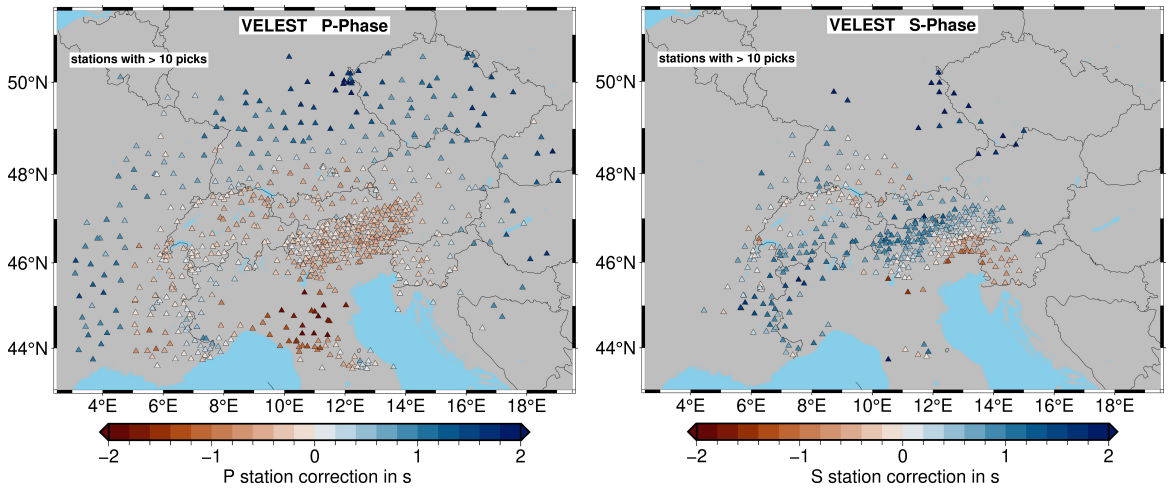

Figure 4.7.: *P*- & *S*-phase station correction terms corresponding to the 1D *VELEST* model based on observations from all distances.

4.5.2. *VELEST* and *McMC* event locations and station corrections

Since the *McMC* algorithm is not given any initial hypocentres a comparison with the *VELEST* locations can be seen as a "shift-test" which is commonly used to assess the dependency of final hypocentres from the initial locations. Resulting locations do not show a significant systematic shift and a horizontal and vertical scattering of $\sigma_{lat/lon} = 0.5$ km and $\sigma_{dep} = 2.3$ km, respectively (Fig. A.10).

The final *P*- and *S*-phase station corrections τ^P & τ^S of the *GAR1D_PS_VELEST* model are displayed in Fig. 4.7 and show a smooth trend rather than unreasonable small scale oscillations. They are in good agreement with station corrections of the *GAR1D_PS_McMC* (see Fig. A.9). Minor differences can be attributed to the fact that *VELEST* computes station corrections relative to a reference station with $\tau^P = 0.0$ s whereas *McMC* has the boundary condition of a zero mean value of all values of $\tau^{P/S}$.

In summary, both VELEST and McMC models are explaining the data similarly well and velocities as well as hypocentres are coinciding well within the uncertainties.

4.5.3. Residual analysis

Fig. 4.8 shows the remaining *P*- & *S*-phase residuals corresponding to the final *VELEST* model for several epicentral distance ranges. *P*-phase residuals show a normal distribution around negligibly small mean values μ and increasing values of standard deviations σ with increasing distances Δ ranging from $\sigma = 0.42$ s ($\Delta = 0$ - 70 km) to $\sigma = 1.03$ s ($\Delta = 300$ - 1000 km). For $\Delta \geq 150$ km no significant increase of the residual with distance is observed. *S*-phase residuals at $\Delta \leq 150$ km also follow a standard distribution with only slightly increased values compared to *P* residuals. At $\Delta \geq 150$ km *S*-residuals are showing a increased standard deviation while being strongly reduced in the number of observations.

In the following we present polar diagrams of remaining *P*-phase residuals observed at single stations. Fig. 4.9(a) shows residuals for station VARN in NE Italy displayed over their distance and BAZ range.

The distribution clearly clusters into a batch of predominantly negative residuals at $\Delta \leq 150$ km and another batch of predominantly positive residuals at $\Delta \geq 250$ km.

A comparable effect of BAZ dependent clusters can be seen in Fig. 4.9(b) displaying the remaining residuals of station WETR located in eastern Bavaria. While observations from the Southwest show negative residuals throughout, for arrivals from the South positive residuals are obtained.

A special focus of this study lies on the inaccuracy of the automatic *PhaseNet* picks that are obtained in the crustal cross-over distance of *Pg*-, *PmP*- & *Pn*-phases. Thus, we computed a set of 1D *VELEST* models with varying layer boundaries for a catalog including picks from all distances and for a catalog excluding the distance range from 130 - 300 km. The 20 best fitting models for both catalogs in Fig. A.7 show, that adding picks from the cross-over distance mainly impacts the resulting velocity models in the lower crust, but does not introduce a significant shift towards systematically higher or lower velocities in either model.

We assessed the remaining residuals of picks from all distances corresponding to the best fitting model computed when excluding the cross-over distance and find that picks in the cross-over distance do not show increased final residual values compared to observations from ≥ 300 km (see Fig. A.8). Therefore, all following models we present contain observations from the entire epicentral distance range.

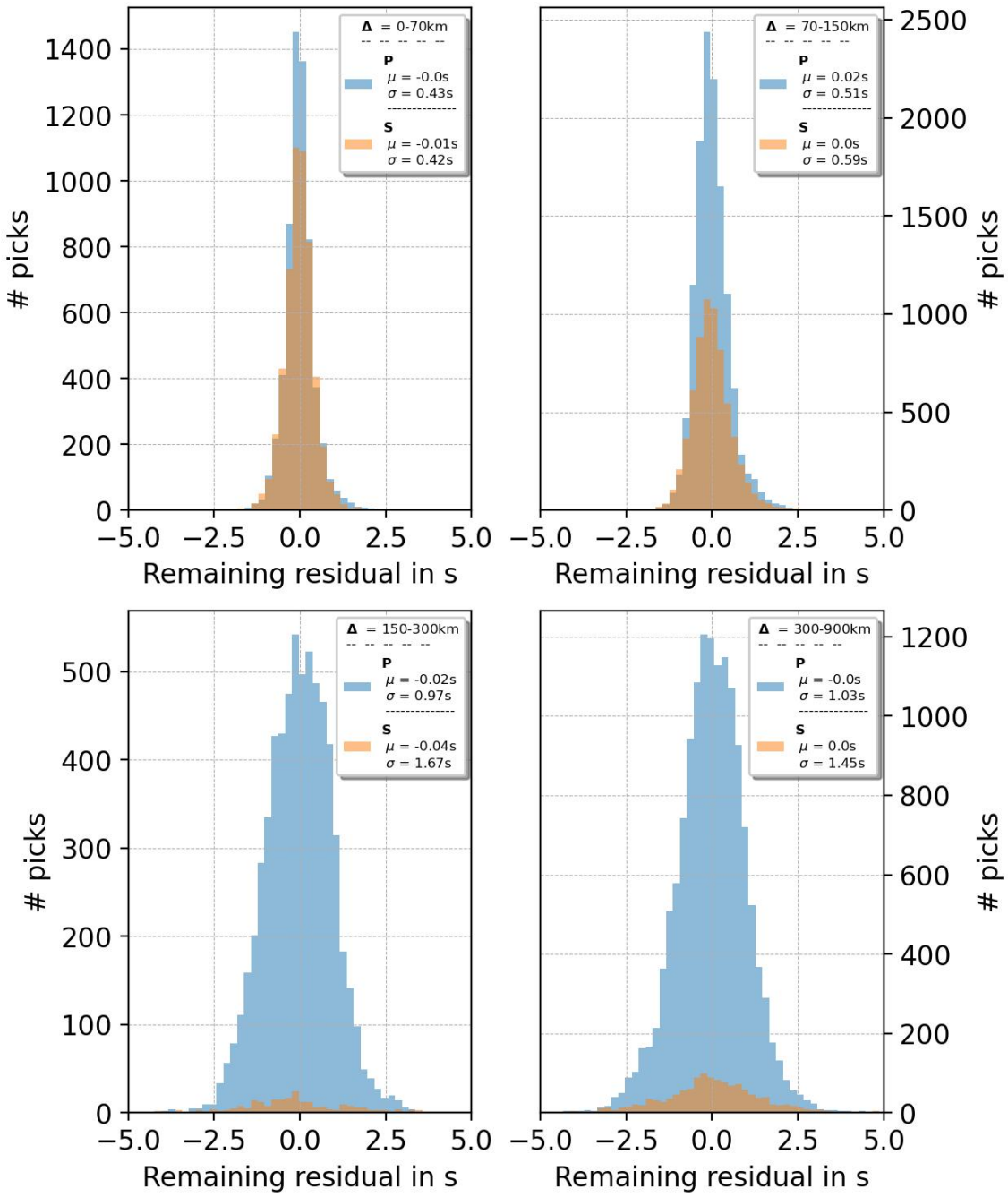

Figure 4.8.: Distribution of remaining *VELEST* residuals for *P*- (blue) and *S*-phases (orange) observed within several epicentral distance ranges.

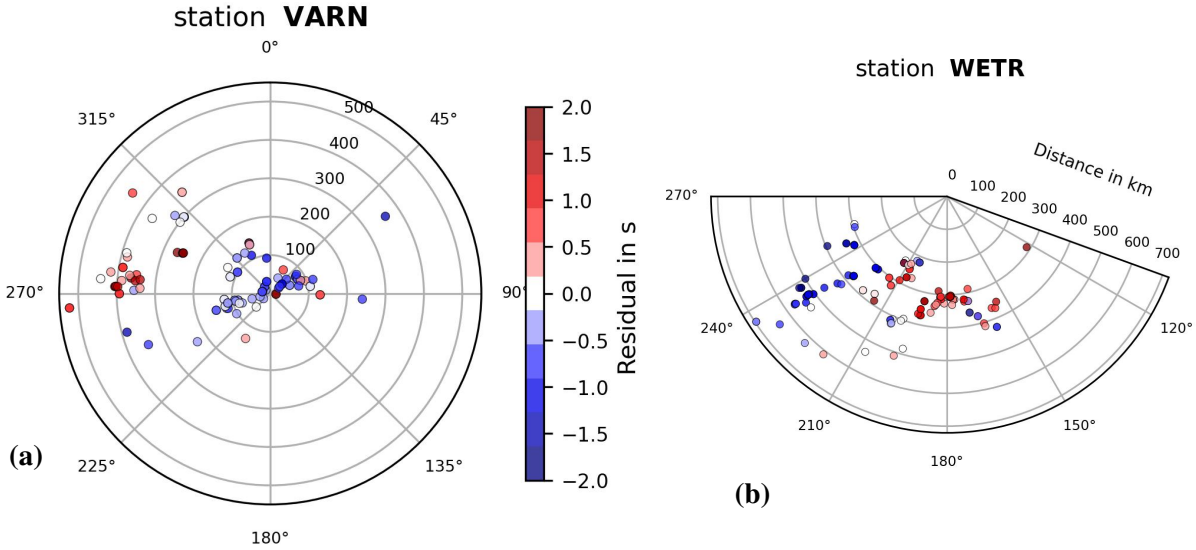

Figure 4.9.: Polar diagrams illustrating the spatial distribution of the remaining *VELEST P*-phase residuals over BAZ and distance observed at the stations *VARN* (NE Italy)**(a)** and *WETR* (SE Germany)**(b)**. Station locations are highlighted in Fig. 4.1.

4.6. Discussion

4.6.1. Static station corrections

We notice only mild variations of the *P* station corrections in the actual mountain range. In the contrary, larger variations of the S-station corrections are present, particularly in the SE we notice a prominent patch of negative station corrections. These match qualitatively with a region of elevated *vp*/*vs* ratio in the LET study by Jozi Najafabadi et al. (2022). As we include epicentral distances up to 1000 km in our *GAR1D_PS* model calculated station corrections (Fig. 4.7) are not only representing local site effects in the vicinity of each station but are systematically affected by large scale geologic structures of the GAR such as Moho topography. Stations along the northern edge of the network in central Germany exclusively record phases from distances ≥ 200 km travelling up-dip along a southward dipping Moho (Spada et al., 2012) systematically reducing their travel time. Therefore, static station corrections of $\approx$+2 s are most likely caused by Moho topography rather than local site effects. At stations with observations from near as well as far offsets such as station VARN in NE Italy a scalar station correction term is not sufficient to correct for distance-dependent residuals as illustrated in Fig. 4.9(a) leaving clusters of near and far observations with negative and positive remaining residuals, respectively. As Fig. 4.10 shows, this impact of *Pn*/*Sn* phases on the station corrections causes an increase of final residuals for *Pg*- and *Sg*-phases compared to their residuals after the relocation step where epicentral distances were limited to $\Delta_{max} = 130$ km. While *Pg*-phase residuals are almost doubling from $\sigma = 0.25$ s to $\sigma = 0.46$ s the increase in *Sg*-phase residuals from $\sigma = 0.44$ s to $\sigma = 0.51$ s is less prominent due to the smaller number of *Sn* observations impacting the final *S* station corrections. This suggests that the final static station corrections are not adequate to consistently correct for local site effects we recommend to use our intermediate model *AlpsLocPS* and its station corrections as published in the Supplement to locate seismicity within the GAR for *P*- & *S*-phases with epicentral distances $\leq$130 km. For events with a sufficient number of near observations, larger distances should not be considered anyway, due to the introduced increase of location uncertainty as shown by Diehl et al. (2021). In the following we will compare our *AlpsLocPS* & *GAR1D_PS* models to previous studies of the region.

4.6.2. Comparison of 1D velocity models

Fig. 4.11(a) shows the *GAR1D_PS_VELEST* (lime) and *GAR1D_PS_McMC* (purple) 1D v_p models of this study in comparison with previous models from Bagagli et al. (2022) (blue), Diehl et al. (2021)(dark-green) and Jozi Najafabadi et al. (2021) (cyan). The orogen wide model from Bagagli et al. (2022) is in good agreement with both our models showing no systematic offset and deviations due to different layering are mainly averaging out over depth. Generally, values of v_p are matching well between all models for the mid-crustal range between 10 - 20 km and are deviating slightly stronger above and below, which is consistent with the increased uncertainty of the *McMC* model in these depths. Deviations and increased uncertainties at shallow depths might be due to the high trade-off between station correc-

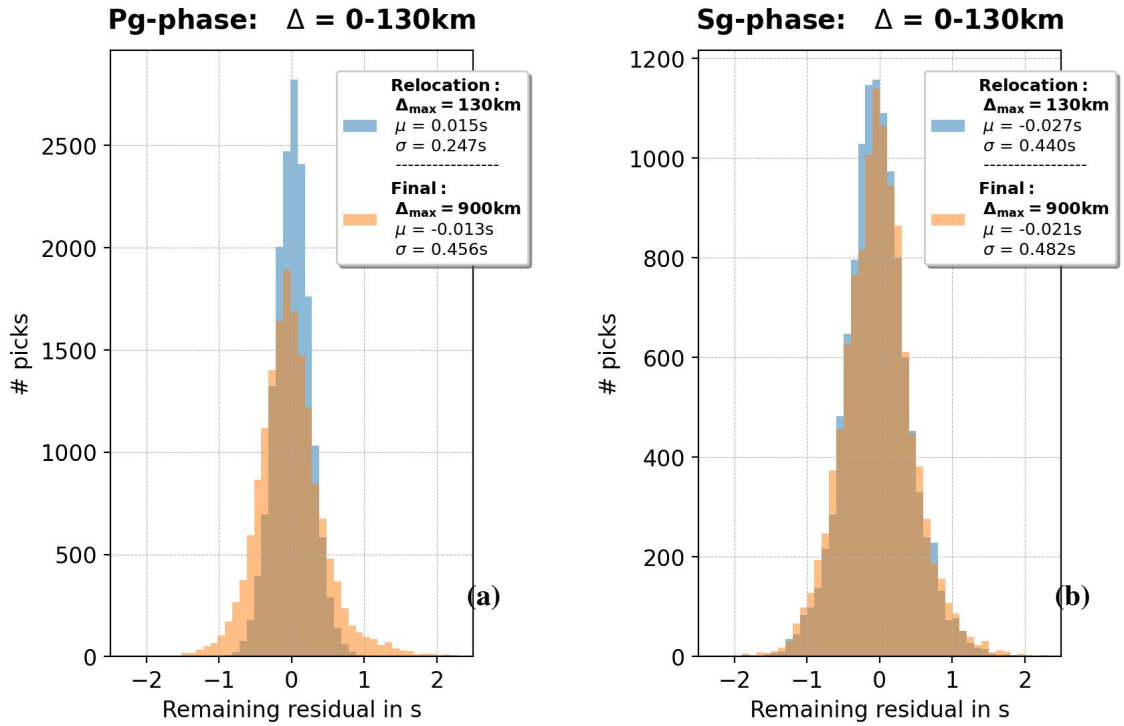

Figure 4.10.: **(a)** *Pg*-phase residuals with regard to the model after the relocation step (blue) and after the final inversion run (orange). **(b)** *Sg*-phase residuals with regard to the model after the relocation step (blue) and after the final inversion run (orange)

tions and velocity values in the upper crust.
Similarly, the v_p/v_s-ratio is well constrained for the mid-crustal range of 10 - 20 km depth as Fig. 4.11(b) demonstrates. Above and below this range the displayed v_p/v_s values are varying stronger. Fig. 4.11(c) compares the 1D v_s models derived in this work with the smaller scale studies from Jozi Najafabadi et al. (2021)(cyan) & Diehl et al. (2021)(darkgreen) and selected 1D profiles of 3D *S*-wave velocity models obtained from ambient noise studies by Kästle et al. (2018)(blue) and Sadeghi-Bagherabadi et al. (2021)(orange). The dashed, dotted and dash-dotted lines correspond to profiles from the Central Alps (46.85°N, 12.91°E), Po plain (45.05°N, 10.99°E) and Western Alps (45.85°N, 7.01°E), respectively, as marked in Fig. 4.1. Since these profiles are local representations of the velocity structure a detailed comparison with our models is not reasonable but represent the lateral variability in the GAR. The best agreement of all models is again visible in the mid-crust between 10 - 25 km depth followed by a range of increased deviation down to ≈45 km in accordance with the increased uncertainty of the *GAR1D_PS_McMC* model. As expected due to its thick sedimentary cover (Zuffetti and Bersezio, 2021), the profile from the Po plain shows significantly lower shallow velocity values.
From the comparison above we conclude that the average velocity structure of the GAR is determined most consistently in the depth range between 10 - 25 km. For shallower depths model velocities are deviating stronger partially due to the high trade-off between velocity and station corrections which themselves greatly depend on the epicentral distance range selected. Receiver function studies (Spada et al., 2012; Mroczek and Tilmann, 2021; Michailos et al., 2023) uniformly show large Moho topography ranging from 20 km in the northern Alpine foreland to more than 50 km beneath the Central Alps. As the substantial variations and uncertainties of the compared models within this depth range show, this large 3D structure can not be captured in a 1D model. Therefore, our models give a value of the average seismic velocities throughout the GAR. Below the maximum Moho depth of ≈55 km the models with sufficient resolution are in good agreement again.
Despite the mentioned issues, we present the first joined 1D *P*- & *S*-wave velocity model and associated station corrections for the GAR based on seismic travel times. This will serve as input for subsequent high resolution 3D tomographic study and provides consistent synthetic travel times e.g. useful for removing outliers in the pick catalog.

4.6.3. Comparison of hypocentres

In order to quantify the absolute accuracy of the determined event locations we compare our *VELEST* hypocentres to the results from Bagagli et al. (2022) and Jozi Najafabadi et al. (2021). A comparison of the 106 events matching between these two previous studies shows lateral variations of $\sigma_{lat} = 2.5$ km and $\sigma_{lon} = 2.1$ km with no significant systematic shift (Fig. A.11). Event depth scatters stronger with $\sigma_{dep} = 6.1$ km. Table 4.3 gives an overview of variations in event locations from Bagagli et al. (2022), Jozi Najafabadi et al. (2021) and our *VELEST* model. Deviations throughout the three comparisons are quite consistent with values of $\sigma_{lat}/\sigma_{lon}$ between 1.3 - 2.5 km and σ_{dep} between 5.8 - 6.3 km. Comparing

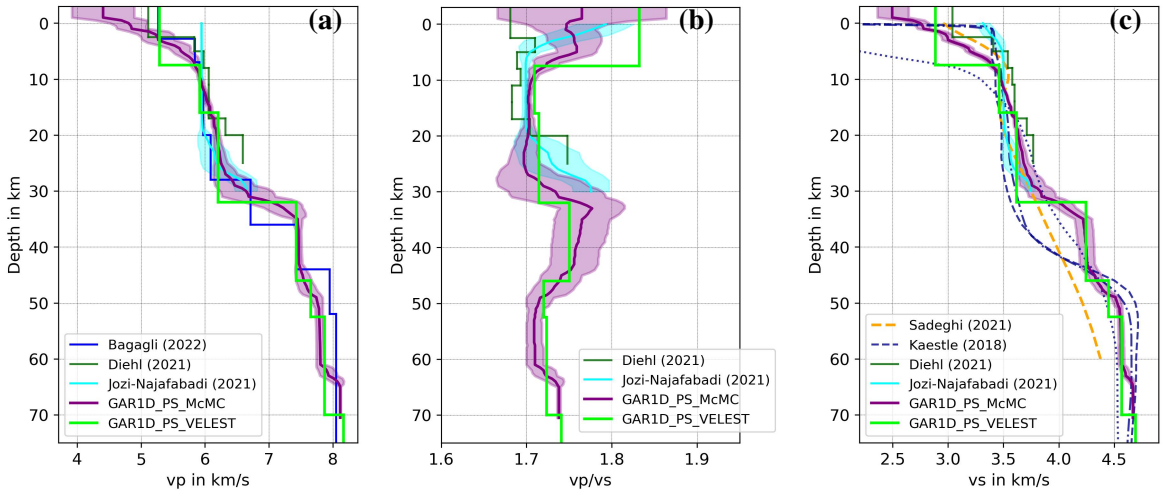

Figure 4.11.: Compilation of our *GAR1D_VELEST*(lime) and *GAR1D_McMC*(purple) 1D v_p, v_p/v_s & v_s models compared to results from previous studies within the GAR. **(a)** Comparison of our v_p models to the 1D models from Bagagli et al. (2022)(blue), Diehl et al. (2021)(darkgreen) and Jozi Najafabadi et al. (2021)(cyan). **(b)** Comparison of our v_p/v_s models to Diehl et al. (2021)(darkgreen) and Jozi Najafabadi et al. (2021). **(c)** Comparison of our v_s models to Diehl et al. (2021)(darkgreen), Jozi Najafabadi et al. (2021) and selected 1D v_s profiles from the 3D ambient noise studies from Kästle et al. (2018)(darkblue) and Sadeghi-Bagherabadi et al. (2021)(orange). The dashed, dotted and dash-dotted lines correspond to profiles from the Central Alps (46.85°N, 12.91°E), Po plain (45.05°N, 10.99°E) and Western Alps (45.85°N, 7.01°E), respectively.

the final *McMC* locations to the previous studies yields very similar offsets.

This indicates that events in the GAR generally can be located with a horizontal accuracy of $\approx$ 2km using a 1D velocity model including station corrections. Hypocentral depths are varying by $\sigma \approx 6$ km between all catalogs and are not more consistent when including *S*-phases as it has been done by Jozi Najafabadi et al. (2021) and this study. All referenced studies used their own picking methods and slightly different seismic stations which likely contributed to the rather large discrepancy in hypocentral depth. For more accurate event locations a denser station network and a consistent high resolution 3D velocity model is required as e.g. the local tomographic study of the Swiss region by Diehl et al. (2021) showed.

Table 4.3.: Comparison of deviations in event locations from Jozi Najafabadi et al. (2021), Bagagli et al. (2022) and our *VELEST* locations. For each pair of catalogs the number of matching events and the mean μ as well as the standard deviation σ for latitude, longitude and depth are listed.

	Jozi Najafabadi et al. (2021) vs. Bagagli et al. (2022)	Jozi Najafabadi et al. (2021) vs. *VELEST* this study	Bagagli et al. (2022) vs. *VELEST* this study
# events	106	40	307
σ_{lon} in km	2.1	1.5	1.3
μ_{lon} in km	-0.4	-0.2	-0.4
σ_{lat} in km	2.5	2.1	2.3
μ_{lat} in km	-0.6	-0.1	-0.7
σ_{dep} in km	6.1	5.8	6.3
μ_{dep} in km	-0.8	0.1	-0.1

4.7. Conclusion

In this work, we present joined 1D *P*- & *S*-wave velocity models including station corrections for the GAR based on seismic data from the *AlpArray Seismic Network* comprising more than 900 permanent and temporal seismic broadband stations. We assess the performance of several state-of-the-art deep neural network picking algorithms with the Seismology Benchmark collection *SeisBench* and find *PhaseNet* to be the most suited for our data set, especially due to its high recall on the test data.
Comparison of pick probabilities attributed to each pick by *PhaseNet* with the manually assigned pick classes in a high precision reference catalog show a clear correlation between *PhaseNet* probabilities and manual pick class as well as consistency of onset times of automatic and manual picks.
We developed a *2-fit-method* selecting picks based on their consistency in a data-driven way independently of *a priori* information such as an initial reference model. Choosing strict selection parameters allows us to consistently remove the overcritical *Pg*/*Sg* arrivals and thus include phases from the crustal cross-over distance increasing the resolution in the lower crust. Our final pick catalog contains 18,820 *P*- and 12,005 *S*-arrivals observed at epicentral distances from 0 - 150 km and 20,781 *P*- and 1,553 *S*-arrivals from 150 - 1000km.
We demonstrate how distant observations can overprint the influence of local site effects in station correction terms when minimizing the final remaining residual at the cost of increasing the misfit for near observations. Therefore, we publish the 1D *P*- & *S*-wave model *AlpsLocPS* including station corrections based on picks with epicentral distances from $\Delta = 0$ - 130 km for consistent event localization throughout the entire GAR and a second model *GAR1D_PS* with data from $\Delta = 0$- 1000 km resolving the entire crust and uppermost mantle allowing the computation of synthetic *P*- & *S*-phase travel times for the GAR.
A comparison of hypocentres determined in this work with locations of matching events from other studies shows epicentral uncertainties of $\sigma_{lon/lat} \approx 1.5$ - 2.5 km and variations in hypocentral depth of $\sigma_{dep} \approx 6.0$ km.

5. 3D crustal *P*- and *S*-wave velocity model of the Alpine mountain chain

This chapter describes the computation of the 3D crustal *P*- and *S*-wave velocity model of the Greater Alpine region and the northern Apennines based on the previously presented *GAR1D_McMC* 1D *P*- and *S*-wave model as initial velocities. Event detections and starting hypocentral parameters are mainly based on Bagagli et al. (2022) and complemented by detections from national agencies where necessary. Similar to the workflow for the 1D model, I am using *PhaseNet* (Weiqiang and Beroza, 2018) to determine seismic phase arrivals and apply the *2-fit-method* for pre-inversion pick selection. I conduct 750 individual inversion runs each with slightly different initial parameters and grid spacings. By averaging over the best 20 models, I obtain a smoother final model minimizing the dependency on a single - to some extend always arbitrarily chosen - model parametrization.
Based on the final 3D velocity model, I address remaining questions regarding the crustal velocity structure of the Alpine orogen. I present seismic evidence for stacking of European and Adriatic crust during continental collision and show the seismic signature of the Adriatic indenter in the Southeastern Alps in unprecedented resolution.

This chapter is currently under preparation to be submitted as a research article.

5.1. Abstract

We present the first comprehensive crustal 3D *P*- and *S*-wave velocity model of the Greater Alpine region (GAR) based on Local Earthquake tomography. Leveraging the unprecedented wealth of seismological data recorded by the AlpArray Seismic Network and complementary experiments this study analyzes seismic broad-band waveforms from 989 stations in the GAR between 2016-2022. We apply the neural network based seismic picking algorithms *PhaseNet* and obtain a total of 173,841 *P*- and 68,967 *S*-phase onsets from 2553 events with $M_L \geq 1.5$ recorded at epicentral distances up to 1000 km. With the SIMUL2023 algorithm we simultaneously relocate the seismicity and invert for the 3D velocity structure of the crust and uppermost mantle. Starting hypocentral parameters and the initial 1D velocity structure are perturbed randomly within their uncertainty estimates. We run a total 750 inversions with variable horizontal and vertical grid parametrizations and define the final model as the average of the 20 inversions with the lowest data misfit. The averaged model shows smoother image of velocity anomalies which is less dependent on a single - often somewhat arbitrarily chosen - model parametrization.

First order anomalies such as foreland basins and the Ivrea body generally agree well with previous studies. We image a crustal root with depths of ≈60 km beneath the Western and Central Alps with a shallowing Moho towards the East. A prominent novel feature is a consistent decrease in *P*- and *S*-wave velocity at mid crustal depths beneath the Western and Central arc. Due to its partial connection to the upper crust in the European foreland we interpret this to be formerly European upper crustal material which has been stacked during the collision process.

5.2. Introduction

With the closing of the Alpine Tethys at 35 Ma, the Europe-Adria plate boundary was transformed into a NW–SE oriented continental collision zone along which the Alpine mountain chain began to form (Handy et al., 2010; Carminati et al., 2012). Subsequently, Miocene counterclockwise rotation of the Adriatic plate relative to Europe and Africa caused a change in convergence direction from NW–SE to WNW–ESE and a decrease in convergence velocity in the Central and Eastern Alps relative to the Western Alps (Dewey et al., 1989). As a result, increased crustal shortening in the Western and Western Central Alps has lead to a crustal root of ≈60 km thickness (Spada et al., 2012). Shallower Moho depths in the Eastern Alps are a consequence of eastwards extrusion of crustal material towards the Pannonian basin (Ratschbacher et al., 1991).

A simplified map of the present geological setting in the Greater Alpine region (GAR) including the main tectonic units and fault lines is shown in Figure 5.1. The northern and southern Alpine foreland regions are characterized by the sedimentary Molasse and Po basin, respectively. A well-known feature at the western end of the Po basin is the Ivrea body which is imaged clearly by seismic (Thouvenot et al., 1996; Diehl et al., 2009a; Solarino et al., 2018) and gravity studies (Bayer et al., 1989). It consists of oversteepened Adriatic mantle material overlying the eastwards subducting European crust (Zhao et al., 2020). In the Southeastern Alps, the Adriatic indenter located on the northern part of the Adriatic plate indented into the European plate causing the W-E oriented Periadriatic fault to be offset sinistrally by the Giudicarie line (Pomella et al., 2012).

Within the scope of the recent interdisciplinary AlpArray/4DMB project a wide range of geoscientific studies have been conducted to further advance the understanding of the orogenesis of the European Alpine mountain chain. Therefore, the AlpArray Seismic Network (AASN) (Hetényi et al., 2018) and the complementary SWATH-D (Heit et al., 2021) & CIFALPS2 networks (Zhao et al., 2018) have been installed across the GAR providing an unprecedented uniform broad-band station spacing of ≈50 km (Fig. 5.1). In this study, we combine this extraordinary data set and the rapid improvement of machine learning based seismic picking algorithms (Weiqiang and Beroza, 2018; Mousavi et al., 2020; Woollam et al., 2022). We use the deep neural network *PhaseNet* (Weiqiang and Beroza, 2018) to determine *P* - and *S*-phase arrivals at distances up to 1000 km and subsequently compute the first uniformely processed orogen-wide 3D crustal *P*- and *S*-wave veloctiy model of the Alpine mountain chain and the northern Apennines.

Aside from contributing to future studies, our model directly addresses open questions regarding the crustal structure of the GAR. We assess large scale differences in the velocity structure along the Alpine arc, especially at mid and lower crustal depths and image the seismic signature of the Adriatic indenter in much higher detail than previous studies (Diehl et al., 2009a; Kästle et al., 2018).

Based on the AASN several recent studies have been imaging the upper mantle structure beneath the GAR. Albeit they consistently show evidence for subducted lithosphere, its precise configuration and the potential presence of slab detachment is still under debate. Zhao et al. (2016a) and Malusà et al. (2021) argue for a continuous European slab while Kästle et al. (2018); Paffrath et al. (2021); Handy et al. (2021) find evidence for a tear or partial detachment. A priori knowledge of the 3D crustal structure is crucial to achieve the optimal resolution in teleseismic travel time tomography studies (Kissling, 1993). Lacking a uniformely processed, comprehensive 3D *P*- and *S*-wave crustal model of the GAR, Paffrath et al. (2021) had to combine two separate crustal models with different resolution and parametrization to correct for the crustal travel time effects. Thus, our high resolution model will be valuable for future teleseismic tomography studies or the reassessment of existing data sets (e.g. Paffrath et al. (2021); Plomerová et al. (2022). Furthermore, it will improve the precision of depth migration in receiver function studies (Mroczek and Tilmann, 2021) and potentially serve as a starting model for full waveform inversion applications.

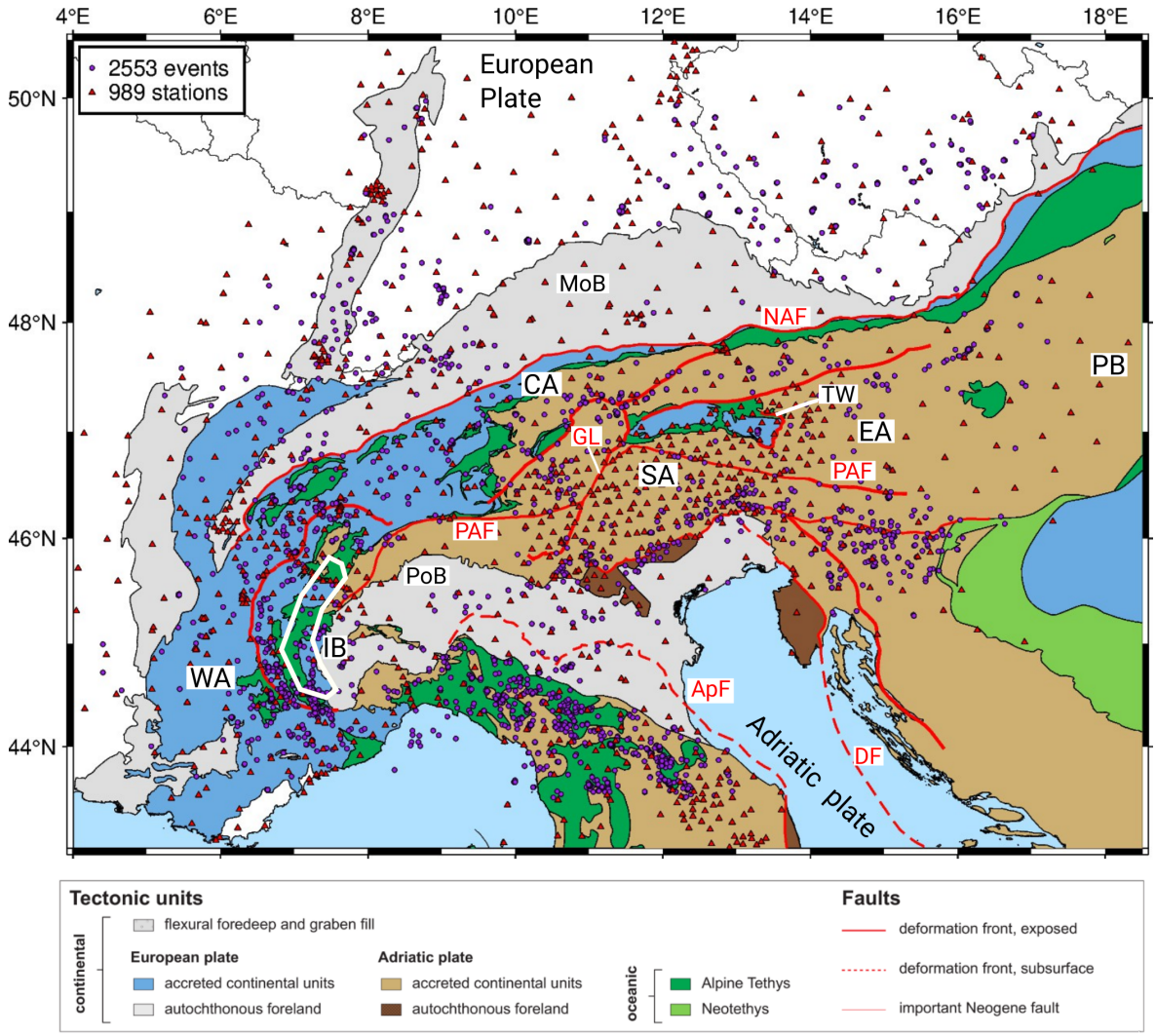

Figure 5.1.: Tectonic map for the Greater Alpine region based on units and major lineaments simplified from Schmid et al. (2004, 2008); Handy et al. (2010, 2014, 2019); Bigi et al. (1990); Froitzheim et al. (1996); Bousquet et al. (2012). The dense station spacing of the AASN (Hetényi et al., 2018) is complemented by the SWATH-D (Heit et al., 2021) and CIFALPS2 (Zhao et al., 2018) networks leading to a total of 989 seismic broad-band stations with $\geq$5 observations. 2553 events with $M_L \geq$1.5 between 01/2016-12/2022 are predominantly based on Bagagli et al. (2022) and augmented by EPOS-EMSC (*https://www.seismicportal.eu/*), RESIF (*https://franceseisme.fr/*) and INGV (Arcoraci et al., 2020). NAF - Northern Alpine Front, PAF - Periadriatic Fault, GL - Giudicarie line, DF - Dinaric Front, ApF - Apenninic Front, TW - Tauern Window, PoB - Po Basin, MoB - Molasse Basin, PB - Pannonian Basin, WA - Western Alps, CA - Central Alps, SA - Southern Alps, EA - Eastern Alps, IB - Ivrea body.

5.3. Data & Methods

This section gives an overview of the overall workflow including data processing, seismic phase picking and details on the inversion technique.

5.3.1. Waveform data

We collected waveforms recorded by a total of 1252 seismic broad-band stations within the GAR between 01/2016-12/2022. The majority of stations belongs to the AASN (Hetényi et al., 2018) which has been installed within the interdisciplinary European AlpArray research initiative. Additionally, we use data from the SWATH-D (Heit et al., 2021) and CIFALPS (Zhao et al., 2018) temporal deployments. All station XML data and raw waveform data were downloaded via the ObsPy FSDN Clients (Krischer et al., 2015) of the data hosting institutions. We only consider 3 component stations with a sampling rate of ≥ 100 Hz and channels of either "HH?", "BH?" or "EH?". We resample all data to 100 Hz which is the required input sampling rate of the deep neural network *PhaseNet* (Weiqiang and Beroza, 2018) used for automatic phase arrival time determination.

5.3.2. Event catalog

The comprehensive seismicity analysis of the GAR from Bagagli et al. (2022) provides uniformly processed initial hypocentral parameters for the time period from 2016-2019. For the years from 2020-2022 we obtained event detections and starting locations from the EPOS-EMSC (*https://www.seismicportal.eu/*), RESIF (*https://franceseisme.fr/*) and INGV (Arcoraci et al., 2020) accessed through the ObsPy FDSN Client and removed duplicates between the catalogs.
We consider events with $M_L \geq 1.5$ yielding an initial catalog consisting of 4580 events between 2016-2022.

5.3.3. Seismic Phase picking

In our previous work (Braszus et al., 2024) we inverted for 1D velocity structure of the GAR and assessed the performance of some of the most commonly applied AI seismic picking algorithms using the *SeisBench* toolbox (Woollam et al., 2022). We compared a high precision manual *P*-phase pick catalog from the broader Swiss area from (Diehl et al., 2009a) to *PhaseNet* (Weiqiang and Beroza, 2018), *EQ-Transformer* (Mousavi et al., 2020) and *GPD* (Ross et al., 2018) each retrained on several benchmark data sets as included in *SeisBench*. Based on a combination of accuracy, recall rate of manual picks and additional phases we find *PhaseNet* in its original version to perform best and decide to use it for seismic arrival time determination.

Table 5.1.: Comparison of *PhaseNet* against manual *P*- and *S*-phase picks for several epicentral distance ranges.

P-phases				**S-phases**			
Δ in km	# picks	σ in s	μ in s	Δ in km	# picks	σ in s	μ in s
0-70	2140	0.09	-0.02	0-70	1489	0.26	0.03
70-150	2989	0.21	-0.05	70-150	1315	0.38	0.09
150-300	2812	0.27	-0.03	150-300	847	0.57	0.02
300-1000	2354	0.26	0.00	300-1000	119	0.59	0.14

Additionally, we compared *PhaseNet P*- & *S*-phase onset times to our manual reference pick catalog including 10,295 *P*- & 3,770 *S*-picks from 30 events of this study. The deviations of *PhaseNet* and manual picks are summarized in Table 5.1 and shown in Figure B.1. Averaging over observations from all distances leads to an estimated pick accuracy of $\sigma_{pick,P} = 0.23$ s and $\sigma_{pick,S} = 0.40$ s for *P*- and *S*-phases, respectively. The final data variances of $\sigma^2_{d,P} \approx 0.18\,\mathrm{s}^2$ and $\sigma^2_{d,S} \approx 0.22\,\mathrm{s}^2$ after the inversion still are significantly larger than the pick variances of $\sigma^2_{pick,P} = 0.05\,\mathrm{s}^2$ and $\sigma^2_{pick,S} = 0.16\,\mathrm{s}^2$ which indicates that model updates are still based on a distinguishable signal and no overfitting is taking place.

5.3.4. Pre-inversion pick selection

In order to consistently remove outliers and secondary phase arrivals from our pick catalog, we modified the *2-fit-method* developed by Braszus et al. (2024) as illustrated in Figure 5.2. This data-driven pre-inversion pick selection method plots the reduced travel time over hypocentral distance and fits weighted linear regression lines through the *Pg* & *Pn* arrivals between 0 - 100 km & 250 - 700 km, respectively. Onsets within 4σ of the extrapolated *Pg* fit at distances $\geq$150km (blue corridor in Figure 5.2) are not considered for the *Pn* fit. Arrivals within 2σ of the fits are selected while the remaining picks are discarded. In contrast to the previous version (Fig. 5.2, left) we do not categorically remove picks within the blue corridor, but select them if they are within 2σ of their corresponding fit. For further detail on the *2-fit-method* we refer to section 3.4 in Braszus et al. (2024). The application of the *2-fit-method* to *S*-phases is shown in Fig. B.2. Here, *P*-phases close to the synthetic *Sn* onset are considered to be *S*-phases which have been mislabelled by *PhaseNet*. All plots generated by the *2-fit-method* are inspected manually and events with unreasonably sloped regression lines are discarded entirely.

We consider events with ≥ 8 *Pg*- & ≥ 4 *Sg*-phases which yields a catalog of 2373 earthquakes and leaves an area of poor coverage in the Po plain in Northern Italy. For this region we loosen the criteria to ≥ 8 *Pg*-phases only and thus add 180 events ensuring a more uniform ray coverage of the model space. Eventually, we discard events with a *GAP* $\geq 180°$, stations with <5 observations and all *S*-phases without a corresponding *P*-onset.

Table 5.2 lists the number of events for which arrivals from a certain phase could be extracted using the

Table 5.2.: Number of events and picks per phase that were selected by the *2-fit method*.

Phase	# events	# picks
Pg	2553	88,600
Sg	2373	55,921
Pn	837	85,241
Sn	384	13,046
Total:	2553	242,808

2-fit-method. The final locations of the 2553 events and 989 stations with ≥5 phase records are shown in Figure 5.1.

5.3.5. Tomographic Inversion

We are using *SIMUL2023* (Eberhart-Phillips et al., 2024) which is the most recent version of the well-established *SIMULPS* algorithm (Thurber, 1983; Eberhart-Phillips, 1990) to simultaneously invert for hypocentral parameters and the *vp* and *vp/vs* structure of the model space. SIMUL2023 linearizes the coupled hypocentre-velocity problem around a starting model and iteratively minimizes the travel time residuals using a damped least squares approach. In each iteration step ray-tracing is performed by an efficient pseudo-bending algorithm (Um and Thurber, 1987). The model is parametrized on nodes which are located on the intersections of a rectangular grid. The velocity at an arbitrary point within the model space is defined by a linear B-spline interpolation of neighboring node values yielding a spatially smooth distribution of model parameters.

Large distance observations can potentially negatively impact the hypocentral accuracy when included for seismicity (re)location (Diehl et al., 2021). Therefore, in a first inversion step we relocate the seismicity and invert for the upper crustal velocity structure using *P*-phases with $\Delta \leq 130$ km and *S*-phases with $\Delta \leq 80$ km. The resulting velocity model and hypocentral parameters are used as input for the second inversion step which is including picks from all distances while keeping the event hypocentres fixed and only updating the origin time. We are not inverting for station correction terms. In both inversions we are fixing the velocity at the outermost nodes and applying a constant linking to neighboring nodes in areas of poor resolution as indicated by the spread values (Fig. B.3) which results in 12,053 independent velocity model parameters. We calculated trade-off curves for damping of *vp* and *vp/vs* for both inversions (Fig. B.4) and select damping values of $\lambda_{p1} = 1000$; $\lambda_{ps1} = 1000$ and $\lambda_{p2} = 5000$; $\lambda_{ps2} = 4000$, respectively. In the following we will refer to the subsequent execution of these two inversion steps as one single inversion run.

Based on checkerboard reconstruction tests for several parametrizations, we choose a horizontal node

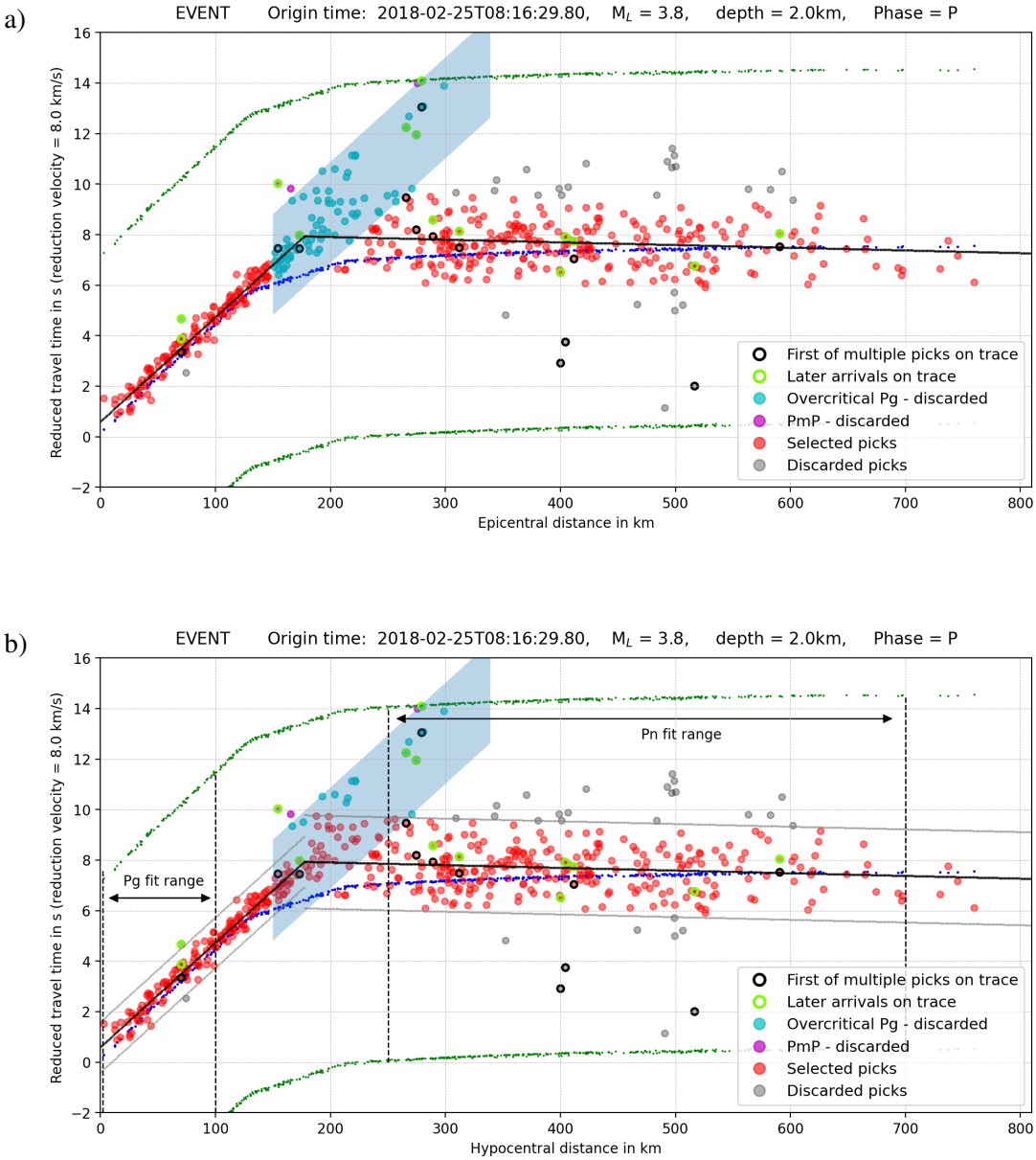

Figure 5.2.: a) Initial version of the *2-fit method* as developed by Braszus et al. (2024) for pre-inversion pick selection. b) Updated version of the *2-fit method* as used in this study. Potential overcritical *Pg*-phases within 4σ of the extrapolated *Pg*-fit at distances $\geq$150 km (blue corridor) are not categorically discarded anymore. Instead, if they lie within 2σ of their corresponding regression line they are selected. Furthermore, travel times are now plotted over hypocentral instead of epicentral distance ensuring a more linear moveout of the direct *Pg* arrivals for deeper crustal events. For a detailed description we refer to Braszus et al. (2024).

spacing of 25 km. Regarding the vertical node spacing, we find models with either 6 or 7 nodal planes between 0 - 70 km depth to be most suitable. Models with larger spacing show a significantly increased data misfit, while a finer spacing introduces vertical smearing and insufficient reconstruction of synthetic models.

We determine the optimal vertical node spacing by running 750 inversions with variable node depths. Initial v_p velocities are taken from Braszus et al. (2024) who used a Markov chain Monte Carlo (McMC) approach (Ryberg and Haberland, 2019) to compute the *GAR1D_McMC P*- and *S*-wave 1D model for the Alpine region including statistical uncertainties. We use a constant initial v_p/v_s ratio of 1.71 representing the average value of the *GAR1D_McMC* and perturb the initial v_p of each individual model by $\pm 1\sigma$ of the *GAR1D_McMC* model. Similarly, initial event locations are shifted horizontally and vertically by $\sigma_{hor} = 2.0$ km and $\sigma_{ver} = 6.0$ km based on the hypocentre uncertainty estimates of Braszus et al. (2024). Additionally, in each single run the entire grid is shifted randomly in x- and y-direction by ± 12.5 km which is equal to half the horizontal node spacing.

The evolution of data misfit over 20 iterations for 750 runs each with 6 and 7 layers is shown in Figure 5.3. Solid, dotted and dashed lines refer to the median, 10% quantile and minimum data variance, respectively. The variance reduction is largest in the first 5-6 iterations and significantly slows down after $\approx$10 iterations with only marginal improvements. We therefore consider the set of 750 runs with 7 layers after 13 iterations for the final step where we average the best 20 models. Thus, the final model is smoother and not dependent on a single parametrization . Averaging over a lower or higher number of individual models does not significantly affect the final result as shown in Figure B.5. This indicates the robustness of the inversion, since each single run has been computed with shifted initial hypocentres, a perturbed 1D starting model and varying horizontal and vertical model parametrization.

Figure 5.4 shows the vertical node distributions that are yielding the smallest data variance for 7 layers between 0 - 70 km and 13 iterations. Based on a previous test with completely arbitrary node distribution, we limit the range of randomly generated parametrizations to models with three nodes between 5 - 35 km, one node between 35 - 45 km and one node between 45 - 57 km. Since the final model is based on an average of 20 parametrizations we define a reference layering with nodes at 0, 10, 18, 28, 40, 55 and 70 km resembling the average node depths of the best 20 models. This reference layering is used in the following chapter to assess the model resolution based on the spread value of the model resolution matrix and reconstruction tests.

5.3.6. Hypocentre relocation

SIMUL2023 linearizes the coupled hypocentre-velocity problem around an initial model and iteratively updates hypocentres and velocity structure. Thus, it is crucial to evaluate the influence of the initial parameters on the final inversion result. A common way to do this are hypocentre shift tests (Haslinger et al., 1999; Husen et al., 1999) where initial hypocentres are moved horizontally and vertically in order to quantify the robustness of the resulting event locations and velocity models. If slight changes

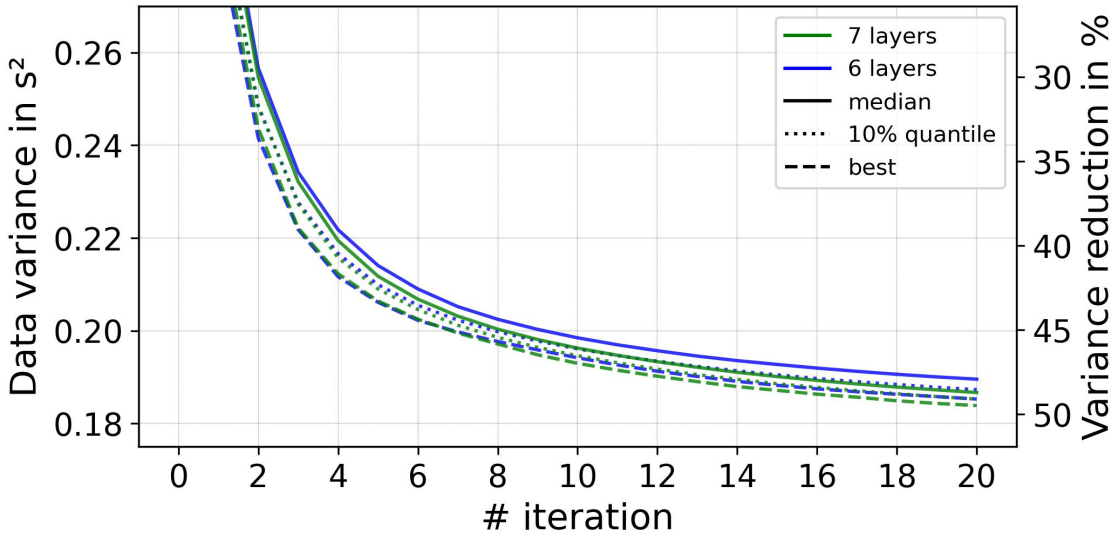

Figure 5.3.: Evolution of data variance over number of iterations for 750 horizontally and vertically shifted parametrizations with 6 layers (blue) and 7 layers (green) between 0 - 70 km. Solid, dotted and dashed lines indicate the variances of the median, 10% quantile and best models, respectively.

of the initial parameters lead to a strong variation in the inversion output, this would indicate an instable result. Our inversion approach as described in the previous section enhances the conventional shift test by additionally varying the initial 1D model within its uncertainties and testing a wide range of grid parametrizations. Each single event in each run has initially been shifted with $\sigma_{hor} = 2.0$ km and $\sigma_{ver} = 6.0$ km. Final locations for the best 200 out of all 750 runs are deviating by less than $\sigma_{hor} = 0.5$ km and $\sigma_{ver} = 3.0$ km for almost all events which indicates the robustness of the resulting hypocentres (Fig. B.6).

Similar to the velocity model, we define our final event locations as the average hypocentral parameters of the 20 inversion runs with the lowest data misfit. The comparison of initial and final hypocentres yields deviations of $\sigma_{lat} = 1.67$ km, $\sigma_{lon} = 1.38$ km and $\sigma_{dep} = 4.67$ km in latitude, longitude and depth, respectively. This is in agreement with Braszus et al. (2024) who quantified the horizontal and vertical hypocentre accuracy as $\sigma_{hor} \approx 2.0$ km and $\sigma_{ver} \approx 6.0$ km, respectively, when using a 1D velocity model including station corrections for the GAR.

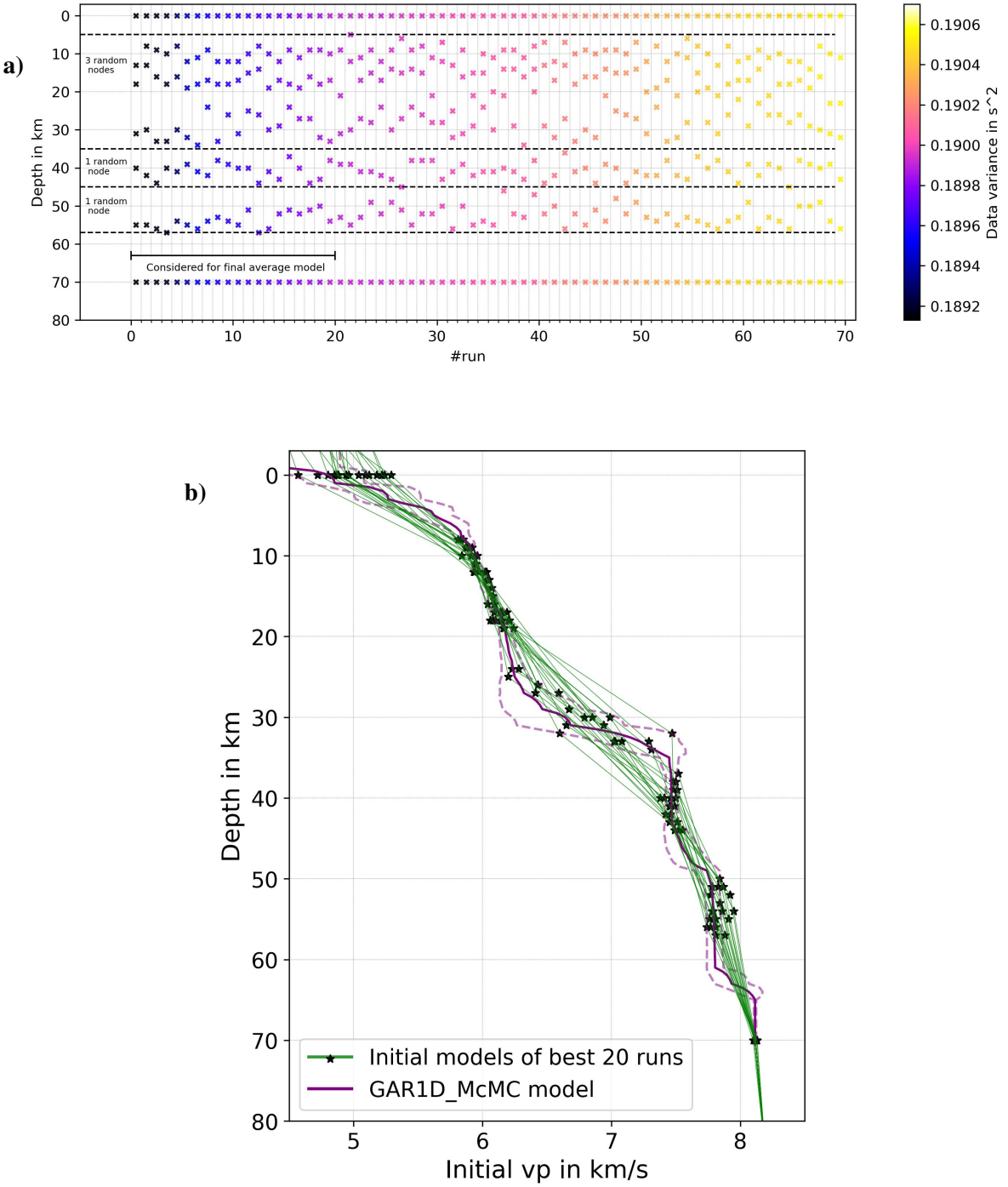

Figure 5.4.: a) Node depths of the 70 models with the lowest data variance. Based on previous tests with completely arbitrary vertical node distribution we set the boundary conditions to 3 nodes between 5 - 35 km, 1 node between 35 - 45 km and 1 node between 45 - 57 km. The final model is calculated by the unweighted average of the best 20 models. b) Starting 1D v_p distribution (green lines) and node depths (black stars) for the 20 best 3D models. Initial v_p values are taken from the *GAR1D_McMC* model (purple) from Braszus et al. (2024) and perturbed with its standard error (purple dashed).

5.4. Model resolution

Similar to most tomographic studies, our model can be described as mixed-determined meaning it is a composite of overdetermined and underdetermined regions. Therefore, it is essential to assess the resolution of the entire model space in order to ascertain in which areas the results can be interpreted confidently and which regions might be poorly resolved and possibly contain smearing effects or artefacts. There are a number of parameters that are commonly used to quantify the resolution such as the derivative weighted sum, hit count, resolution diagonal elements, and spread function (Toomey and Foulger, 1989; Eberhart-Phillips, 1990; Diehl et al., 2009a)
Another way to determine the resolution within certain regions of the model space are reconstruction tests. Travel times are calculated through a synthetic model and are then inverted using the same starting model as for the real data inversion. In order to simulate the effect of picking uncertainty, a noise term with the amplitude of the estimated picking error can be added to the synthetic travel times. The shape of the synthetic model can range from an equally spaced checkerboard over random complex structures to anomalies of expected size and amplitude.
The following summarizes the analysis we carried out to assess to resolution of our final velocity model. All tests are run as a joint inversion of picks from all distances with 5 iterations using a slightly decreased damping of $\lambda_p = 3000$; $\lambda_{ps} = 3000$. We choose a reference layering of 0, 10, 18, 28, 40, 55 and 70 km representing the average node depths of the individual runs contributing to the final model.

5.4.1. Spread function

The spread function value is calculated for each node and quantifies the spread of values around the diagonal matrix elements along each row of the model resolution matrix (MRM) (Toomey and Foulger, 1989) Nodes with low spread values are therefore better constrained than nodes with higher spread. Figures B.7 & B.8 show depth slices of spread function values for *vp* and *vp/vs*, respectively. At shallow depths areas of low spread are clearly correlating with the regions of increased seismicity in the Southwestern Alps and Northern Apennines and the area of dense station spacing with the SWATH-D network (Fig. 5.1). The Western Po plain is showing rather large spread values in the upper 20 km due to its sparse seismicity. With increasing depth the resolution of the model space becomes more homogeneous as the number of criss-crossing and horizontally propagating rays is increasing. As aspired, this yields a fairly uniform distribution of spread values at depths of 25-70 km for *vp* as well as *vp/vs*.

5.4.2. Checkerboard tests

Checkerboard tests are a widely used tool to assess the solution quality of seismic tomography images (Fukao et al., 1992; van der Hilst et al., 1993; Diehl et al., 2009a). They are helpful to investigate areas of potential smearing and quantify to what extend the amplitude of an anomaly can be recovered. Additionally, we use them to derive the finest model parametrization which still yields a robust reconstruction

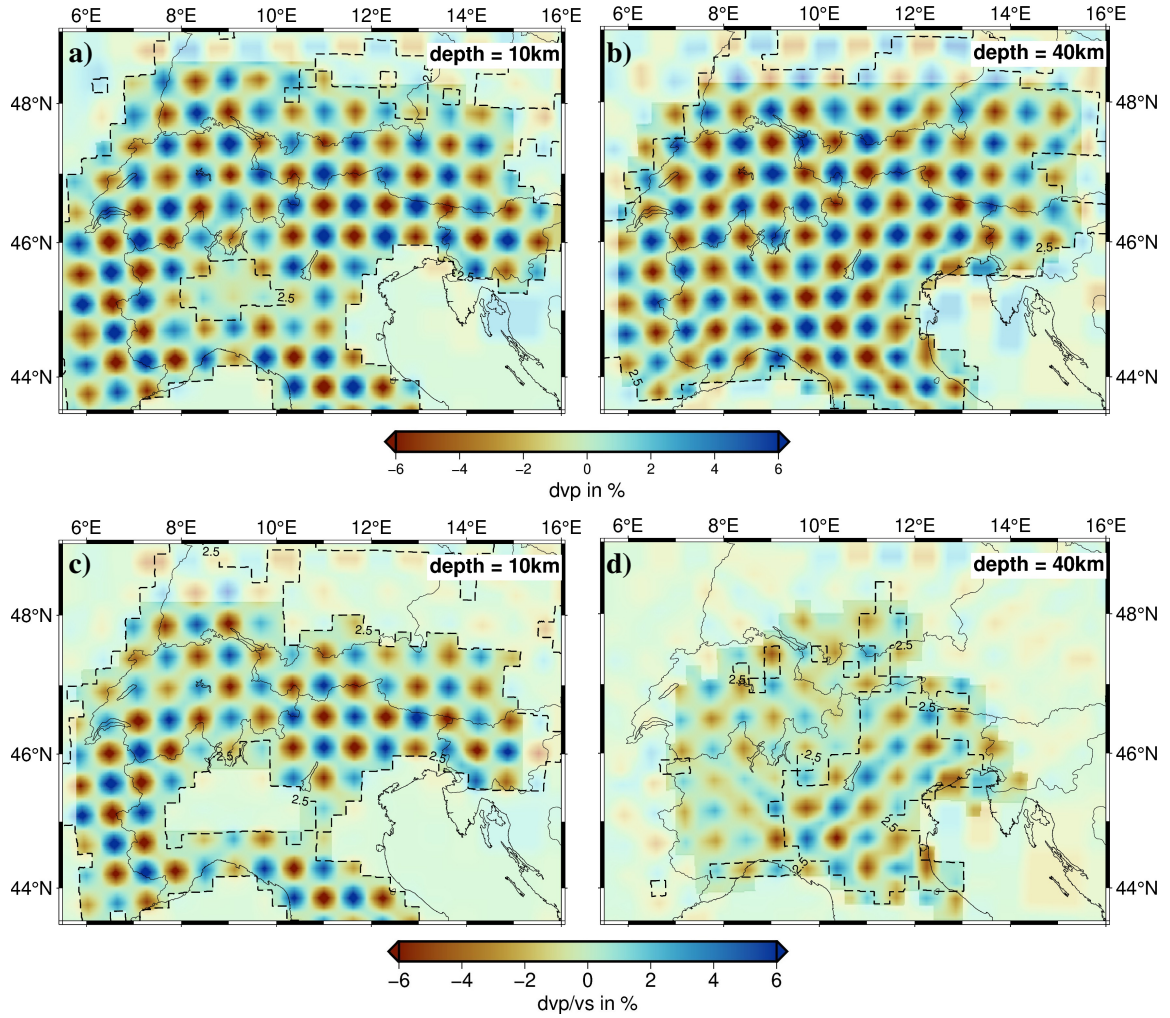

Figure 5.5.: Recovery of *vp* and *vp/vs* checkerboard anomalies of ±10% and contour lines of spread values for selected depths. Based on a combination of checkerboard reconstruction and spread value we define the well resolved models parts and blur areas of poor resolution.

of synthetic anomalies. In our case this is a horizontal node spacing of 25 km and a vertical spacing of 10 - 15 km. To account for the estimated picking error (section 5.3.3 & Braszus et al. (2024)), we add a normally distributed noise term with $\sigma = 0.25$ s to the synthetic *P*- and *S*-phase travel times.

In the synthetic checkerboard models every second layer is perturbed with alternating anomalies of ±10% in either *vp* or *vp/vs* with every other layer remaining unperturbed. The reconstructed models with *vp* and *vp/vs* perturbations in even and odd numbered layers, respectively, are shown in Figures B.9-B.12.

Figure 5.5 shows the recovered checkerboard models together with contour lines of a spread function value of 2.5. Based on a combination of checkerboard test and spread function value we define the part of the model space which is resolved well enough to be interpreted. The poorly resolved areas are blurred.

5.4.3. Characteristic model

The strength of checkerboard tests is the identification of generally well resolved areas in the model space. In order to assess to which extend an anomaly with a certain shape and amplitude can be resolved, more realistic synthetic models should be used for reconstruction tests (Haslinger et al., 1999). Therefore, we perform another recovery test with a normally distributed noise of $\sigma = 0.25$ s and mostly arbitrarily chosen anomalies in every second layer. Additionally, we insert a π-shaped low velocity anomaly beneath the Central Alps which is encircling a small rectangle of 6 nodes with increased velocity just east of the Giudicarie line. These structures are resembling main features of our final inversion. A comprehensive comparison of initial and reconstructed model is shown in Figures B.13 and B.14 while Figure 5.6 shows the depth slices at 28 km and 55 km.

Anomalies of *vp* (Fig. 5.6a,b) in the centre of the model space are mostly recovered very well in shape except for the most shallow layer at 0km depth (Fig. B.13). In well resolved areas synthetic amplitudes of $\pm 10\%$ are recovered as 4-7%, which corresponds to about half their initial amplitude. The π-shaped low velocities and the high velocity rectangle are recovered accurately in shape with an amplitude of 4-6%.

Reconstructed *vp/vs* anomalies are reduced to 20-30% of their initial amplitude at 28 km depth (Fig. 5.6). At 55 km depth (Fig. 5.6d) the reconstructed amplitude reaches 40-60% with moderate horizontal smearing.

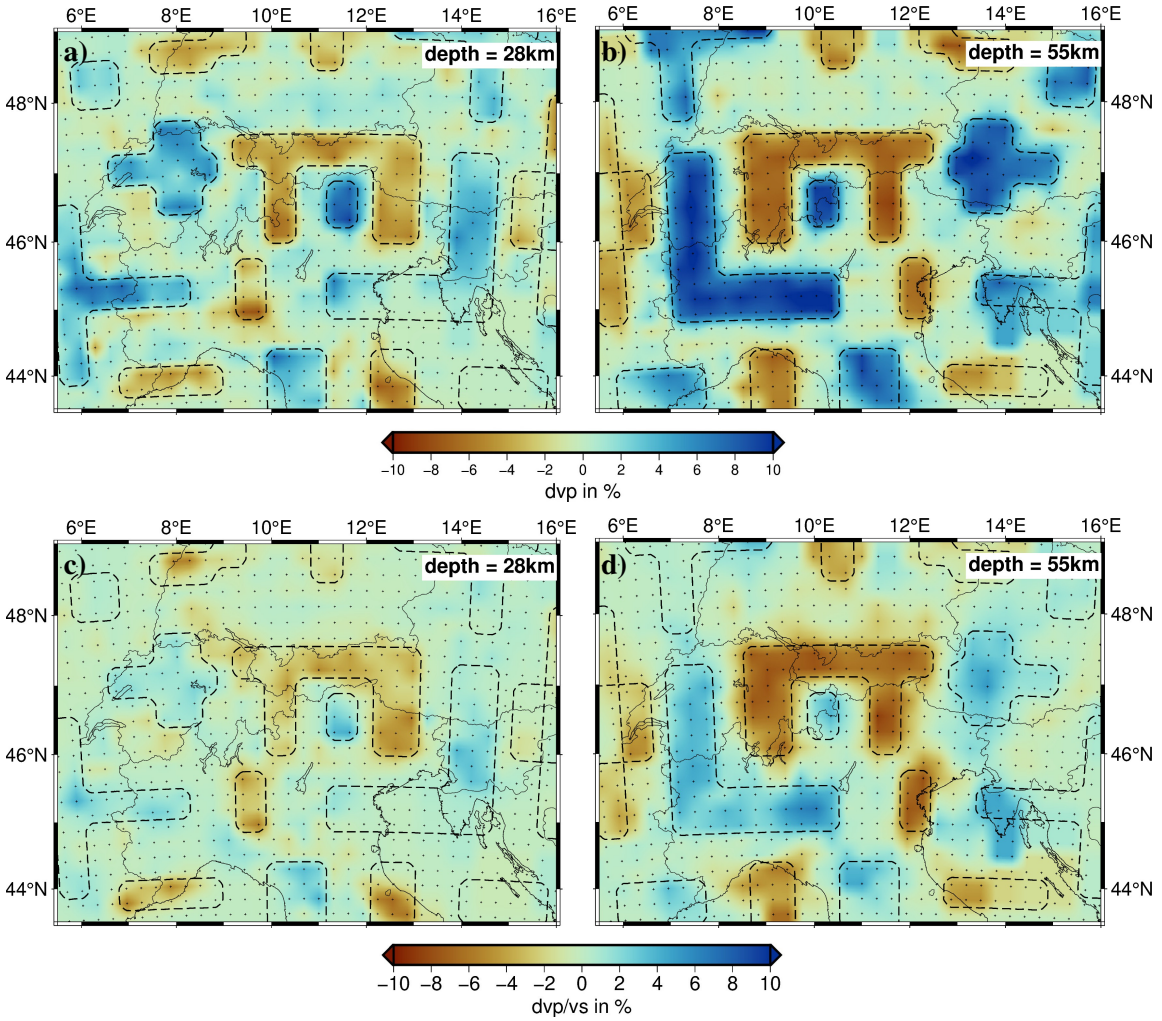

Figure 5.6.: Reconstruction of characteristic models for v_p and v_p/v_s at 28 km and 55 km depth. Outlines of the $\pm 10\%$ perturbations in the synthetic models are marked by dashed lines.

5.5. Results

In this chapter we summarize the most prominent features within the resolved models parts on the basis of depth slices and cross sections through our final velocity model.

5.5.1. Depth slices

Figure 5.7 shows horizontal slices through the final *vp*, *vp/vs* & *vs* model at 6 km, 26 km, 34 km and 44 km, respectively.

At shallow depths the Alpine orogen generally is showing a slightly increased *vp* (Fig. 5.7a) and a coherently decreased *vp/vs* ratio (Fig. 5.7c) resulting in a substantial increase in *vs* (Fig. 5.7e). A prominent low velocity zone is present for *vp* and *vs* in the Po basin in the southern foreland (anomaly A). Similarly, in the northern and western foreland a low *vp* and *vs* anomaly is extending along the Molasse basin (anomaly B). While the southern foreland shows a rather consistent increase in *vp/vs* (anomaly A), in the northern foreland an increased *vp/vs* is only present in its northeastern part (anomaly B). Another area of strongly increased *vp/vs* is present in the Friaul region in northeastern Italy and western Slovenia (anomaly C).

Throughout the mid and lower crust a well-defined WNW-ESE trending zone of low velocities is present beneath the northern Apennine (anomaly D). Due to the increased *vp/vs*, the negative anomaly in v_s is more pronounced than in v_p. This feature is becoming thinner with depths and is visible down to 50 - 55 km. In the western Po plain a very strong and sharply delineated positive anomaly is visible in *vp* and *vs* in the region where previous studies found the Ivrea Geophysical body (anomaly E). This feature is strongest at 20 - 30km (Figs. 5.7b,f) where it is showing mantle velocities already without a noticeable *vp/vs* signature. South of the Central Alps a W-E elongated positive anomaly in *vp* and *vs* stretches from the Lago Maggiore to the Italian-Slovenian boarder along the northern Po plain (anomaly F).

At mid and lower crustal depths the area beneath the Alpine arc is characterized by a decrease in *vp* and *vs* (anomalies G, H, K, L, M, N). Generally, there is a relatively thin band of low velocities following the Alpine arc west of ≈9.5°E (anomalies G, K, M). This low velocity area thickens towards the East until is reaches the Giudicarie Fault at ≈11°E (anomaly H, L, N). East of 12°E this anomaly is less distinct in shape and amplitude.

A region of increased *vp* and *vs* is present directly east of the Giudicarie Fault between 11 - 11.5°E at depth of 20 - 40 km (anomaly J). It is connected to the slightly elevated velocities beneath the Northern Po plain (anomaly F) and disrupts the otherwise continuous low velocities beneath the Alpine orogen.

Deeper than 20 km there is no coherent feature in the v_p/v_s model, except for the increase beneath the northern Apennine (anomaly D).

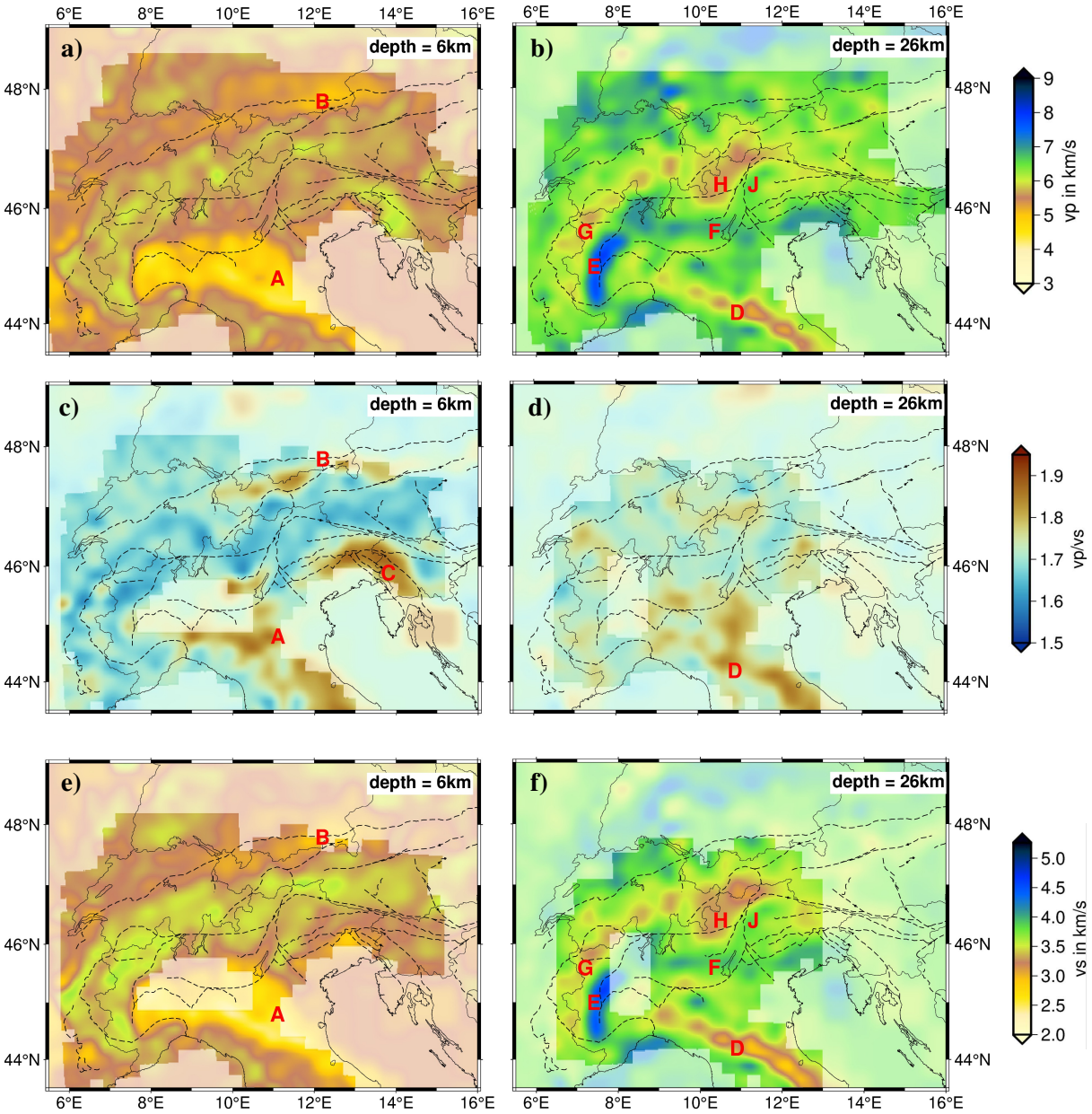

Figure 5.7.: See continuation of this Figure on the next page for description.

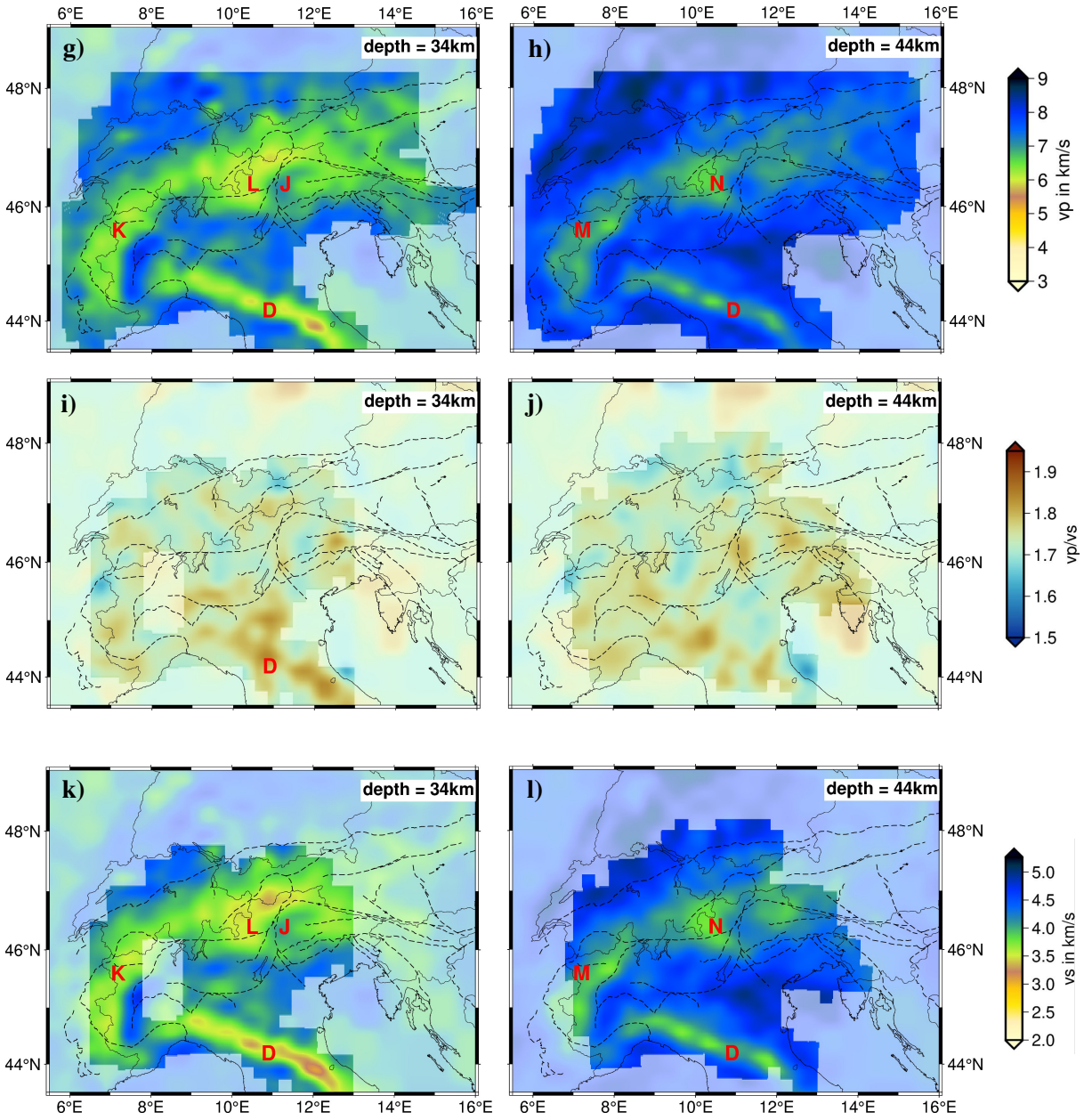

Figure 5.7.: *continued.* Horizontal slices through the final v_p, v_p/v_s and v_s model for depths of 6 km, 26 km, 34 km & 44 km, respectively. Areas of poor resolution (Fig. 5.5) are blurred. For a description of anomalies A-N we refer to the text. Major fault lines (dashed) are based on Schmid et al. (2004). The colorbar for v_p and v_s is a modified version of Diehl et al. (2009a).

5.5.2. Cross sections

Figure 5.8 shows several cross sections of *vp* cutting perpendicular through the Alpine arc including the previously investigated CIFALPS, ECORS-CROP, TRANSALP and EASI transects. Similar to earlier studies of the region (Diehl et al., 2009a; Jozi Najafabadi et al., 2022) we plot the contour line of $vp = 7.25$ km/s (black dashed) as a Moho proxy. The Moho depth from Spada et al. (2012) is indicated by dashed white lines while the seismicity within 30 km of the corresponding profile is denoted by purple dots.

All profiles display shallow low velocity zones in the western or northern (anomaly B) as well as in the southern forelands (anomaly A) corresponding to the Molasse basin and Po basin, respectively. Beneath the eastern edge of the western Alpine arc, profiles 1 and 2 reveal a positive anomaly with mantle velocities present at mid-crustal depths coinciding well with the location of the Ivrea Body (anomaly E). On the western edge of the Ivrea body our Moho proxy jumps from 50-60km depth on the European side to ≈20km on the Adriatic side in Profiles 1 & 2. From here it shallows towards the W/NW beneath the European foreland while it deepens again underneath the northwestern Po basin on the Adriatic side. All profiles display an area of decreased *vp* at depths of 15-25 km beneath the mountain chain with varying shape and amplitude (anomalies G,H & P). In profile 2 this feature is isolated from the very shallow low velocities while in profiles 1, 3 and 4 a connection to the surface is visible. Profile 5 is showing a slightly northward dipping positive anomaly (anomaly Q) in the upper 20 km beneath the Tauern window next to a similarly northward dipping low velocity anomaly South of it. Along profile 4 in the Central Alps the Moho proxy reaches ≈60km and dips considerably steeper on the Adriatic side (anomaly F) than on the European side. This difference in dip angle is leveling out towards the East in profiles 5 and 6 while the maximum Moho depth decreases to ≈45km in profile 6. The continuous shallowing of the Moho towards the East is visible in profile 7. Here, the previously identified low velocities at 15-25 km depth (anomaly H & P) are present consistently except beneath the western Tauern window (anomaly Q). They are less pronounced and slightly shallower beneath the eastern Tauern window (anomaly P) and disappear East of 14°E.

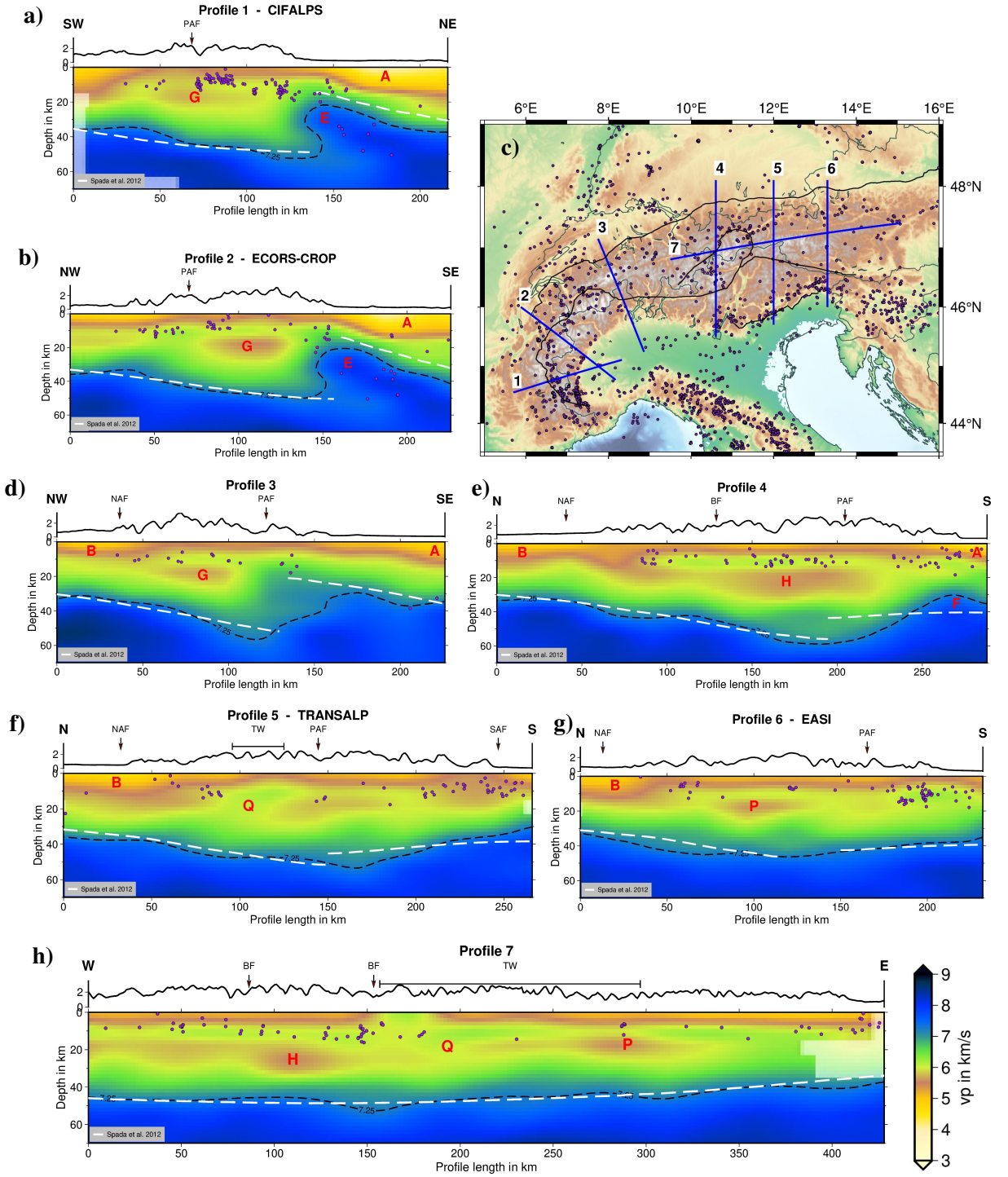

Figure 5.8.: Cross sections through the final v_p model for several arc perpendicular profiles along the entire orogen and a W-E striking profile through the Central and Eastern Alps. Purple dots mark the seismicity within 30 km of the profile. Moho depths from Spada et al. (2012) and our Moho proxy of the $v_p = 7.25$ km/s isoline are shown as white and black dashed lines, respectively. Labels along the profile mark the intersection with major fault lines (Schmid et al., 2004): PAF - Periadriatic fault; NAF - Northern Alpine Front; BF - Brenner Fault; SAF - Southern Alpine Front; TW - Tauern Window.

5.6. Discussion

CIFALPS & ECORS-CROP

Based on seismic data from the CIFALPS experiment (Zhao et al., 2016b) the western Alps have recently been studied with a variety of geophysical methods. One of the key findings is seismic evidence of European continental crust subducted into the Adriatic upper mantle along a serpentinized plate interface (Zhao et al., 2015, 2020). In Figure 5.9 we show our *vp* model along the CIFALPS transect overlain by line drawings separating crustal units based on Malusà et al. (2021) (their Fig. 13a). Their model is in good agreement with our Moho proxy and the presence of lower crustal velocities in depths of up to 55 km beneath the Ivrea body. At the westernmost tip of the Ivrea body the transition from mantle to crustal velocities matches the location of a serpentinized mantle wedge as proposed by Malusà et al. (2021). Our European Moho is consistent with Spada et al. (2012) and Malusà et al. (2021) while we image a 5-10 km deeper Moho on the Adriatic side.

In Figure 5.10 we compare our v_p model along the NW-SE striking ECORS-CROP profile in the Western Alps to the Moho from Spada et al. (2012), outlines of crustal units from Schmid et al. (2017) and seismic reflectors from Thouvenot et al. (1996). Deep crustal velocities beneath the arc and the oversteepened positive anomaly attributed to the Ivrea body are in agreement with Schmid et al. (2017). At shallow depths the reflectivity coincides well with the strong velocity gradients at the bottom of the foreland basins at ≈ 5 km beneath the Molasse basin and ≈ 10 km beneath the Po basin. Low velocities at 15 - 25 km depth southeast of the PAF are correlating well with an area of increased reflectivity. Similar to the CIFALPS profile, based on the tectonic model this mid crustal area of low velocities is located in the eastern part of the European upper crust.

Mid-crustal low velocities in Western and Central alps

Consistently decreased velocities in the mid-crust are clearly visible in the depth sections (Fig. 5.7b,f; anomalies G & H) and in all cross sections (Fig. 5.8). This feature is narrower in the western arc with $\approx$50 km width (Fig. 5.7, anomaly G) and broadens laterally to more than 100 km in the Central Alps (Fig. 5.7, anomaly H). Our reconstruction tests (Fig. 5.6a) show the resolvability of such features for v_p at mid crustal depths. Diehl et al. (2009a) likewise observe a prominent low velocity zone (LVZ) at 30 km depth (their Fig. 9) beneath the Western and Central Alps which they attribute to the Alpine crustal root. Due to the increased number of arrival times, we are able to parametrize the model with an additional crustal layer compared to Diehl et al. (2009a). With this refined vertical resolution we demonstrate that these mid-crustal low velocities are mostly separated from the surface by a band of $v_p > 6.0$ km/s (Fig. 5.8). Similar to our anomaly H in Figure 5.7 west of the Giudicarie line, Kästle et al. (2024) find a prominent LVZ in their v_s model of the Eastern Alps. The smaller scale LET of the Eastern and Eastern Southern Alps from Jozi Najafabadi et al. (2022) images low velocities at 15 - 20 km depth beneath a shallower

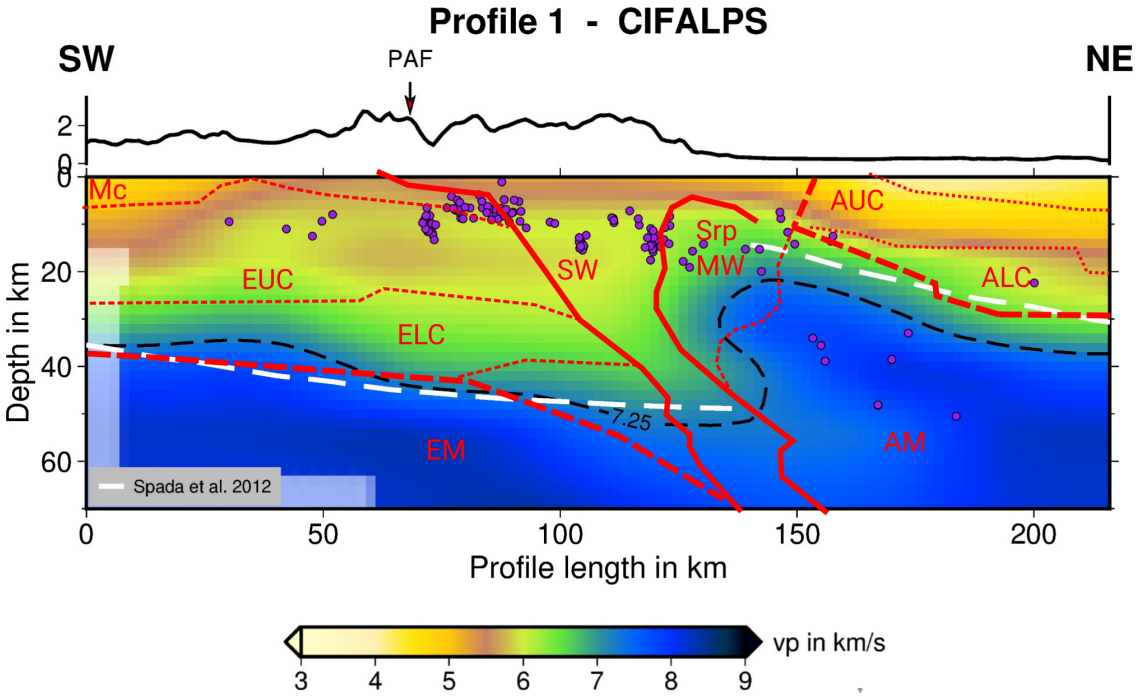

Figure 5.9.: Cross section through our v_p model along the *CIFALPS* transect (Profile 1 in Fig. 5.8) superimposed with crustal tectonic units (red lines) after Malusà et al. (2021). Moho depths from Spada et al. (2012) and our Moho proxy of the $v_p = 7.25$ km/s isoline are shown as white and black dashed lines, respectively. Events within 30 km of the profile are marked by purple dots. Mc - Mesozoic cover; EUC - European upper crust; ELC - European lower crust; EM - European mantle; AUC - Adriatic upper crust; ALC - Adriatic lower crust; AM - Adriatic mantle; SW - subduction wedge; Srp MW - Serpentinized mantle wedge; PAF - Periadriatic Fault.

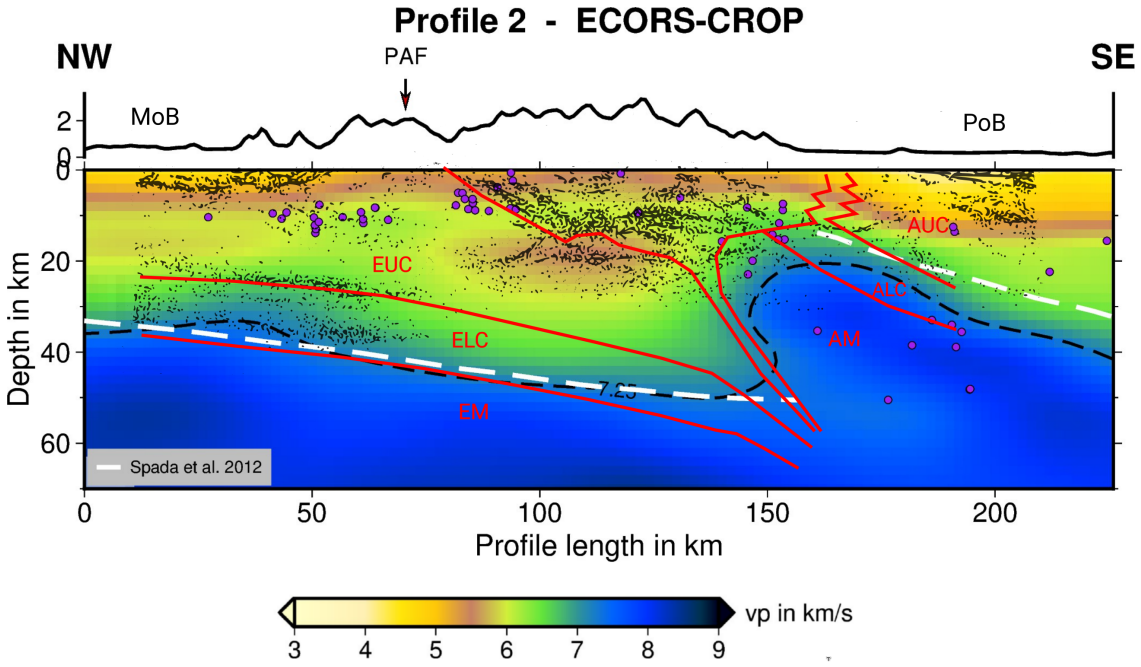

Figure 5.10.: Cross section through our v_p model along the *ECORS-CROP* transect (Profile 2 in Fig. 5.8) superimposed with crustal tectonic units (red lines) after Schmid et al. (2017) and seismic reflectors (black drawings) from Thouvenot et al. (1996). Moho depths from Spada et al. (2012) and our Moho proxy of the $v_p = 7.25$ km/s isoline are shown as white and black dashed lines, respectively. Events within 30 km of the profile are marked by purple dots. MoB - Molasse basin; PoB - Po basin; EUC - European upper crust; ELC - European lower crust; EM - European mantle; AUC - Adriatic upper crust; ALC - Adriatic lower crust; AM - Adriatic mantle; PAF - Periadriatic Fault..

high velocity area along the Tauern Window (TW) (their Fig. 9e) which is in agreement with our Profile 7 (Fig. 5.8). Here, in our model the LVZ is slightly shallower beneath the eastern TW and terminates between 13.5 - 14.0°E.

Figure 5.11 visualizes this LVZ in 3D by plotting the $v_p = 5.9$ km/s iso-velocity surface approximating the transition from upper to mid crustal velocities based on the *GAR1D_McMC* model (Fig. 5.4b). Figure 5.11a) reveals a southward dipping surface beneath the Molasse basin in the northern foreland and an upward jump of the iso-surface to ≈5 km South of the Northern Alpine Front which coincides with a band of WSW-ENE oriented shallow seismicity. Figure 5.11b) is looking at the same iso-velocity surface from the lower northwestern corner of the model. It illustrates the thinner LVZ along the western arc and its thickening beneath the Central Alps. The LVZ is partly connected to shallow low velocities on the European side in the Northwest and North and disconnected to the South and Southeast. Thus, we attribute this LVZ to former European upper crust which has been emplaced at 15 - 25 km depth as a consequence of crustal stacking during continental collision. While the thinner low velocity belt in the Western Alps is in agreement with smaller amounts of collisional shortening (Malusà et al., 2015), Miocene counterclockwise rotation of the Adriatic plate (Handy et al., 2010) likely expedited stacking West of the Giudicarie line in the Central Alps. Furthermore, this interpretation matches tectonic outlines along the CIFALPS and ECORS-CROP profiles (Figs. 5.9 & 5.10) which assign this LVZ to the European upper crustal domain.

The LVZ terminates abruptly at the Giudicarie line in the Eastern Central Alps as illustrated by the 1D v_p profiles in Figure 5.12. Further to the East it is strongly reduced and slightly shallower (Fig. 5.8h & 5.11b) indicating only minor crustal stacking. The regions of major crustal stacking in the Western and Central arc are showing the deepest crustal root based on our Moho proxy velocity (Fig. 5.13) which is in agreement with previous studies (Spada et al., 2012; Kästle et al., 2018).

Moho and Adriatic indenter

As stated above, we define our Moho proxy as the depth of the $v_p = 7.25$ km/s iso-velocity surface as displayed in Figure 5.13. First order features such as the shallow Moho of 15 - 20 km depth beneath the Ivrea zone and a deep crustal root of up to 60 km depth in the Western and Central Alps and in the Northern Apennines are in good agreement with previous studies of the region (Spada et al., 2012; Lu et al., 2020; Kästle et al., 2024). Beneath the Lepontine Dome in the Western Central Alps between 8.5 - 9.5°E the maximum Moho depths is slightly shallower with ≈45 km. This feature is similarly present in Lu et al. (2020) while only slightly indicated in Spada et al. (2012).

Another anomaly within the generally deepened Moho proxy beneath the arc is visible East of the Giudicarie line where we image Moho depths of 35 - 40 km at the approximate location of the Adriatic indenter (Ratschbacher et al., 1991; Pomella et al., 2012). In the same area we observe a prominent high velocity zone between 20 - 40 km depth (Fig.5.7, anomaly J) with a strong negative lateral velocity contrast to the West due to the previously discussed emplacement of upper crust. This contrast is following the Giu-

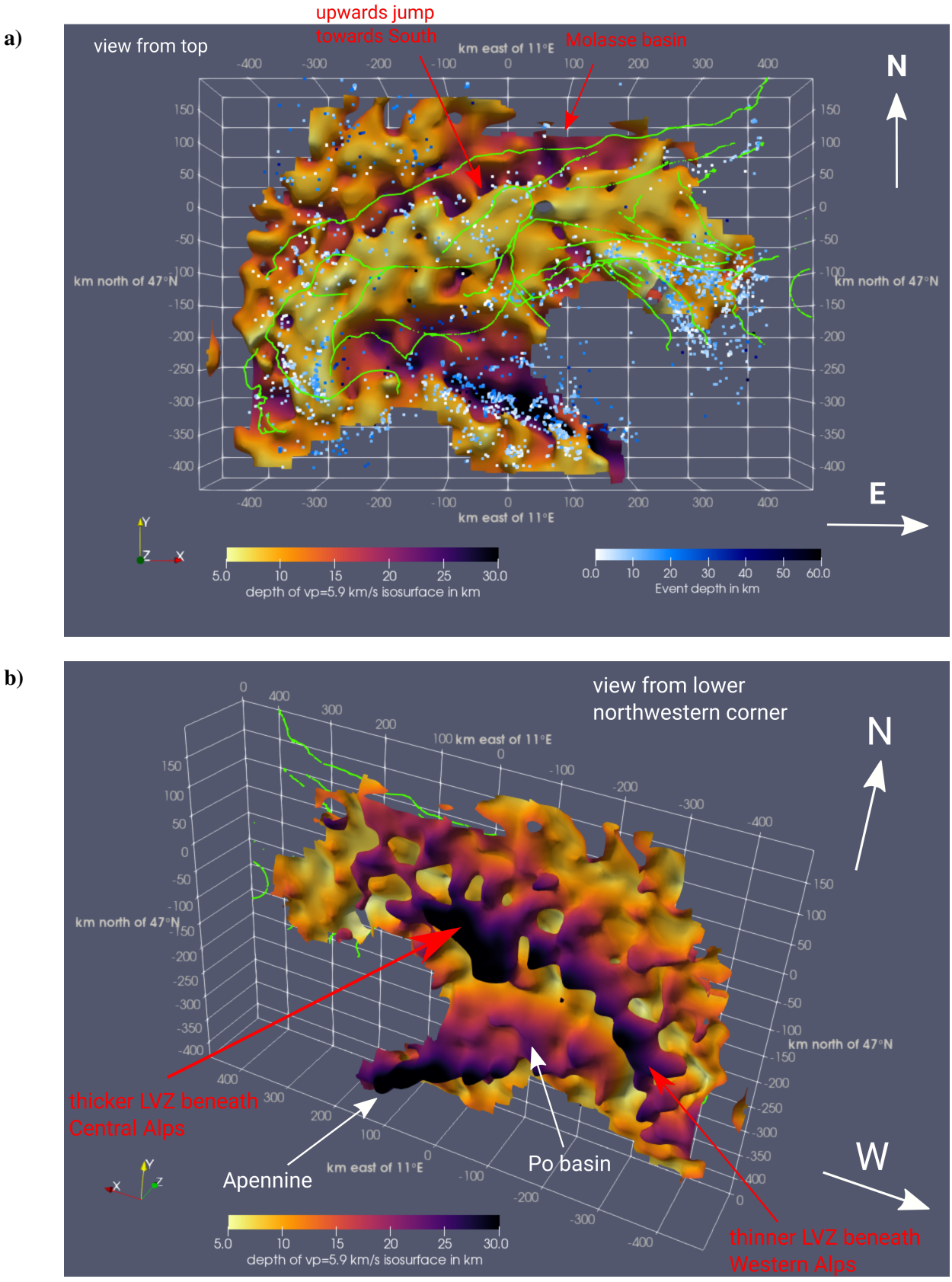

Figure 5.11.: Visualization of the $v_p = 5.9$ km/s iso-velocity surface as an approximation for the transition from upper to midle crust using *ParaView* (Ahrens et al., 2005) with viewing angles from the top (**a**) and the lower northwestern corner of the model space (**b**). Fault lines (green) are based on Schmid et al. (2004).

dicarie line very closely and is strongest between 15 - 40 km depth as the 1D velocity profiles in Figure 5.12 illustrate. Our reconstruction tests (Fig. 5.6a) verify that a feature of the given amplitude and shape is clearly resolved in the v_p model.

Albeit in less detail, this increased velocity of the Adriatic indenter and an elevated Moho have been imaged by previous works. We note that receiver function and controlled source seismic studies (Spada et al., 2012; Mroczek and Tilmann, 2021; Michailos et al., 2023) which are sensitive to sharp velocity contrasts along interfaces do not image an elevated Moho at the location of the Adriatic indenter. Methods such as LET, ambient noise tomography and wave equation tomography which rely on proxy velocities to infer Moho depths mostly show a shallower Moho and increased velocity east of the Giudicarie line. Lu et al. (2020); Sadeghi-Bagherabadi et al. (2021); Jozi Najafabadi et al. (2022) attributed this to remnants of Permian magmatism (Schuster and Stüwe, 2008). Alternatively, Kästle et al. (2024) speculated about underthrust crustal slivers that are being dragged by laterally discontinuous segments of the sinking Alpine slab or crustal deformation resulting from the collision with Adria.

The gradient of the 1D v_p profiles through the southern indenter is very similar to the northern Adriatic plate (Fig. 5.12). Thus, we interpret the southern part of the indenter to be a largely undeformed continuation of the northern Adriatic plate. Lower velocities of the southern indenter likely are a consequence of downward bending of the Adriatic plate towards the North which also explains its slightly deeper Moho at 35 - 40 km compared to the 'original' Adriatic continental Moho at ≈30 km. Similar to other studies, we image an apparent Moho elevation compared to the region west of the Giudicarie line with a Moho jump of 15 - 20 km. In comparison to the southern indenter, its northern part shows a rather continuous velocity gradient with depth (Fig. 5.12), strongly decreased velocities in the lower crust and a deeper Moho (Fig. 5.13). We interpret this as thickening in the lower crust and deformation as a result of continental collision and potential remains of Permian magmatism.

Along the northern margin of the Adriatic plate we image Moho depths of 30 - 35 km which is 5 - 10 km shallower compared to results from Spada et al. (2012). Furthermore, in the Eastern Alps we observe a consistent shallowing of the Moho towards the East which is in accordance with previous studies as the comparison of our Moho proxy with Spada et al. (2012) in Figure 5.8h shows. Combined with the less pronounced mid crustal low velocity anomalies (Fig. 5.7b,f & 5.12) we infer that only minor stacking of European and Adriatic crust took place in the Eastern Alps. Instead, crustal material extruded eastward towards the Pannonian basin (Ratschbacher et al., 1991; Frisch et al., 1998).

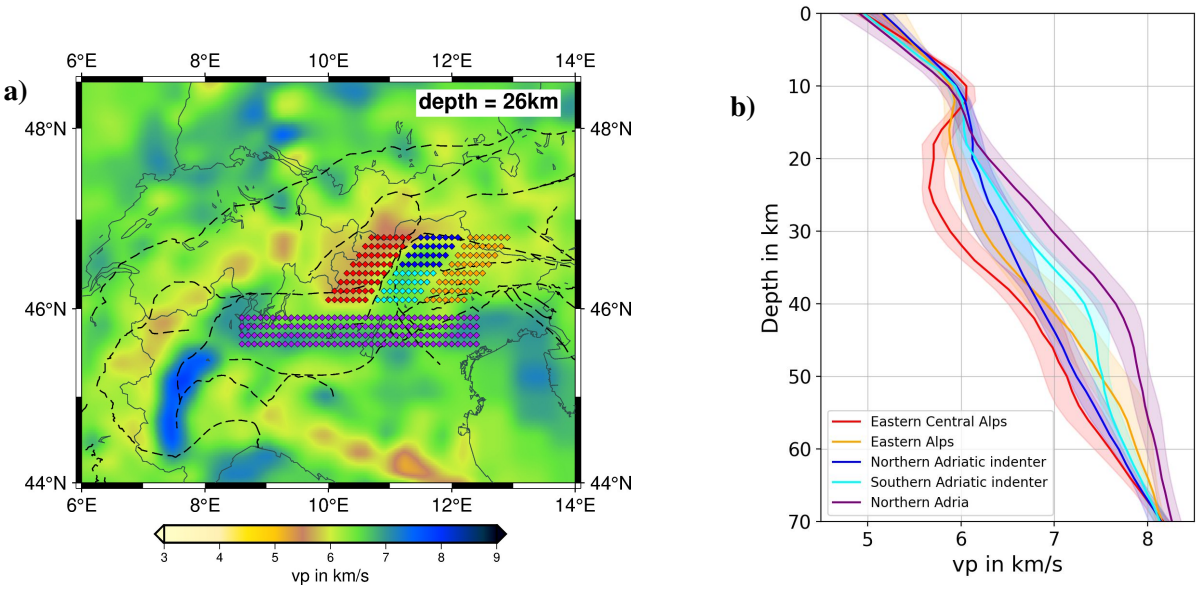

Figure 5.12.: **a)** Location of 1D v_p profiles for several regions in the Central and Eastern Alps indicated by colored diamonds plotted on top of the v_p model at 26 km. **b)** 1D v_p distribution over depth for the regions in a). Solid lines and shaded areas mark the average and standard deviation of v_p over depth.

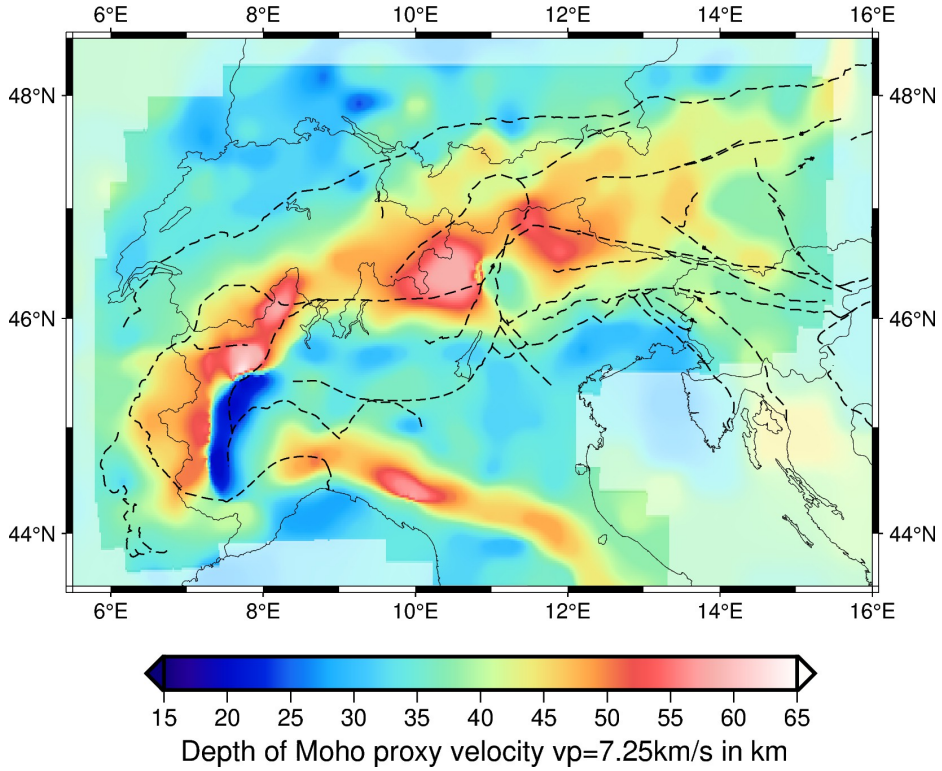

Figure 5.13.: Similar to other LET studies of the area we chose the depth of the $v_p = 7.25$ km/s iso-surface as a Moho proxy. Poorly resolved areas are blurred based on the model resolution at the average Moho depth of ~40 km. Fault lines are based on (Schmid et al., 2004).

5.7. Conclusion

We present the first comprehensive 3D *P*- and *S*-wave velocity model for the Greater Alpine region based on Local Earthquake tomography. Using waveforms from 989 seismic broad-band stations of the AlpArray Seismic Network and its complementary deployments we inverted for the 3D velocity structure of the crust and uppermost mantle with 173,841 *P*- and 68,967 *S*-phase arrivals from 2553 events of $M_L \geq 1.5$. All seismic phase arrivals were determined by the deep neural network *PhaseNet*. We intensively test variable grid spacings by running 750 inversions with almost arbitrary vertical parametrization. In each run the initial model parameters and hypocentre locations are randomly perturbed within their uncertainties. The final model is calculated as the average over the 20 runs with the lowest data misfit and shows a smoother image than the individual inversions which is less dependent on a single model parametrization.

Synthetic reconstruction tests demonstrate very good resolution at mid and lower crustal depths throughout the orogen. Robustness of our model is further indicated by the agreement of first order features with previous studies across the mountain chain. We map the foreland basins as prominent low velocity zones at shallow depths and clearly image the Ivrea body as a positive velocity anomaly with Moho depths as shallow as 20 km. A belt of consistently decreased velocities is present in the Western and Central Alps between 15 - 25 km depth. It is terminated sharply by the Adriatic indenter along the Giudicarie line and is considerably less pronounced beneath the Eastern Alps. Based on their partial connection to the upper crust in the European foreland we interpret these low velocities as former European upper crust that has been stacked during collision. This low velocity zone is most prominent directly West of the Giudicarie line where Miocene counterclockwise rotation of the Adriatic plate likely further facilitated stacking as a consequence of shortening. Furthermore, this matches the observed deep crustal root beneath the Western and Central Alps with Moho depths of up to 60 km. We find a clear difference in the seismic signature of the Adriatic indenter between its northern and southern part. We interpret its southern part to be a largely undeformed continuation of the northern Adriatic plate based on their similar velocity profiles. The northern part shows a strongly thickened lower crust most likely due to deformation during indentation and potential remnants of Permian magmatism.

6. Conclusion

The main novelty of this work is the first comprehensive high resolution crustal 3D *P*- and *S*-wave velocity model of the Greater Alpine region (GAR). On the one hand it provides consistent synthetic travel times, crustal correction terms or an initial velocity model for various future seismological studies. On the other hand it directly addresses some of the initially posed research questions regarding the large scale crustal velocity structure of the GAR.
In a first step, I calculated the first comprehensive 1D *P*- and *S*-wave velocity model of the GAR which serves as an initial model for the 3D velocity inversion. The 1D and 3D models are both based on the densely spaced AlpArray Seismic Network and complementary networks installed as part of the AlpArray/4DMB project.

Assessment of AI picking algorithms and development of a new pick selection method

I used the recently published *SeisBench* toolbox (Woollam et al., 2022) to assess the performance of the most common neural network algorithms for seismic phase picking by benchmarking them against a high accuracy manual reference catalog from Diehl et al. (2009a). Based on a combination of accuracy, recall and number of additional arrivals I found *PhaseNet* (Weiqiang and Beroza, 2018) to be most suited for this study and used it for all seismic phase picking tasks. The discrepancy between *PhaseNet* and manual picks is similar to the inconsistency between two independently determined manual pick catalogs. Furthermore, I observed a clear correlation between *PhaseNet's* pick probability and the manually assigned pick quality.
In order to efficiently and consistently discard outliers from the *PhaseNet* pick catalog, I developed a data-driven pre-inversion pick selection technique. On an event basis, it selects or discards arrivals based on their proximity to two weighted regression lines fit through the *Pg/Sg* and *Pn/Sn* arrival branches of each event section plot. It requires only minor manual supervision and is applicable to distances up to 1000 km including the crustal triplication zone.

Minimum 1D velocity model of the Greater Alpine region

I simultaneously inverted for hypocentral parameters and the 1D *P*- and *S*-wave velocity structure of the GAR including stations corrections. This inversion is based on 39,599 *P* and 13,188 *S* observations from 384 events with $M_L \geq 2.5$. I illustrated how distant *Pn/Sn* observations potentially overprint the

influence of local site effects in the station correction terms. Therefore, on the one hand I computed the *AlpsLocPS* model based on arrivals with epicentral distances of $\Delta \leq 130$ km which can be used for consistent (re)location of seismicity within the GAR. On the other hand, I published the *GAR1D_PS* model based on observations from up to 1000 km capturing the velocity structure of the entire crust and uppermost mantle. It is the first comprehensive and uniformly processed 1D *P*- and *S*-wave velocity model of the entire GAR and will allow the computation of consistent synthetic travel times.
I compared the well established *VELEST* code against the recently developed bayesian Markov chain Monte Carlo (McMC) algorithm. Both approaches yield very similar results regarding the model velocities, station corrections and hypocentres. While *VELEST* requires *a priori* knowledge in form of initial velocity models and event locations, *McMC* explores a manually defined model space by iteratively perturbing an arbitrarily chosen model parameter for millions of random starting models. Thus, it provides an uncertainty estimate for each model parameter corresponding to the standard deviation of each parameter across the *n* best fitting models. Based on a comparison of my final event locations with previous studies from Jozi Najafabadi et al. (2021) and Bagagli et al. (2022), I quantified the hypocentral accuracy as $\sigma_{lon/lat} \approx 1.5$ - 2.5 km in horizontal and $\sigma_{dep} \approx 6.0$ km in vertical direction when using a 1D velocity model of the GAR including station corrections.

3D *P*- and *S*-wave velocity model

Due to the substantially larger number of 12,053 independent velocity model parameters in the subsequent 3D velocity inversion, I lowered the event magnitude threshold to $M_L \geq 1.5$ which yielded 173,841 *P*- and 68,967 *S*-picks from 2553 events recorded at 989 seismic broadband stations. I used *SIMUL2023* (Eberhart-Phillips et al., 2024), the most recent version of the established *SIMULPS* algorithm, to simultaneously invert for hypocentral parameters and the 3D velocity structure of the crust and uppermost mantle. *SIMUL2023* linearizes the inversion problem around a starting model which is updated iteratively and thus requires initial velocities and hypocentral parameters. The model space is parametrized along nodal planes and linearly interpolated between neighboring nodes. Since the selection of initial model parameters and model parametrization has a significant impact on the inversion result, I computed a total of 750 inversion runs. In each run the initial event locations and velocity structure were perturbed within the uncertainty estimates I determined during computation of the 1D model. Furthermore, in each run the model parametrization was varied within a reasonable range to make the result less dependent on a single grid spacing. The final model was calculated as the average of the 20 single models with the best data fit. It shows a smoother and more reasonable velocity structure than each individual model and additionally provides statistical model and hypocentre uncertainties.
Previous studies based on smaller data sets (e.g. Diehl et al., 2009a) put a strong focus on precise manual or manually supervised onset time determination. Since this approach is not feasible for the amounts of data analyzed in this study, I use these accurate manual arrivals as a reference to assess the performance

of neural networks. My velocity model shows higher resolution over a larger area which verifies the applicability of neural network based arrival times for LET.

Summary of tectonic interpretations

The final 3D velocity model contains the most prominent geological features of the GAR such as the Molasse and Po basin in the northern and southern foreland, respectively. The strong velocity gradient at their bottoms is in good agreement with reflectivity of active seismics from (Thouvenot et al., 1996). Another well-studied large scale anomaly is the Ivrea body at the western edge of the Po plain (Schmid et al., 2017; Zhao et al., 2020). It consists of Adriatic mantle which has been oversteepened and thus intrudes into the upper crust while overriding the subducting European plate. Similar to previous studies, I image the Ivrea body as an area of strongly increased velocities with an elevated Moho reaching as shallow as 15 - 20 km. The Moho generally is deepest beneath the Western and Central Alps where it reaches depths of ≈60 km while it slowly shallows towards the East matching the results from Spada et al. (2012). The general agreement of these described first order features with previous studies indicates robustness of my model across the entire GAR.

A remarkable novel feature in my final model is a belt of consistently decreased velocities in the Western and Central Alps between 15 - 25 km depth. A 3D visualization of this low velocity zone (LVZ) reveals a partial connection to the European upper crust in the North and Northwest while it is disconnected from the Adria in the South and Southeast. I interpret this mid crustal LVZ as former European upper crust which has been emplaced beneath Adriatic upper and mid crustal material during continental collision. The implicated crustal stacking is reflected in an increased Moho depth beneath the Western and Central Alps which is in agreement with previous studies (Spada et al., 2012). The broadening of the LVZ in the Central Alps directly West of the Giudicarie line might be related to Miocene counterclockwise rotation of the Adriatic plate which further facilitated stacking as a consequence of shortening. While parts of this LVZ have been imaged by earlier tomographies (Diehl et al., 2009a; Jozi Najafabadi et al., 2022; Kästle et al., 2024), they were lacking either the resolution or the spatial extend of the model space to interpret this feature within the bigger picture of the entire Alpine mountain chain.

The eastern margin of this LVZ is clearly delineated by the Giudicarie line along which a prominent W-E striking velocity contrast is evident. An increase of velocities together with an apparent Moho elevation East of the Giudicarie line have been attributed to the Adriatic indenter and its composition of rigid remnants of permian magmatism (Lu et al., 2020; Sadeghi-Bagherabadi et al., 2021; Kästle et al., 2024). In this work I present strong indications of a different seismic signature between the northern and southern part of the Adriatic indenter. Its southern part generally follows the velocity profiles of the Adriatic plate in the South with a similar velocity gradient throughout the crust and a slightly deeper Moho of 35 - 40 km. Thus, I interpret it as a largely undeformed continuation of the Adriatic plate which has been slightly bent downwards during collision. The northern part of the Adriatic indenter shows

a considerably lower velocity gradient and Moho depths of $\geq$50 km. I interpret this as consequence of lower crustal thickening based on accumulation of European as well as Adriatic lower crust during collision and potential remnants of permian magmatism.

Acknowledgments

I would like to express my profound thanks to Prof. Andreas Rietbrock for creating this project in the first place and for supervising my work over the last years. Without his thoughtful advises, creative inputs and general geoscientific knowledge this thesis would not exist in the way is does now. He helped me understand and experience that there is hardly any task that cannot be solved or at least transformed into a solvable one by approaching it from all possible - and sometimes seemingly impossible - angles.
Secondly, I would like to thank Dr. Christian Haberland not only for co-supervising this work but also for hosting me twice during my stays in Potsdam. Thank you and your family, Christian, for your hospitality.
Furthermore, I would like to thank apl. Prof. Joachim Ritter for co-refereeing this thesis.
Looking back, I am truly grateful for all the great, enriching, sometimes exhausting but always enjoyable out-of-office experiences such as field work, conferences, project meetings and research visits that I was able to experience during my PhD.
A huge shout-out to all my fellow AlpArray/4DMB PhD students who turned every conference and project meeting into a great time and sometimes - maybe inadvertently - with their stories made me realize what a great environment I am given by the GPI and its people to pursue my PhD here. I thank all my colleagues, not only for their helpful feedback on my work, but especially for creating a great work environment.
Since my time at KIT/GPI did not start with my PhD but actually in October 2013, there are many other people whom I want to thank for creating many great memories on- and off-campus and for helping me take my mind off geophysics every now and then.
Going back even further, I obviously owe great thanks to my parents, grandparents and all family that supported me and made it possible for me to study at all.

7. Bibliography

Ahrens, J., B. Geveci, and C. Law, 2005: Visualization handbook. URL https://www.sciencedirect.com/book/9780123875822/visualization-handbook.

Aldersons, F., 2004: Toward three-dimensional crustal structure of the Dead Sea region from local earthquake tomography. Ph.D. thesis, Tel Aviv University, Israel.

Allen, R. V., 1978: Automatic earthquake recognition and timing from single traces. *Bulletin of the Seismological Society of America*, **68 (5)**, 1521–1532, URL https://doi.org/10.1785/BSSA0680051521.

AlpArray Seismic Network, 2014: Eastern Alpine Seismic Investigation (EASI) - AlpArray Complimentary Experiment. URL http://networks.seismo.ethz.ch/networks/xt/.

———, 2015: AlpArray Seismic Network (AASN) temporary component. URL http://networks.seismo.ethz.ch/networks/z3/.

Arcoraci, L., L. Miconi, D. Cheloni, L. Colini, R. Di Maro, A. Lisi, M. T. Mariucci, S. Pinzi, P. Battelli, and M. Berardi, 2020: Bollettino Sismico Italiano (BSI), I quadrimestre 2020. URL http://terremoti.ingv.it/bsi?id=10.13127/BSI/202001.

Baer, M. and U. Kradolfer, 1987: An automatic phase picker for local and teleseismic events. *Bulletin of the Seismological Society of America*, **77 (4)**, 1437–1445, URL https://doi.org/10.1785/BSSA0770041437.

Bagagli, M., I. Molinari, T. Diehl, E. Kissling, D. Giardini, and AlpArray Working Group , 2022: The AlpArray Research Seismicity-Catalogue. *Geophysical Journal International*, **231 (2)**, 921–943.

Bayer, R., M. Carozzo, R. Lanza, M. Miletto, and D. Rey, 1989: Gravity modelling along the ECORS-CROP vertical seismic reflection profile through the Western Alps. *Tectonophysics*, **162 (3)**, 203–218, URL https://www.sciencedirect.com/science/article/pii/0040195189902448.

Bianchi, I. and G. Bokelmann, 2014: Seismic signature of the alpine indentation, evidence from the eastern alps. *Journal of Geodynamics*, **82**, 69–77, URL https://www.sciencedirect.com/science/article/pii/S0264370714001033, sI : Geodynamics of the Mediterranean.

Bigi, G., A. Castellarin, M. Coli, G. Dal Piaz, R. Sartori, P. Scandone, and G. Vai, 1990: Structural model of Italy, 1:500.000. *Quaderni de La Ricerca Scientifica, C.N.R.*, **114**, 81–110.

Bousquet, R., S. Schmid, G. Zeilinger, R. Oberhänsli, C. Rosenberg, G. Molli, C. Robert, M. Wiederkehr, and P. Rossi, 2012: *Tectonic framework of the Alps*. CCGM/CGMW (Commission for the Geological Map of the World, Paris).

Braszus, B., A. Rietbrock, C. Haberland, and T. Ryberg, 2024: AI based 1-D P- and S-wave velocity models for the greater alpine region from local earthquake data. *Geophysical Journal International*, **237 (2)**, 916–930, URL `https://doi.org/10.1093/gji/ggae077`.

Carminati, E., M. Lustrino, and C. Doglioni, 2012: Geodynamic evolution of the central and western Mediterranean: Tectonics vs. igneous petrology constraints. *Tectonophysics*, **579**, 173–192, URL `https://www.sciencedirect.com/science/article/pii/S004019511200056X`, orogenic processes and structural heritage in Alpine-type mountain belts.

Dewey, J., M. Helman, S. Knott, E. Turco, and D. Hutton, 1989: Kinematics of the western Mediterranean. *Geological Society, London, Special Publications*, **45**, 265–283.

Di Stefano, R., F. Aldersons, E. Kissling, P. Baccheschi, C. Chiarabba, and D. Giardini, 2006: Automatic seismic phase picking and consistent observation error assessment: Application to the Italian seismicity. *Geophysical Journal International*, **165 (1)**, 121 – 134.

Diehl, T., S. Husen, E. Kissling, and N. Deichmann, 2009a: High-resolution 3-D P-wave model of the Alpine crust. *Geophysical Journal International*, **179 (2)**, 1133–1147.

Diehl, T., E. Kissling, M. Herwegh, and S. Schmid, 2021: Improving Absolute Hypocenter Accuracy With 3D Pg and Sg Body-Wave Inversion Procedures and Application to Earthquakes in the Central Alps Region. *Journal of Geophysical Research: Solid Earth*, **126 (12)**, e2021JB022 155.

Diehl, T., E. Kissling, S. Husen, and F. Aldersons, 2009b: Consistent phase picking for regional tomography models: application to the greater Alpine region. *Geophysical Journal International*, **176 (2)**, 542–554.

Eberhart-Phillips, D., 1986: Three-dimensional velocity structure in northern California Coast Ranges from inversion of local earthquake arrival times. *Bulletin of the Seismological Society of America*, **76 (4)**, 1025–1052.

———, 1990: Three-dimensional P and S velocity structure in the Coalinga Region, California. *Journal of Geophysical Research: Solid Earth*, **95 (B10)**, 15 343–15 363.

Eberhart-Phillips, D. and M. Reyners, 1997: Continental subduction and three-dimensional crustal structure: The northern South Island, New Zealand. *Journal of Geophysical Research: Solid Earth*, **102 (B6)**, 11 843–11 861.

Eberhart-Phillips, D., C. Thurber, A. Rietbrock, B. Fry, M. Reyners, and F. Lanza, 2021: Simul2017: a flexible program for inversion of earthquake data for 3-D velocity and hypocenters or 3-D Q. URL https://doi.org/10.5281/zenodo.5746047.

———, 2024: Simul2023: a flexible program for inversion of earthquake data for 3-D velocity and hypocenters or 3-D Q. URL https://doi.org/10.5281/zenodo.10695070.

Escudero, C., 2022: P-, S-wave velocity and VP/VS of the Colima Volcanic Complex from local earthquake tomography. *Bulletin of Volcanology*, **84**, 30.

Eva, E. and S. Solarino, 1998: Variations of stress directions in the western Alpine arc. *Geophysical Journal International*, **135 (2)**, 438 – 448.

Evans, J., D. Eberhart-Phillips, and C. Thurber, 1994: User's manual for SIMULPS12 for imaging Vp and Vp/Vs: A derivative of the Thurber tomographic inversion SIMUL3 for local earthquakes and explosions. *U.S. Geol. Surv. Open File Rep*, **94–431**.

Frisch, W., J. Kuhlemann, I. Dunkl, and A. Brügel, 1998: Palinspastic reconstruction and topographic evolution of the Eastern Alps during late Tertiary tectonic extrusion. *Tectonophysics*, **297 (1)**, 1–15, URL https://www.sciencedirect.com/science/article/pii/S0040195198001607.

Froitzheim, N., S. Schmid, and M. Frey, 1996: Mesozoic paleogeography and the timing of eclogitefacies metamorphism in the Alps: A working hypothesis. *Eclogae Geologicae Helvetiae*, **891 (1)**, 81–110.

Fukao, Y., M. Obayashi, H. Inoue, and M. Nenbai, 1992: Subducting slabs stagnant in the mantle transition zone. *Journal of Geophysical Research: Solid Earth*, **97 (B4)**, 4809–4822.

Haberland, C., A. Rietbrock, D. Lange, K. Bataille, and T. Dahm, 2009: Structure of the seismogenic zone of the southcentral Chilean margin revealed by local earthquake traveling tomography. *Journal of Geophysical Research*, **114 (B1)**, B01 317.

Handy, M., S. Schmid, R. Bousquet, E. Kissling, and D. Bernoulli, 2010: Recoiling plate-tectonic reconstructions of Alpine Tethys with the geological-geophysical record of spreading and subduction in the Alps. *Earth-Science Reviews*, **102 (3-4)**, 121–158.

Handy, M., K. Ustaszewski, and E. Kissling, 2014: Reconstructing the Alps–Carpathians–Dinarides as a key to understanding switches in subduction polarity, slab gaps and surface motion. *International Journal of Earth Sciences*, **104**, 1–26.

Handy, M. R., J. Giese, S. M. Schmid, J. Pleuger, W. Spakman, K. Onuzi, and K. Ustaszewski, 2019: Coupled Crust-Mantle Response to Slab Tearing, Bending, and Rollback Along the Dinaride-Hellenide Orogen. *Tectonics*, **38 (8)**, 2803–2828.

Handy, M. R., S. M. Schmid, M. Paffrath, W. Friederich, and the AlpArray Working Group, 2021: Orogenic lithosphere and slabs in the greater Alpine area – interpretations based on teleseismic P-wave tomography. *Solid Earth*, **12 (11)**, 2633–2669.

Haslinger, F., E. Kissling, J. Ansorge, D. Hatzfeld, E. Papadimitriou, V. Karakostas, K. Makropoulos, H.-G. Kahle, and Y. Peter, 1999: 3D crustal structure from local earthquake tomography around the Gulf of Arta (Ionian region, NW Greece). *Tectonophysics*, **304 (3)**, 201–218.

Heit, B., L. Cristiano, C. Haberland, F. Tilmann, D. Pesaresi, Y. Jia, H. Hausmann, S. Hemmleb, M. Haxter, T. Zieke, K. Jaeckl, A. Schloemer, and M. Weber, 2021: The SWATH-D Seismological Network in the Eastern Alps. *Seismological Research Letters*, **92 (3)**, 1592–1609, URL `https://doi.org/10.1785/0220200377`.

Hetényi, G., I. Molinari, J. Clinton, G. Bokelmann, I. Bondár, W. Crawford, J.-X. Dessa, C. Doubre, W. Friederich, F. Fuchs, D. Giardini, Z. Gráczer, M. Handy, M. Herak, Y. Jia, E. Kissling, H. Kopp, M. Korn, L. Margheriti, T. Meier, M. Mucciarelli, A. Paul, D. Pesaresi, C. Piromallo, T. Plenefisch, J. Plomerová, J. Ritter, G. Rümpker, V. Šipka, D. Spallarossa, C. Thomas, F. Tilmann, J. Wassermann, M. Weber, Z. Wéber, V. Wesztergom, M. Živčić, AlpArray Seismic Network Team, AlpArray OBS Cruise Crew , and AlpArray Working Group, 2018: The AlpArray Seismic Network: A Large-Scale European Experiment to Image the Alpine Orogen. *Surveys in Geophysics*, **39**, 1009–1033.

Hicks, S., A. Rietbrock, I. Ryder, C.-S. Lee, and M. Miller, 2014: Anatomy of a megathrust: The 2010 M8.8 Maule, Chile earthquake rupture zone imaged using seismic tomography. *Earth and Planetary Science Letters*, **405**, 142–155.

Hofman, L. J., J. Kummerow, S. Cesca, and the AlpArray-Swath-D Working Group, 2023: A new seismicity catalogue of the eastern Alps using the temporary Swath-D network. *Solid Earth*, **14 (10)**, 1053–1066.

Horvath, F., G. Bada, P. Szafián, G. Tari, A. Ádám, and S. Cloetingh, 2006: Formation and deformation of the Pannonian Basin: Constraints from observational data. *Geological Society, London, Memoirs*, **32**, 191–206.

Husen, S., E. Kissling, E. Flueh, and G. Asch, 1999: Accurate hypocentre determination in the seismogenic zone of the subducting Nazca Plate in northern Chile using a combined on-/offshore network. *Geophysical Journal International*, **138 (3)**, 687–701.

Jozi Najafabadi, A., C. Haberland, E. Le Breton, M. Handy, V. Verwater, B. Heit, M. Weber, and the AlpArray and AlpArray SWATH-D working groups, 2022: Constraints on Crustal Structure in the Vicinity of the Adriatic Indenter (European Alps) From Vp and Vp / Vs Local Earthquake Tomography. *Journal of Geophysical Research: Solid Earth*, **127 (2)**, e2021JB023 160.

Jozi Najafabadi, A., C. Haberland, T. Ryberg, V. Verwater, E. Le Breton, M. Handy, M. Weber, and the AlpArray and AlpArray SWATH-D working groups, 2021: Relocation of earthquakes in the southern and eastern Alps (Austria, Italy) recorded by the dense, temporary SWATH-D network using a Markov chain Monte Carlo inversion. *Solid Earth*, **12 (5)**, 1087–1109.

Julian, B. and D. Gubbins, 1977: Three-dimensional seismic ray tracing. *Journal of Geophysics*, **43 (1)**, 95–113.

Kissling, E., 1993: Deep structure of the Alps—what do we really know? *Physics of the Earth and Planetary Interiors*, **79 (1)**, 87–112.

Kissling, E., W. Ellsworth, D. Eberhart-Phillips, and U. Kradolfer, 1994: Initial reference models in local earthquake tomography. *Journal of Geophysical Research: Solid Earth*, **99 (B10)**, 19 635–19 646.

Krischer, L., T. Megies, R. Barsch, M. Beyreuther, T. Lecocq, C. Caudron, and J. Wassermann, 2015: ObsPy: A bridge for seismology into the scientific Python ecosystem. *Computational Science & Discovery*, **8 (1)**, 014 003.

Kuang, W., C. Yuan, and J. Zhang, 2021: Real-time determination of earthquake focal mechanism via deep learning. *Nature Communications*, **12**, 1432.

Kästle, E., A. El-Sharkawy, L. Boschi, T. Meier, C. Rosenberg, N. Bellahsen, L. Cristiano, and C. Weidle, 2018: Surface Wave Tomography of the Alps Using Ambient-Noise and Earthquake Phase Velocity Measurements. *Journal of Geophysical Research: Solid Earth*, **123 (2)**, 1770–1792.

Kästle, E. D., F. Tilmann, and AlpArray and Swath-D Working Groups , 2024: Anisotropic Reversible-Jump McMC Shear-Velocity Tomography of the Eastern Alpine Crust. *Geochemistry, Geophysics, Geosystems*, **25 (3)**, e2023GC011 238.

Lapins, S., B. Goitom, J. Kendall, M. Werner, K. Cashman, and J. Hammond, 2021: A little data goes a long way: Automating seismic phase arrival picking at nabro volcano with transfer learning. *Journal of Geophysical Research: Solid Earth*, **126 (7)**, e2021JB021 910.

Lay, T. and T. C. Wallace, 1995: Modern Global Seimology. *Modern Global Seismology*, Lay, T. and T. C. Wallace, Eds., Academic Press, International Geophysics, Vol. 58, URL `https://www.sciencedirect.com/science/article/pii/S0074614205800026`.

León-Ríos, S., L. Bie, H. Agurto-Detzel, A. Rietbrock, A. Galve, A. Alvarado, S. Beck, P. Charvis, Y. Font, S. Hidalgo, M. Hoskins, M. Laigle, D. Oregioni, A. Meltzer, M. Ruiz, and J. Woollam, 2021: 3D Local Earthquake Tomography of the Ecuadorian Margin in the Source Area of the 2016 Mw 7.8 Pedernales Earthquake. *Journal of Geophysical Research: Solid Earth*, **126 (3)**, e2020JB020 701.

Lomax, A., J. Virieux, P. Volant, and C. Berge-Thierry, 2000: Probabilistic Earthquake Location in 3D and Layered Models . *Advances in Seismic Event Location*, Thurber, C. H. and N. Rabinowitz, Eds., Springer Netherlands, Dordrecht, 101–134, URL https://doi.org/10.1007/978-94-015-9536-0_5.

Lu, Y., L. Stehly, R. Brossier, and A. Paul, 2020: Imaging Alpine crust using ambient noise wave-equation tomography. *Geophysical Journal International*, **222 (1)**, 69–85.

Malusà, M. G., C. Faccenna, S. L. Baldwin, P. G. Fitzgerald, F. Rossetti, M. L. Balestrieri, M. Danišík, A. Ellero, G. Ottria, and C. Piromallo, 2015: Contrasting styles of (U)HP rock exhumation along the Cenozoic Adria-Europe plate boundary (Western Alps, Calabria, Corsica). *Geochemistry, Geophysics, Geosystems*, **16 (6)**, 1786–1824.

Malusà, M. G., S. Guillot, L. Zhao, A. Paul, S. Solarino, T. Dumont, S. Schwartz, C. Aubert, P. Baccheschi, E. Eva, Y. Lu, C. Lyu, S. Pondrelli, S. Salimbeni, W. Sun, and H. Yuan, 2021: The Deep Structure of the Alps Based on the CIFALPS Seismic Experiment: A Synthesis. *Geochemistry, Geophysics, Geosystems*, **22 (3)**, e2020GC009 466.

Menke, W., 1989: *Geophysical Data Analysis : Discrete Inverse Theory.*, Vol. Second edition. Academic Press.

Michailos, K., G. Hetényi, M. Scarponi, J. Stipčević, I. Bianchi, L. Bonatto, W. Czuba, M. Di Bona, A. Govoni, K. Hannemann, T. Janik, D. Kalmár, R. Kind, F. Link, F. P. Lucente, S. Monna, C. Montuori, S. Mroczek, A. Paul, C. Piromallo, J. Plomerová, J. Rewers, S. Salimbeni, F. Tilmann, P. Środa, J. Vergne, and the AlpArray-PACASE Working Group, 2023: Moho depths beneath the European Alps: a homogeneously processed map and receiver functions database. *Earth System Science Data*, **15 (5)**, 2117–2138.

Michelini, A., S. Cianetti, S. Gaviano, C. Giunchi, D. Jozinović, and V. Lauciani, 2021: INSTANCE – the Italian seismic dataset for machine learning. *Earth System Science Data*, **13 (12)**, 5509–5544, URL https://essd.copernicus.org/articles/13/5509/2021/.

Mousavi, S., W. Ellsworth, Z. Weiqiang, L. Chuang, and G. Beroza, 2020: Earthquake transformer—an attentive deep-learning model for simultaneous earthquake detection and phase picking. *Nature Communications*, **11**, 3952.

Mousavi, S., Y. Sheng, Z. Weiqiang, and G. Beroza, 2019: STanford EArthquake Dataset (STEAD): A Global Data Set of Seismic Signals for AI. *IEEE Access*, **7**, 179 464–179 476.

Mroczek, S. and F. Tilmann, 2021: Joint ambient noise auto-correlation and receiver function analysis of the Moho. *Geophysical Journal International*, **225 (3)**, 1920–1934.

Münchmeyer, J., D. Bindi, U. Leser, and F. Tilmann, 2021: Earthquake magnitude and location estimation from real time seismic waveforms with a transformer network. *Geophysical Journal International*, **226 (2)**, 1086–1104.

Münchmeyer, J., J. Woollam, A. Rietbrock, F. Tilmann, D. Lange, T. Bornstein, T. Diehl, C. Giunchi, F. Haslinger, D. Jozinović, A. Michelini, J. Saul, and H. Soto, 2022: Which Picker Fits My Data? A Quantitative Evaluation of Deep Learning Based Seismic Pickers. *Journal of Geophysical Research: Solid Earth*, **127 (1)**, e2021JB023 499, URL https://agupubs.onlinelibrary.wiley.com/doi/abs/10.1029/2021JB023499.

NCEDC, 2013: Northern California Earthquake Data Center. Dataset. URL https://www.ncedc.org/.

Paffrath, M., W. Friederich, S. Schmid, M. Handy, and the AlpArray and AlpArray-Swath D Working Group , 2021: Imaging structure and geometry of slabs in the greater Alpine area – a P-wave traveltime tomography using AlpArray Seismic Network data. *Solid Earth*, **12 (11)**, 2671–2702.

Pavlis, G. L. and J. R. Booker, 1980: The mixed discrete-continuous inverse problem: Application to the simultaneous determination of earthquake hypocenters and velocity structure. *Journal of Geophysical Research: Solid Earth*, **85 (B9)**, 4801–4810.

Plomerová, J., H. Žlebčíková, G. Hetényi, L. Vecsey, V. Babuška, and AlpArray-EASI and AlpArray working groups, 2022: Two subduction-related heterogeneities beneath the Eastern Alps and the Bohemian Massif imaged by high-resolution P-wave tomography. *Solid Earth*, **13 (1)**, 251–270, URL https://se.copernicus.org/articles/13/251/2022/.

Podvin, P. and I. Lecomte, 1991: Finite difference computation of traveltimes in very contrasted velocity models: a massively parallel approach and its associated tools. *Geophysical Journal International*, **105 (1)**, 271–284, URL https://doi.org/10.1111/j.1365-246X.1991.tb03461.x.

Pomella, H., M. Stipp, and B. Fügenschuh, 2012: Thermochronological record of thrusting and strike-slip faulting along the Giudicarie fault system (Alps, Northern Italy). *Tectonophysics*, **579**, 118–130, URL https://www.sciencedirect.com/science/article/pii/S0040195112002326.

Ratschbacher, L., W. Frisch, H.-G. Linzer, and O. Merle, 1991: Lateral extrusion in the eastern Alps, PArt 2: Structural analysis. *Tectonics*, **10 (2)**, 257–271, URL https://agupubs.onlinelibrary.wiley.com/doi/abs/10.1029/90TC02623.

Rietbrock, A., 2001: P wave attenuation structure in the fault area of the 1995 Kobe earthquake. *Journal of Geophysical Research: Solid Earth*, **106 (B3)**, 4141–4154, URL https://agupubs.onlinelibrary.wiley.com/doi/abs/10.1029/2000JB900234.

Ross, Z. E., M. Meier, E. Hauksson, and T. H. Heaton, 2018: Generalized Seismic Phase Detection with Deep Learning. *Bulletin of the Seismological Society of America*, **108 (5A)**, 2894–2901.

Ryberg, T. and C. Haberland, 2019: Bayesian simultaneous inversion for local earthquake hypocentres and 1-D velocity structure using minimum prior knowledge. *Geophysical Journal International*, **218 (2)**, 840–854, URL `https://doi.org/10.1093/gji/ggz177`.

Sadeghi-Bagherabadi, A., A. Vuan, A. Aoudia, S. Parolai, and The AlpArray and AlpArray-Swath-D Working Group, 2021: High-Resolution Crustal S-wave Velocity Model and Moho Geometry Beneath the Southeastern Alps: New Insights From the SWATH-D Experiment. *Frontiers in Earth Science*, **9**, 641 113.

SCEDC, 2013: Southern California Earthquake Data Center, Caltech. Dataset. URL `https://scedc.caltech.edu/`.

Schmid, S., D. Bernoulli, B. Fügenschuh, L. Matenco, S. Schefer, R. Schuster, M. Tischler, and K. Ustaszewski, 2008: The Alpine-Carpathian-Dinaridic orogenic system: Correlation and evolution of tectonic units. *Swiss Journal of Geosciences*, **101**, 139–183.

Schmid, S., B. Fügenschuh, E. Kissling, and R. Schuster, 2004: Tectonic map and overall architecture of the Alpine orogen. *Eclogae Geologicae Helvetiae*, **97**, 93–117.

Schmid, S., E. Kissling, T. Diehl, D. van Hinsbergen, and G. Molli, 2017: Ivrea mantle wedge, arc of the Western Alps, and kinematic evolution of the Alps–Apennines orogenic system. *Swiss Journal of Geosciences*, **110 (2)**, 581–612.

Schuster, R. and K. Stüwe, 2008: Permian metamorphic event in the Alps. *Geology*, **36 (8)**, 603–606.

SED at ETH Zurich, 1983: National Seismic Networks of Switzerland. URL `http://networks.seismo.ethz.ch/networks/ch/`.

Solarino, S., M. G. Malusà, E. Eva, S. Guillot, A. Paul, S. Schwartz, L. Zhao, C. Aubert, T. Dumont, S. Pondrelli, S. Salimbeni, Q. Wang, X. Xu, T. Zheng, and R. Zhu, 2018: Mantle wedge exhumation beneath the Dora-Maira (U)HP dome unravelled by local earthquake tomography (Western Alps). *Lithos*, **296-299**, 623–636.

Soto, H. and B. Schurr, 2021: DeepPhasePick: a method for detecting and picking seismic phases from local earthquakes based on highly optimized convolutional and recurrent deep neural networks. *Geophysical Journal International*, **227 (2)**, 1268–1294.

Spada, M., I. Bianchi, E. Kissling, N. Agostinetti, and S. Wiemer, 2012: Combining controlled-source seismology and receiver function information to derive 3-D Moho topography for Italy. *Geophysical Journal International*, **194 (2)**, 1050–1068.

Spencer, C. and D. Gubbins, 1980: Travel-time inversion for simultaneous earthquake location and velocity structure determination in laterally varying media. *Geophysical Journal International*, **63 (1)**, 95–116.

Stampfli, G. and G. Borel, 2002: A plate tectonic model for the Paleozoic and Mesozoic constrained by dynamic plate boundaries and restored synthetic oceanic isochrons. *Earth and Planetary Science Letters*, **196 (1)**, 17–33.

Thouvenot, F., A. Paul, G. Sénéchal, A. Hirn, and R. Nicolich, 1996: Comparison between two techniques of line-drawing migration (ray-tracing and common tangent method). *Bulletin de la Société Géologique de France*, **170**, 53–59.

Thurber, C., 1983: Earthquake locations and three-dimensional crustal structure in the Coyote Lake Area, central California. *Journal of Geophysical Research: Solid Earth*, **88 (B10)**, 8226–8236.

Thurber, C. and D. Eberhart-Phillips, 1999: Local earthquake tomography with flexible gridding. *Computers & Geosciences*, **25 (7)**, 809–818.

Toomey, D. R. and G. R. Foulger, 1989: Tomographic inversion of local earthquake data from the Hengill-Grensdalur Central Volcano Complex, Iceland. *Journal of Geophysical Research: Solid Earth*, **94 (B12)**, 17 497–17 510.

Um, J. and C. Thurber, 1987: A fast algorithm for two-point seismic ray tracing. *Bulletin of the Seismological Society of America*, **77 (3)**, 972–986.

van der Hilst, R. D., E. R. Engdahl, and W. Spakman, 1993: Tomographic inversion of P and pP data for aspherical mantle structure below the northwest Pacific region. *Geophysical Journal International*, **115 (1)**, 264–302.

Wagner, M., S. Husen, A. Lomax, E. Kissling, and D. Giardini, 2013: High-precision earthquake locations in Switzerland using regional secondary arrivals in a 3-D velocity model. *Geophysical Journal International*, **193 (3)**, 1589–1607.

Weiqiang, Z. and G. Beroza, 2018: PhaseNet: A Deep-Neural-Network-Based Seismic Arrival Time Picking Method. *Geophysical Journal International*, **216 (1)**, 261–273.

Woollam, J., J. Münchmeyer, F. Tilmann, A. Rietbrock, D. Lange, T. Bornstein, T. Diehl, C. Giunchi, F. Haslinger, D. Jozinović, A. Michelini, J. Saul, and H. Soto, 2022: SeisBench—A Toolbox for Machine Learning in Seismology. *Seismological Research Letters*, **93 (3)**, 1695–1709.

Woollam, J., A. Rietbrock, A. Bueno Rodriguez, and S. De Angelis, 2019: Convolutional Neural Network for Seismic Phase Classification, Performance Demonstration over a Local Seismic Network. *Seismological Research Letters*, **90 (2a)**, 491–502.

Zhao, L., M. Malusà, H. Yuan, A. Paul, S. Guillot, Y. Lu, L. Stehly, S. Solarino, E. Eva, G. Lu, T. Bodin, and CIFALPS Group & AlpArray Working Group, 2020: Evidence for a serpentinized plate interface favouring continental subduction. *Nature Communications*, **11**, 2171.

Zhao, L., A. Paul, S. Guillot, S. Solarino, M. Malusà, T. Zheng, S. Salimbeni, T. Dumont, S. Schwartz, R. Zhu, and Q. Wang, 2015: First Seismic Evidence for Continental Subduction beneath the Western Alps. *Geology*, **43 (9)**, 815–818.

Zhao, L., A. Paul, M. G. Malusà, X. Xu, T. Zheng, S. Solarino, S. Guillot, S. Schwartz, T. Dumont, S. Salimbeni, C. Aubert, S. Pondrelli, Q. Wang, and R. Zhu, 2016a: Continuity of the Alpine slab unraveled by high-resolution P wave tomography. *Journal of Geophysical Research: Solid Earth*, **121 (12)**, 8720–8737.

Zhao, L., A. Paul, S. Solarino, and RESIF, 2016b: Seismic network YP: CIFALPS temporary experiment (China-Italy-France Alps seismic transect). URL `https://seismology.resif.fr/networks/#/YP__2012`.

———, 2018: Seismic network XT: CIFALPS-2 temporary experiment (China-Italy-France Alps seismic transect . URL `https://seismology.resif.fr/networks/#/XT__2018`.

Zuffetti, C. and R. Bersezio, 2021: Space-time geological model of the quaternary syntectonic fill of a foreland basin (po basin, northern italy). *Sedimentary Geology*, **421**, 105 945.

A. Appendix for chapter 4

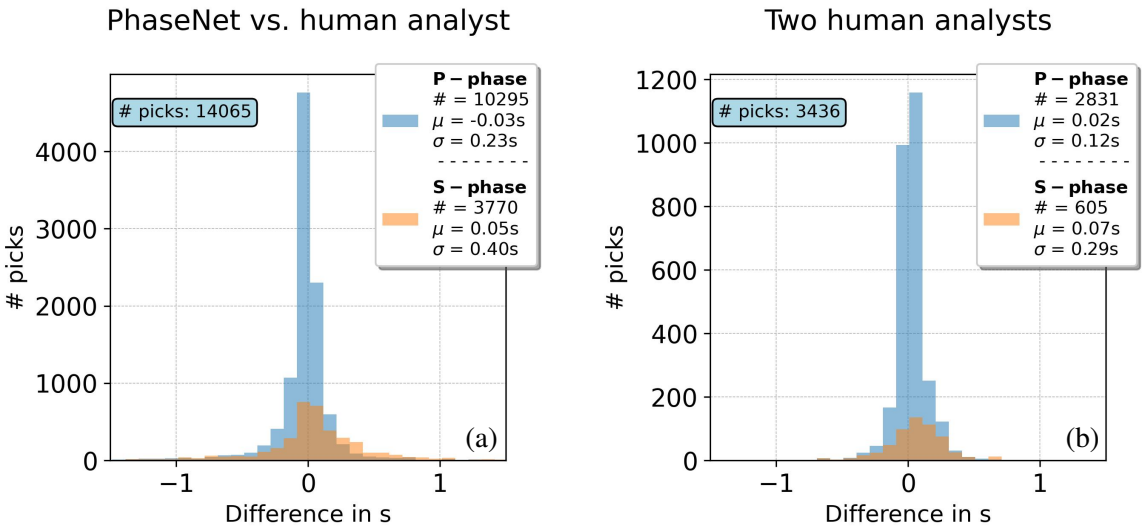

Figure A.2.: (a) Comparison of *PhaseNet* and manually determined *P*- & *S*-phase arrival times from 30 events. (b) Comparison of *P*- & *S*-phase arrival times of 6 events independently picked by two human analysts.

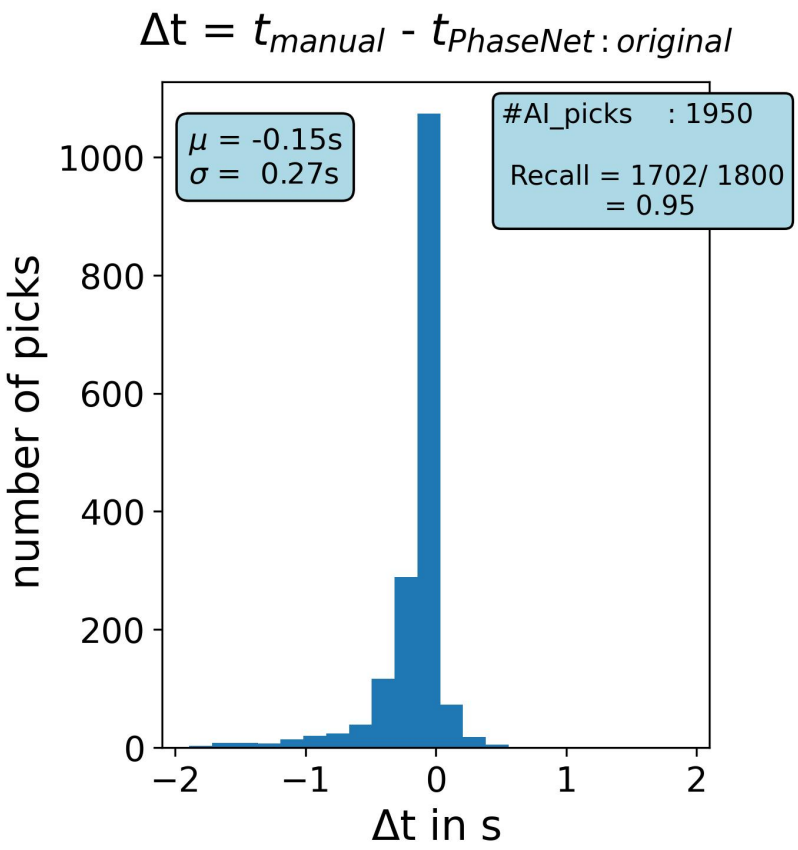

Figure A.1.: Assessment of PhaseNet's performance when compared to the high quality manually determined *P*-phase arrival time catalogue from Diehl et al. (2009a).

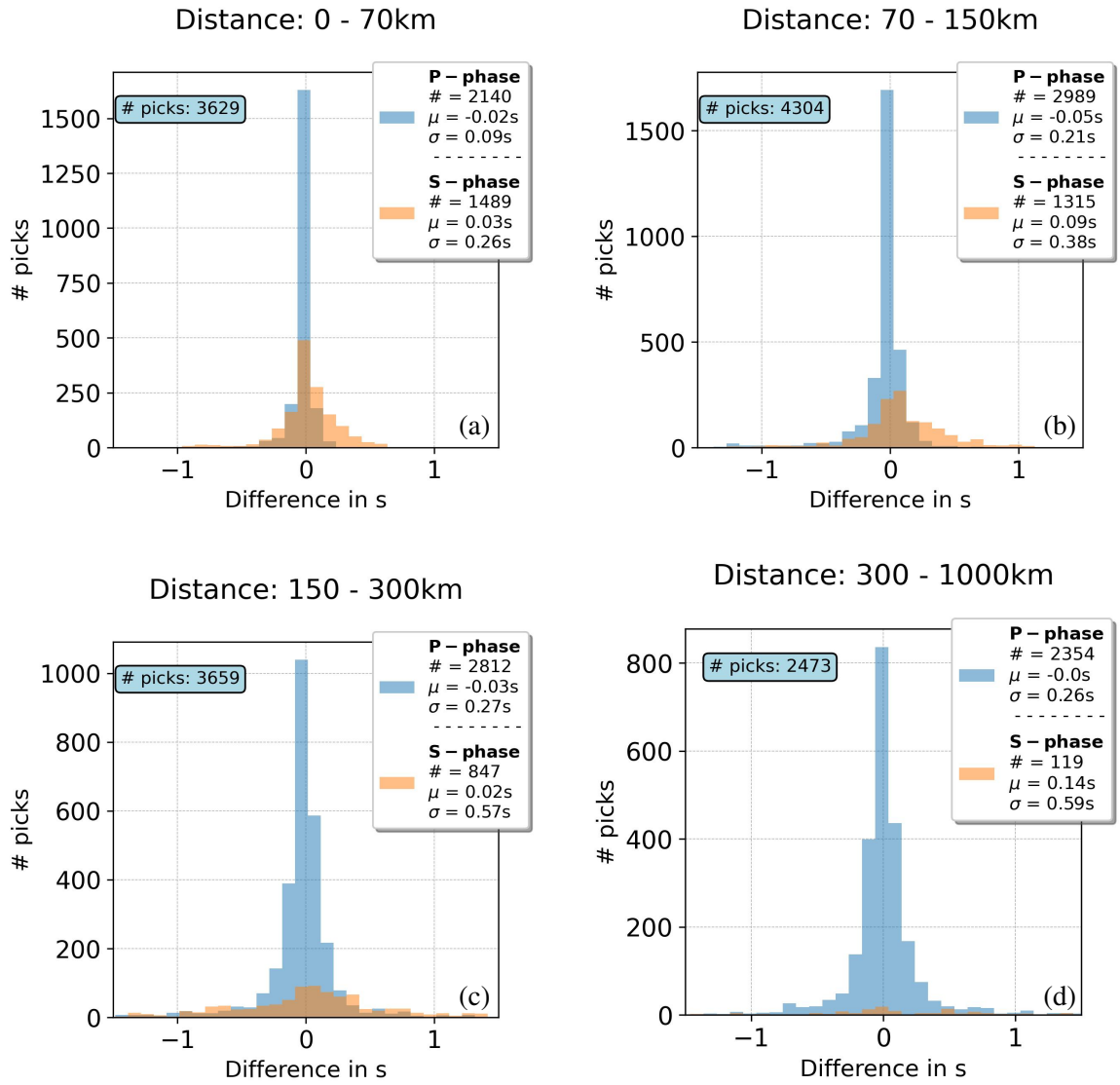

Figure A.3.: Comparison of *PhaseNet* against manually determined *P*- and *S*-phase arrival times as in Fig. A.2(a) for the epidistance ranges from 0-70km (a), 70-150km (b), 150-300km (c) & 300-1000km (d).

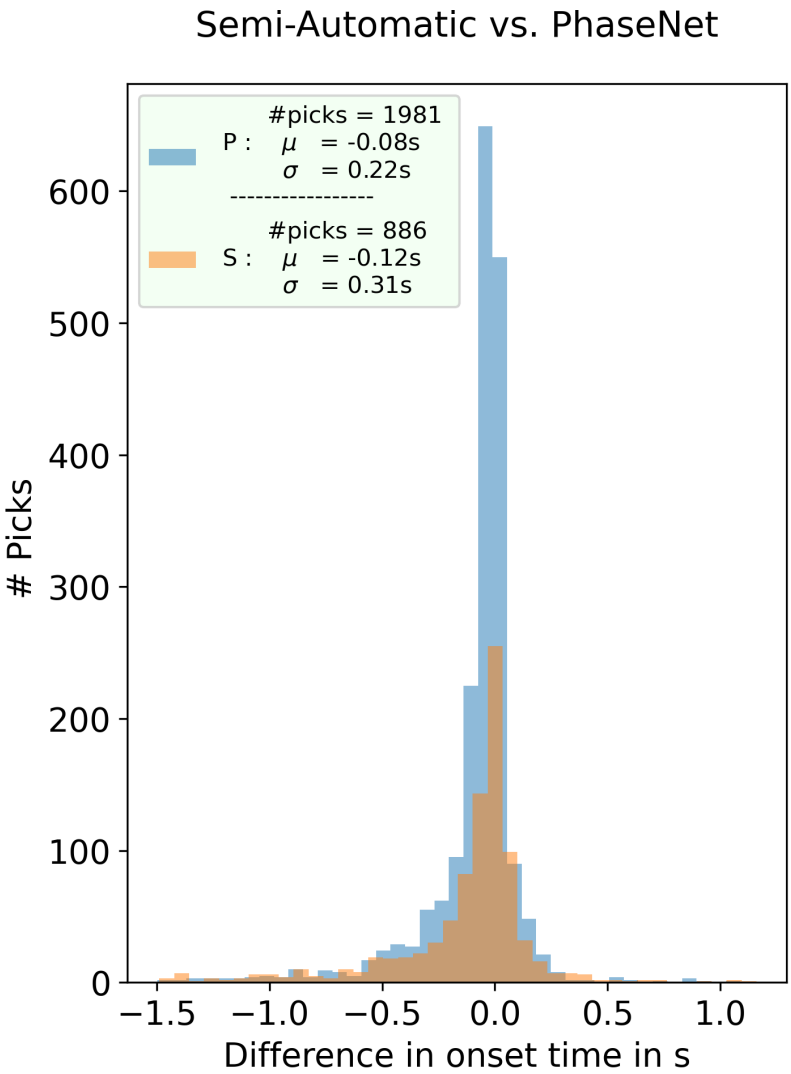

Figure A.4.: Assessment of *PhaseNet's* performance when compared to the manually revised *P*- & *S*-phase picks from Jozi Najafabadi et al. (2021).

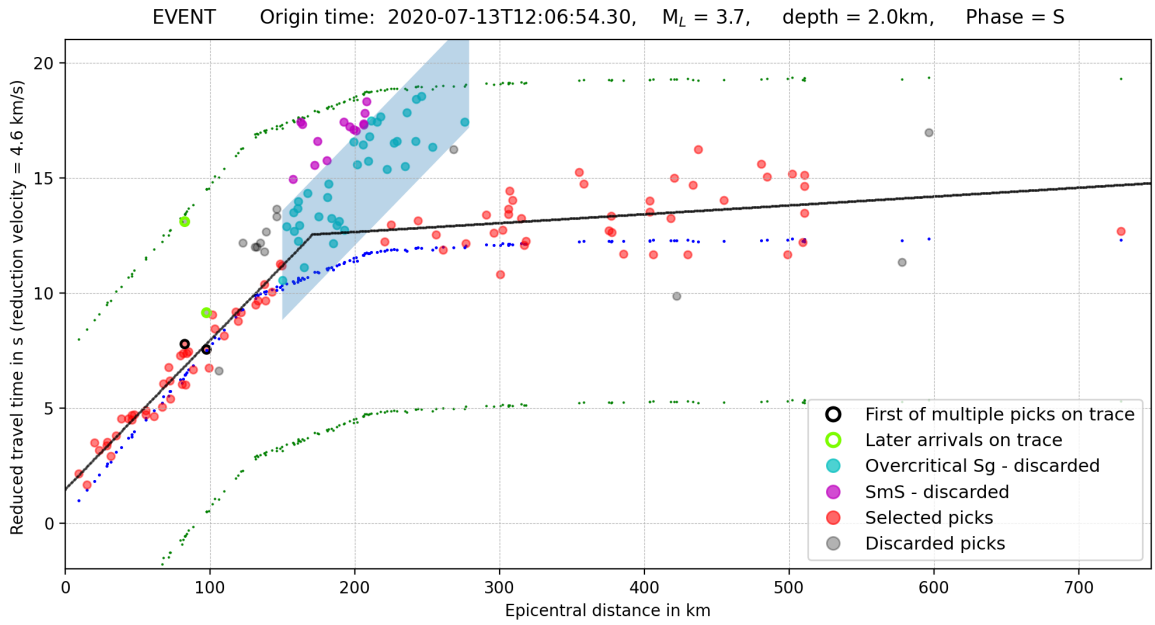

Figure A.5.: Illustration of the 2-fit method to discard erroneous picks. *PhaseNet S*-phase arrivals are plotted over epicentral distance with a reduction velocity of 4.6 km/s. The corridor of considered picks is marked with green crosses at ± 7 s around the synthetic onset (blue crosses). A linear regression is fit through the picks from 0 - 100 km and then extrapolated. All picks within the blue corridor at $\Delta \geq 150$ km within 4σ of this fit are labelled as overcritical *Sg*-phases (cyan) and discarded. Later phases with $\Delta \geq 150$ km are discarded as *SmS*-arrivals (purple). A second weighted linear regression is fit through arrivals from 250 - 700 km and extrapolated until its interjection point with the first fit. Arrivals within 2σ of the fits plotted in red are selected, while the remaining picks marked in grey are discarded. In the case of more than one arrival on the same trace, only the first arrival within 2σ of the fit is considered. First and later arrivals on the same trace are marked with black and lime edgecolors, respectively.

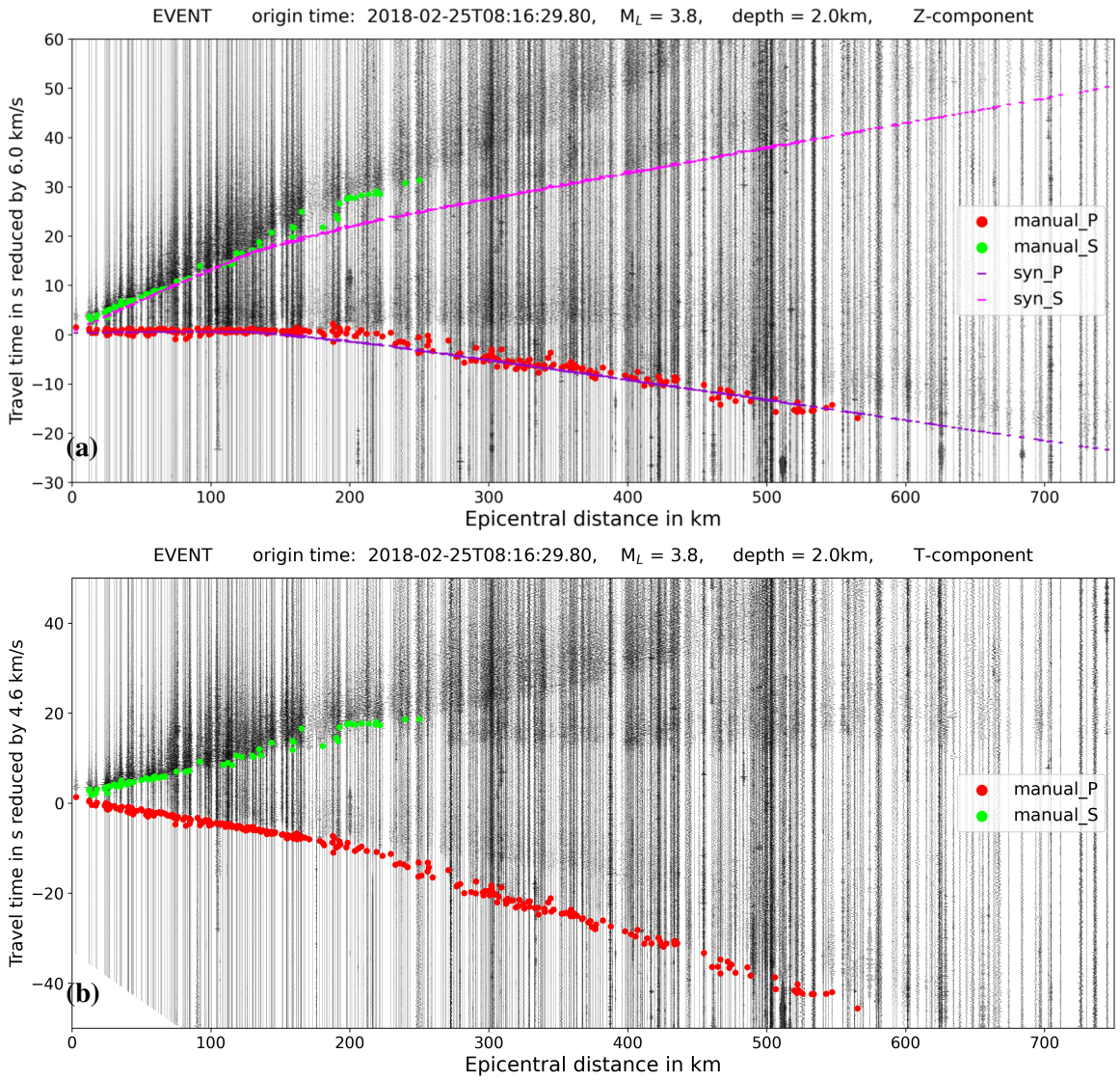

Figure A.6.: Event section plots of the same event as in Figure 4.4(a) with manually determined *P*- and *S*-phase arrivals marked in red and green, respectively. (a) *Z*-component reduced by the approximate velocity of the direct *Pg*-wave $v_{red} = 6.0 km/s$. (b) *T*-component reduced by the approximate velocity of the *Sn*-wave $v_{red} = 4.6 km/s$.

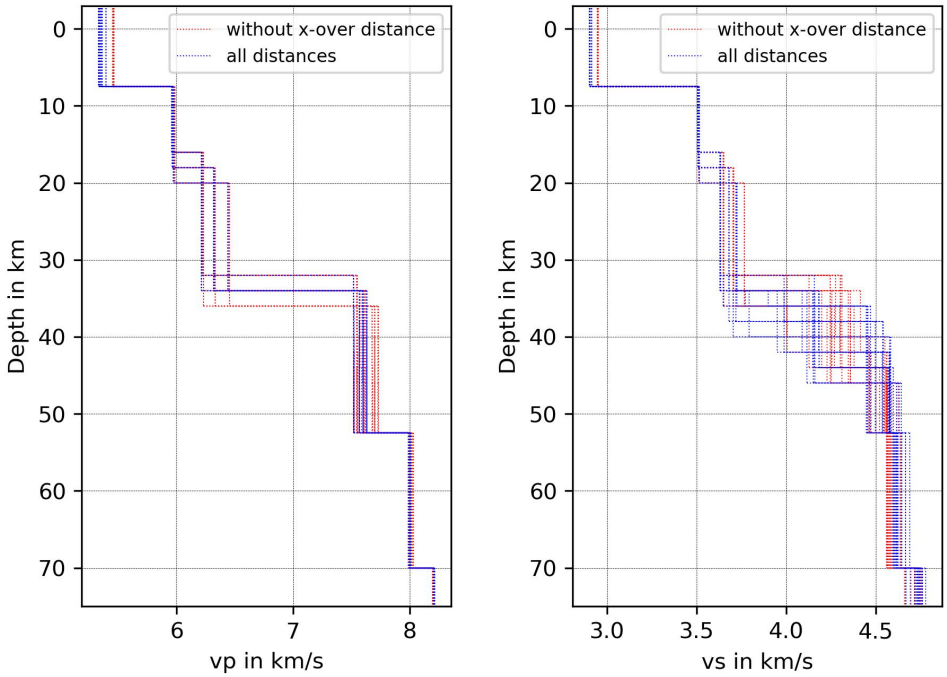

Figure A.7.: Comparison of the the 20 best fitting v_p (left) and v_s (right) *VELEST* models based on picks catalogs excluding (red) and including (blue) the cross-over range from 130 - 300km.

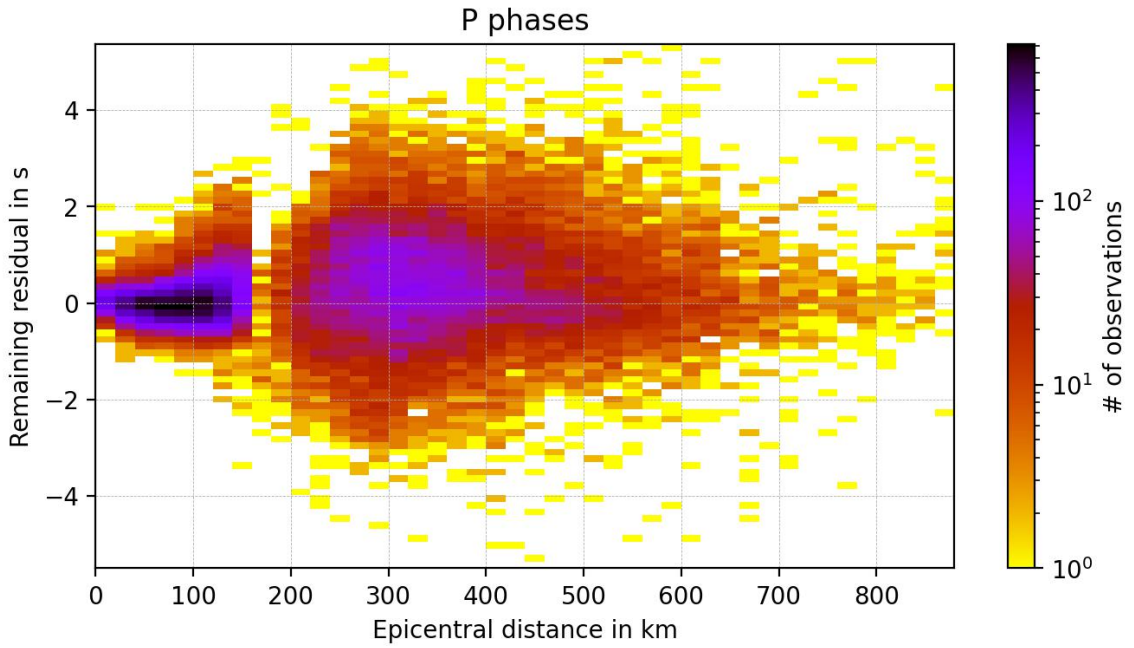

Figure A.8.: Remaining *P*-phase residuals of observations from the entire epicentral range corresponding to the *VELEST* model which has been computed excluding picks from the cross-over distance range from 130 - 300km.

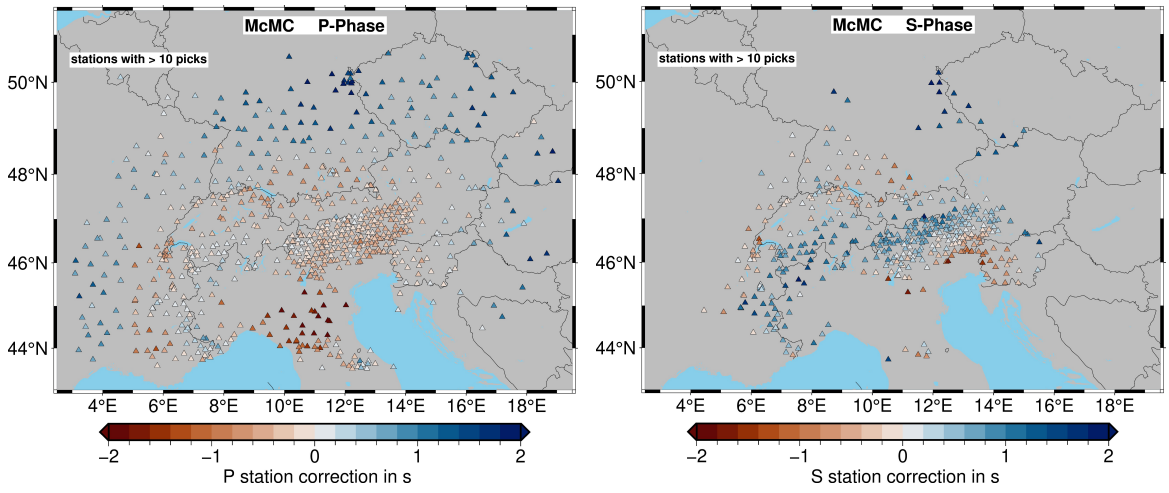

Figure A.9.: *P*- & *S*-phase station correction terms corresponding to the *GAR1D_PS_McMC* model based on observations from all distances.

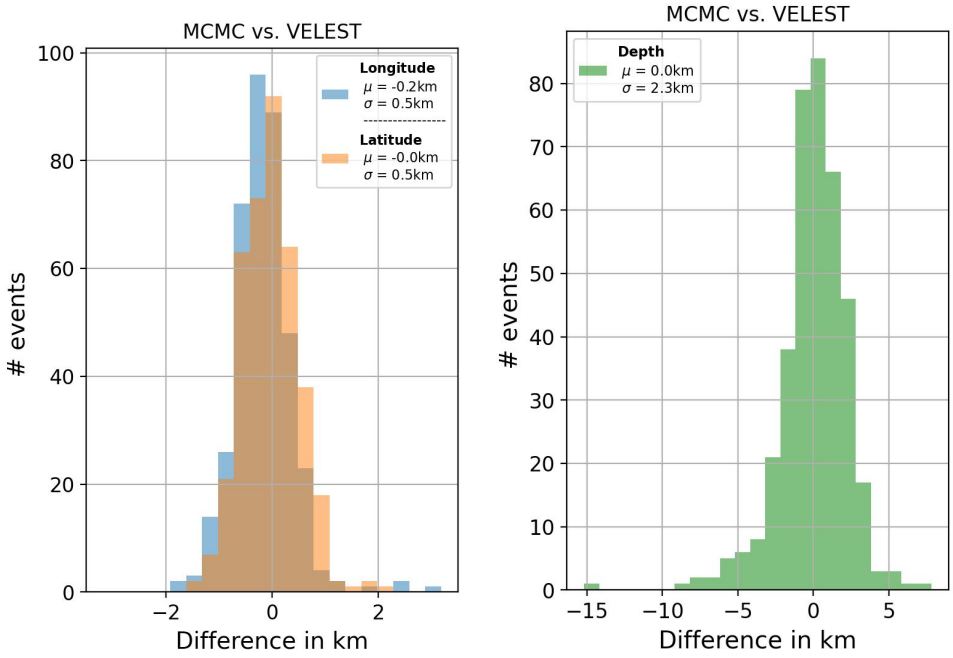

Figure A.10.: Differences in longitude & latitude (left) and depth (right) when comparing *VELEST* and *MCMC* final event locations derived in this study.

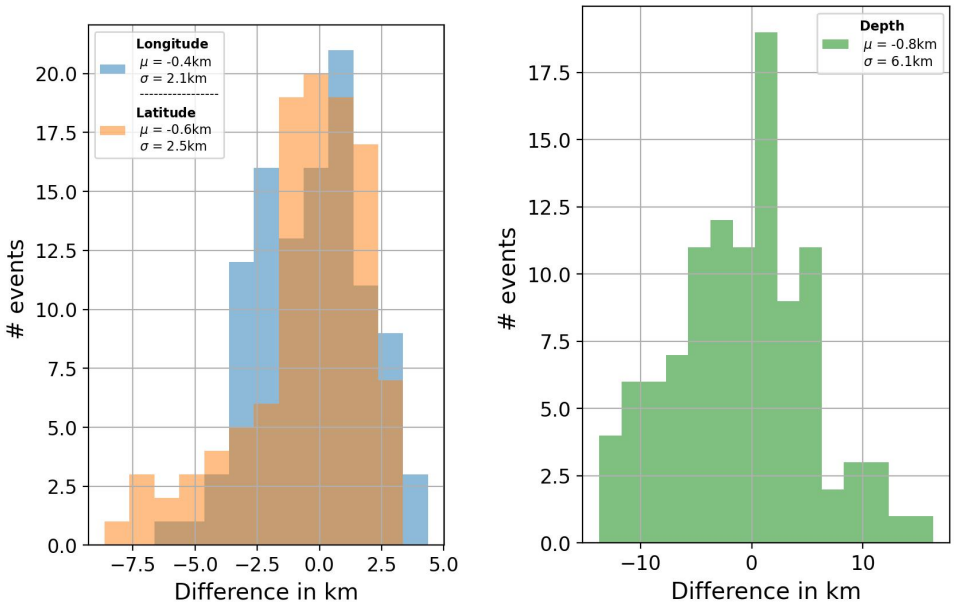

Figure A.11.: Comparison of event locations from Bagagli et al. (2022) and Jozi Najafabadi et al. (2021). Horizontal and vertical discrepancies of epicentres are shown in the left and right panel, respectively.

B. Appendix for chapter 5

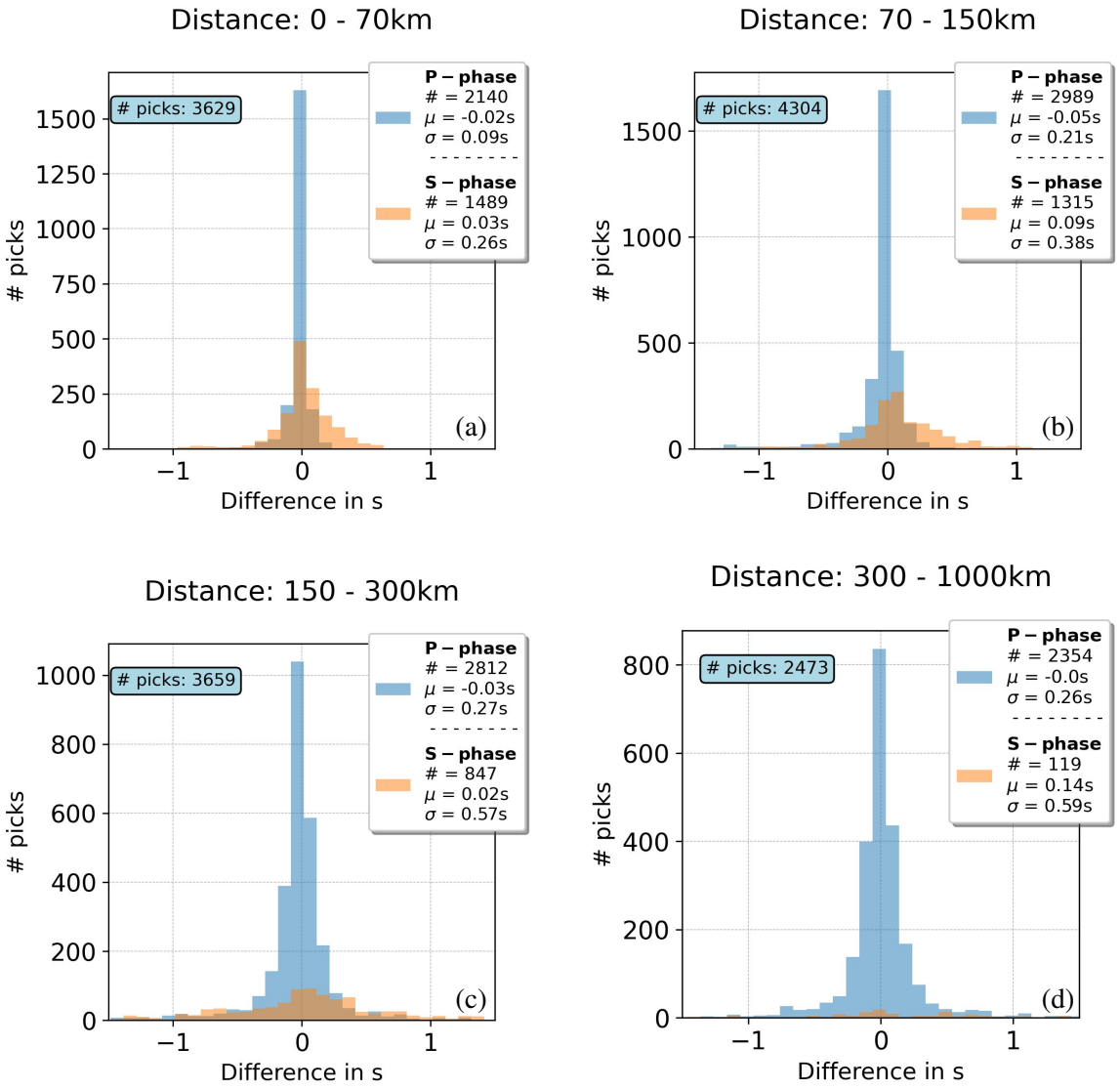

Figure B.1.: Comparison of *PhaseNet* against manually determined *P*- and *S*-phase arrival times for the epidistance ranges from 0-70km (a), 70-150km (b), 150-300km (c) & 300-1000km (d). Figure is taken from Braszus et al. (2024).

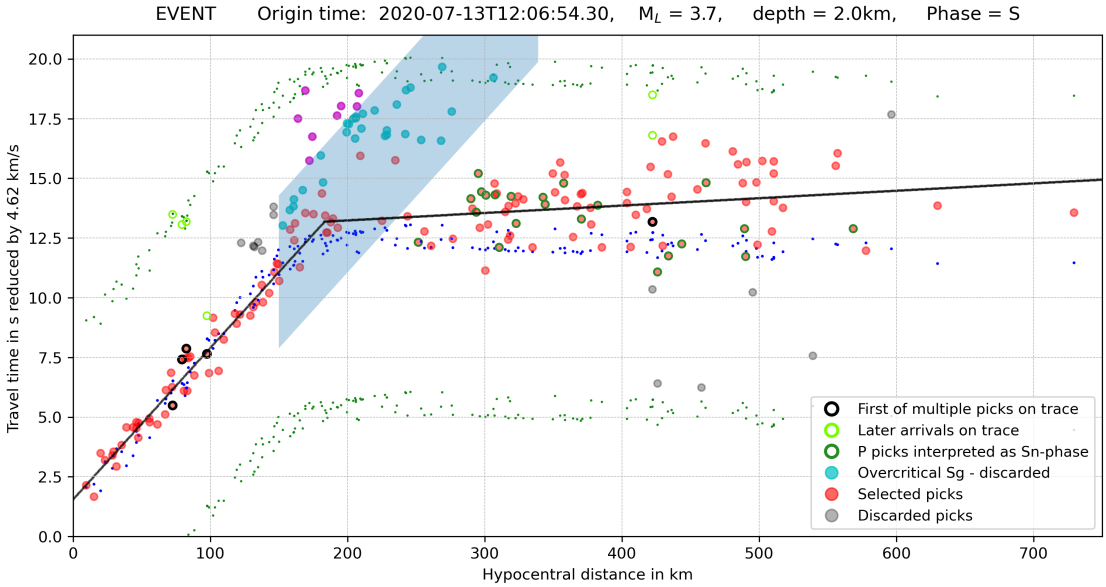

Figure B.2.: Application of the *2-fit method* to *S*-phase arrivals. Picks are selected or discarded based on their proximity to the respective regression line which is fit through the *Sg* and *Sn* arrivals. Darkgreen edgecolors mark picks that initially were labelled as *P*-phases by *PhaseNet*. Due to their proximity to the synthetic *Sn*-onset they are considered to be *S*-phases. Further detail on the *2-fit method* can be found in section 5.3.4.

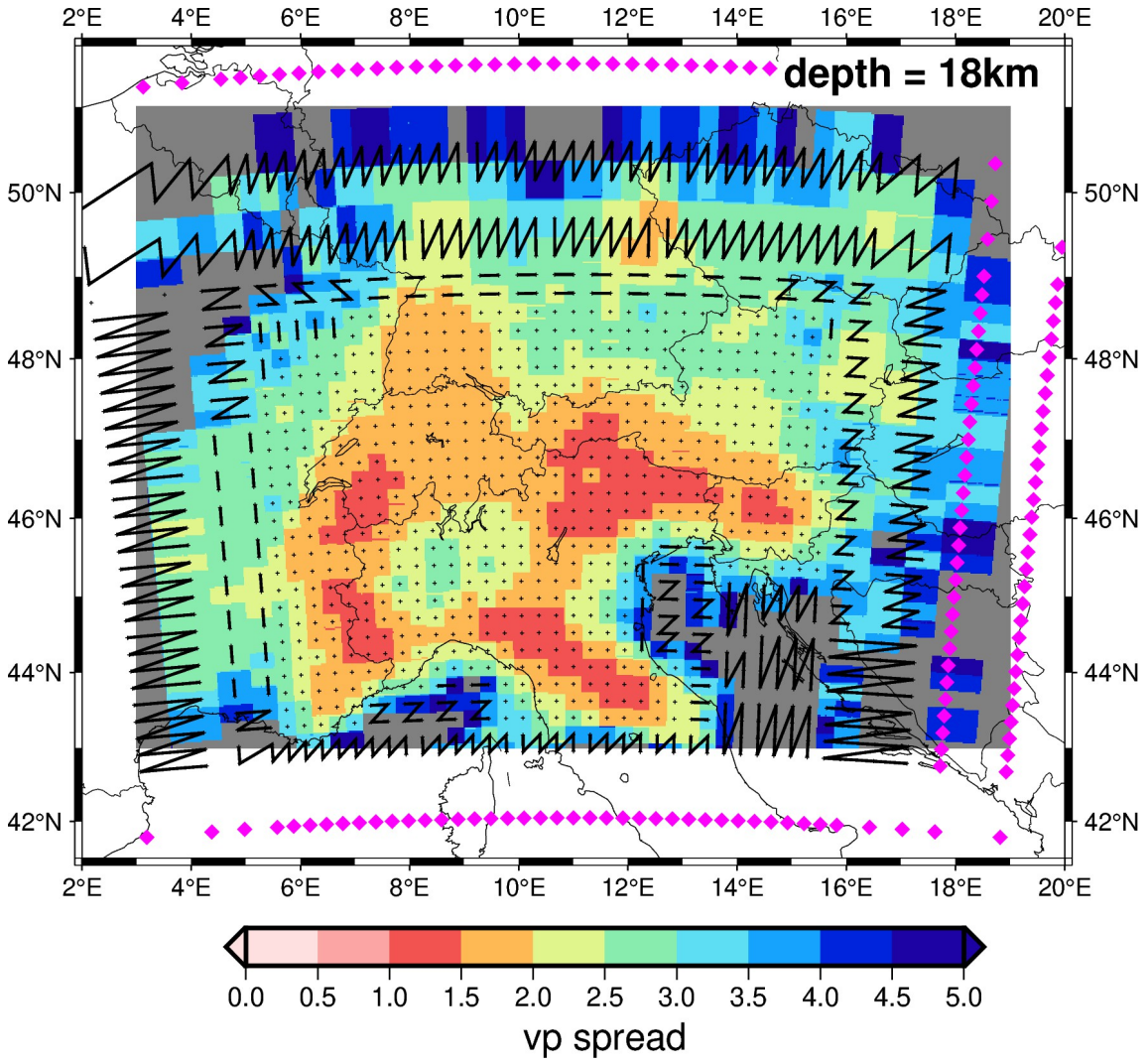

Figure B.3.: Illustration of fixed (pink diamonds) and linked (black lines) nodes together with the v_p spread value at a depth of 18 km. The outermost nodes are fixed to their initial value throughout all inversion steps. Neighboring nodes on the edge of the resolved area are linked together and thus are updated identically in each iteration of the SIMUL2023 algorithm.

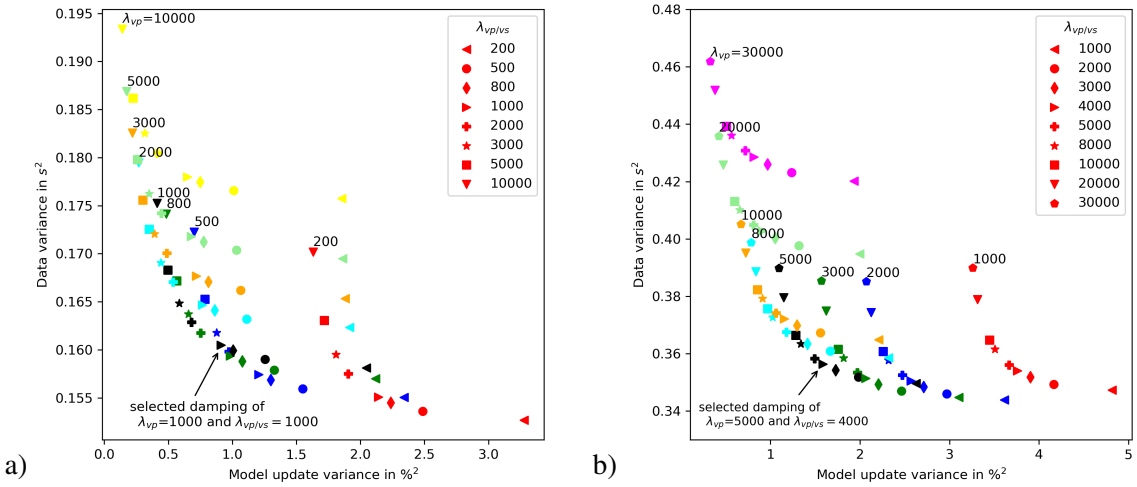

Figure B.4.: Trade of curves based on which the ideal damping value for the damped least squares inversion of v_p (left) and v_p/v_s (right) is determined.

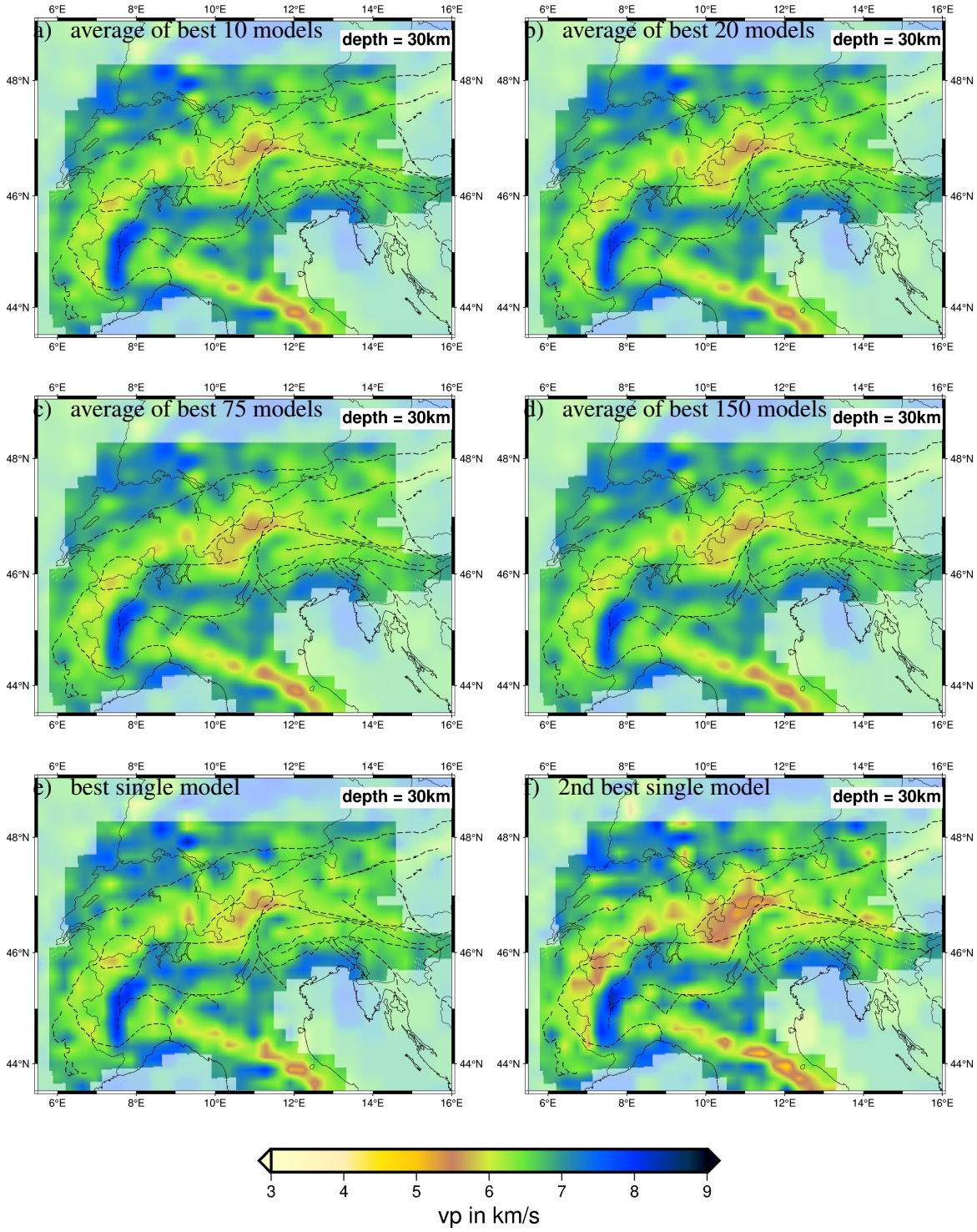

Figure B.5.: Panels a)-d) show the v_p structure at 30 km depth as averages of the 10, 20, 75 and 150 models with the lowest data misfit, respectively. Panels e) and f) display the single models with the best and second-best misfit reduction, respectively.

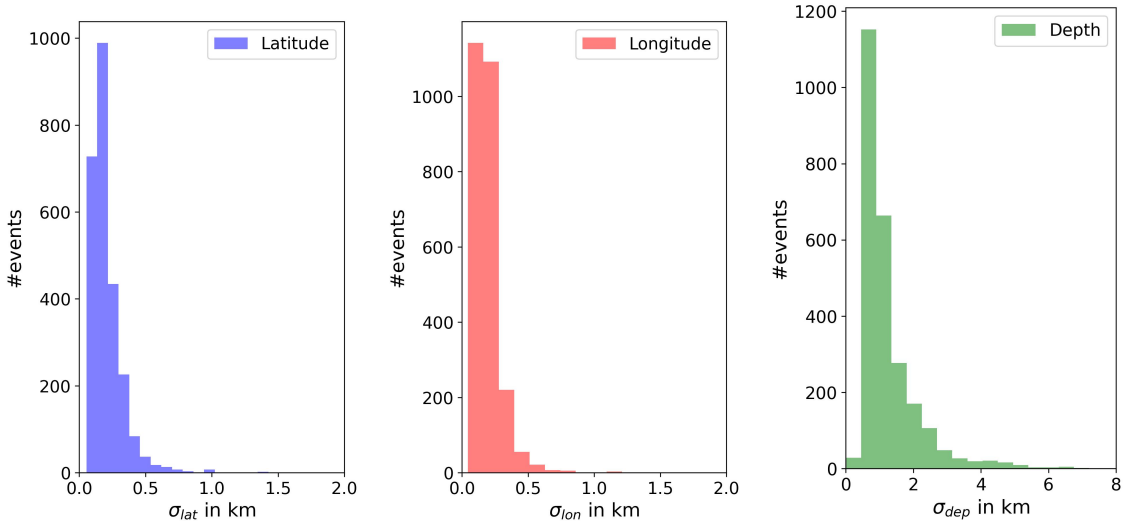

Figure B.6.: Standard deviations of all 2553 hypocentres based on the best 200 inversion runs with shifted initial hypocentres, perturbed 1D starting model and varying grid parametrization. Thus, the influence of these initial parameters on the final hypocentres can be quantified as less than 0.5 km horizontally and less than 3.0 km vertically.

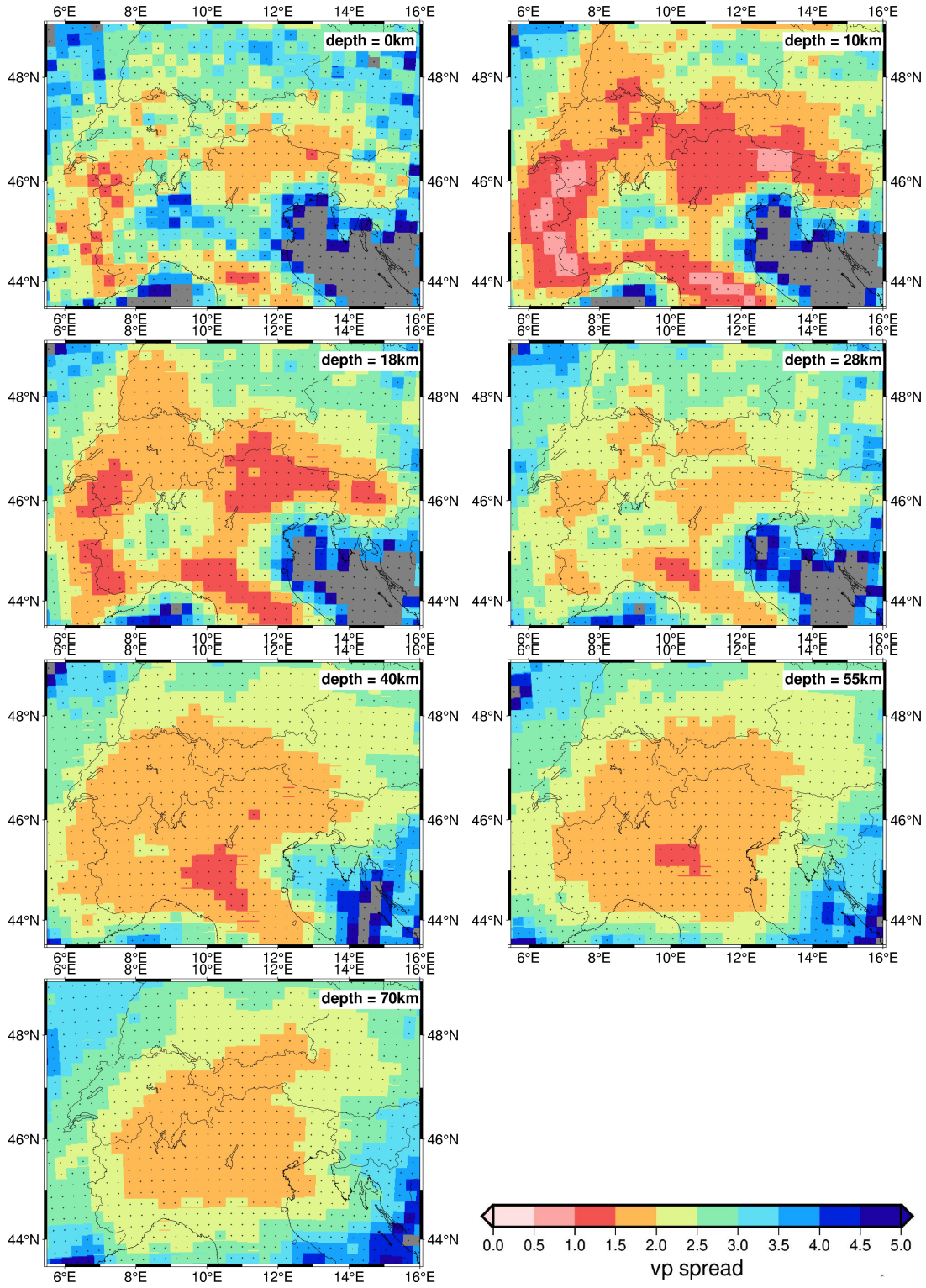

Figure B.7.: Depth slices of spread function values for v_p nodes.

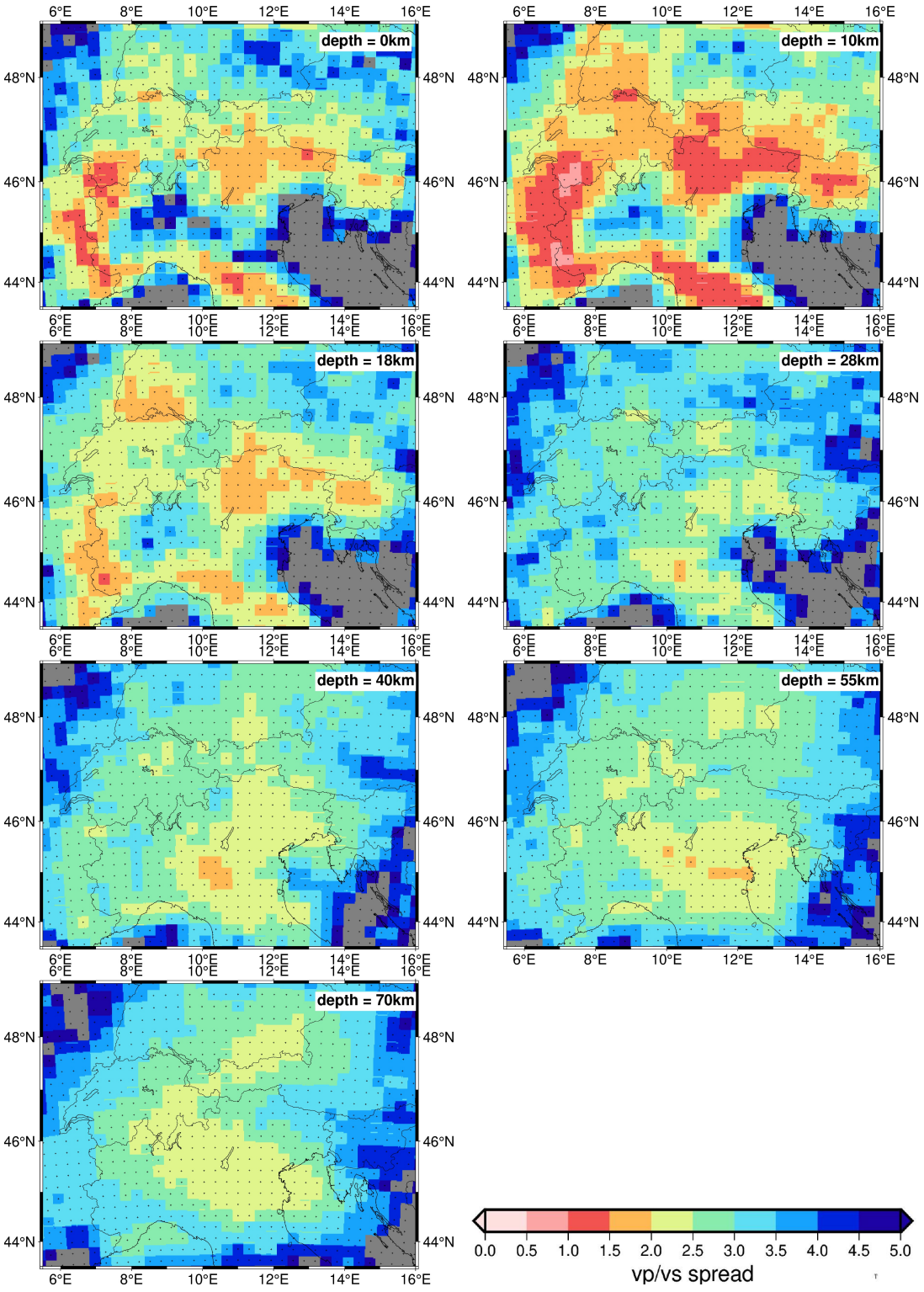

Figure B.8.: Depth slices of spread function values for v_p/v_s nodes.

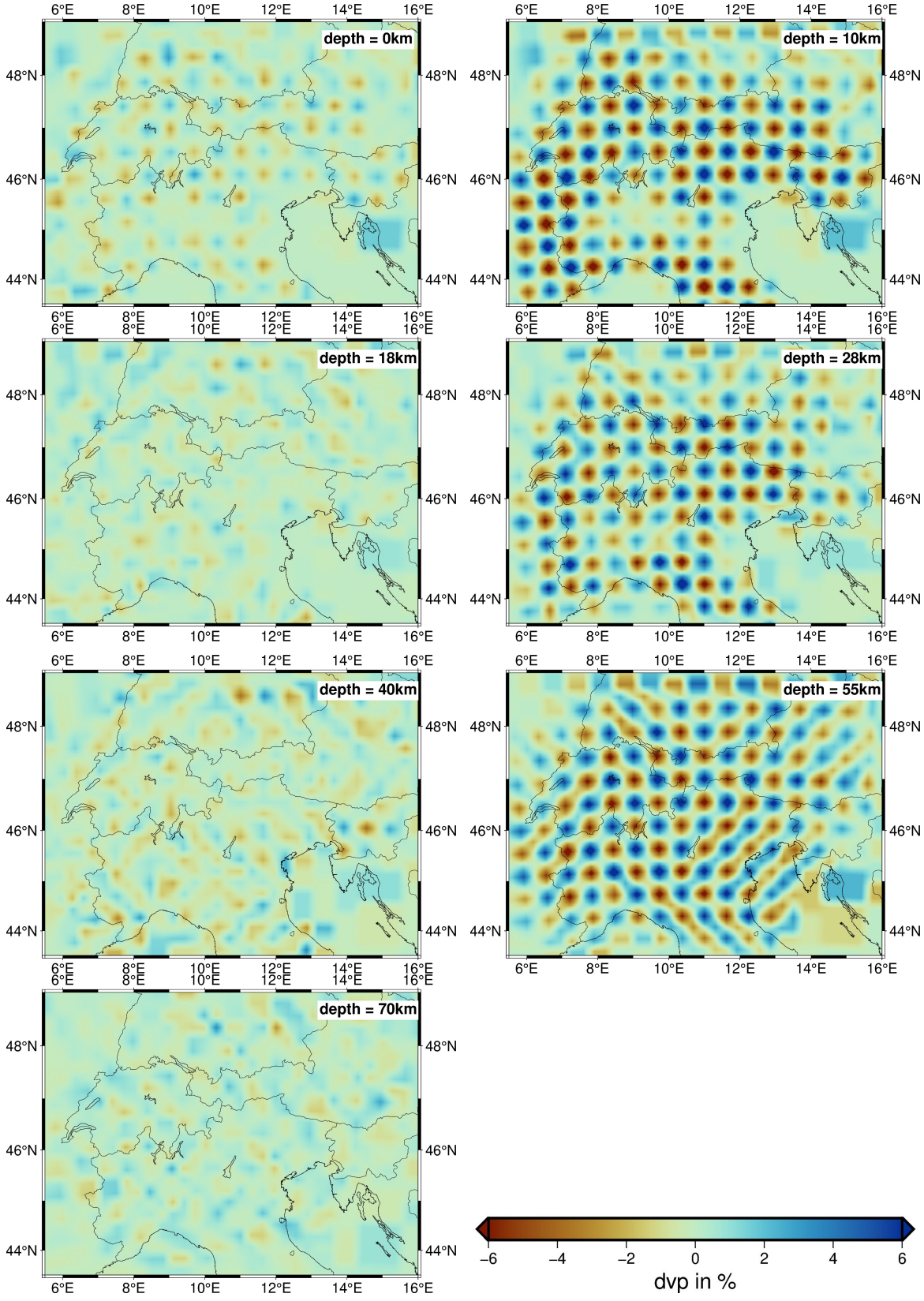

Figure B.9.: Recovery of checkerboard anomalies with ±10% *vp* perturbations in even numbered layers (right column).

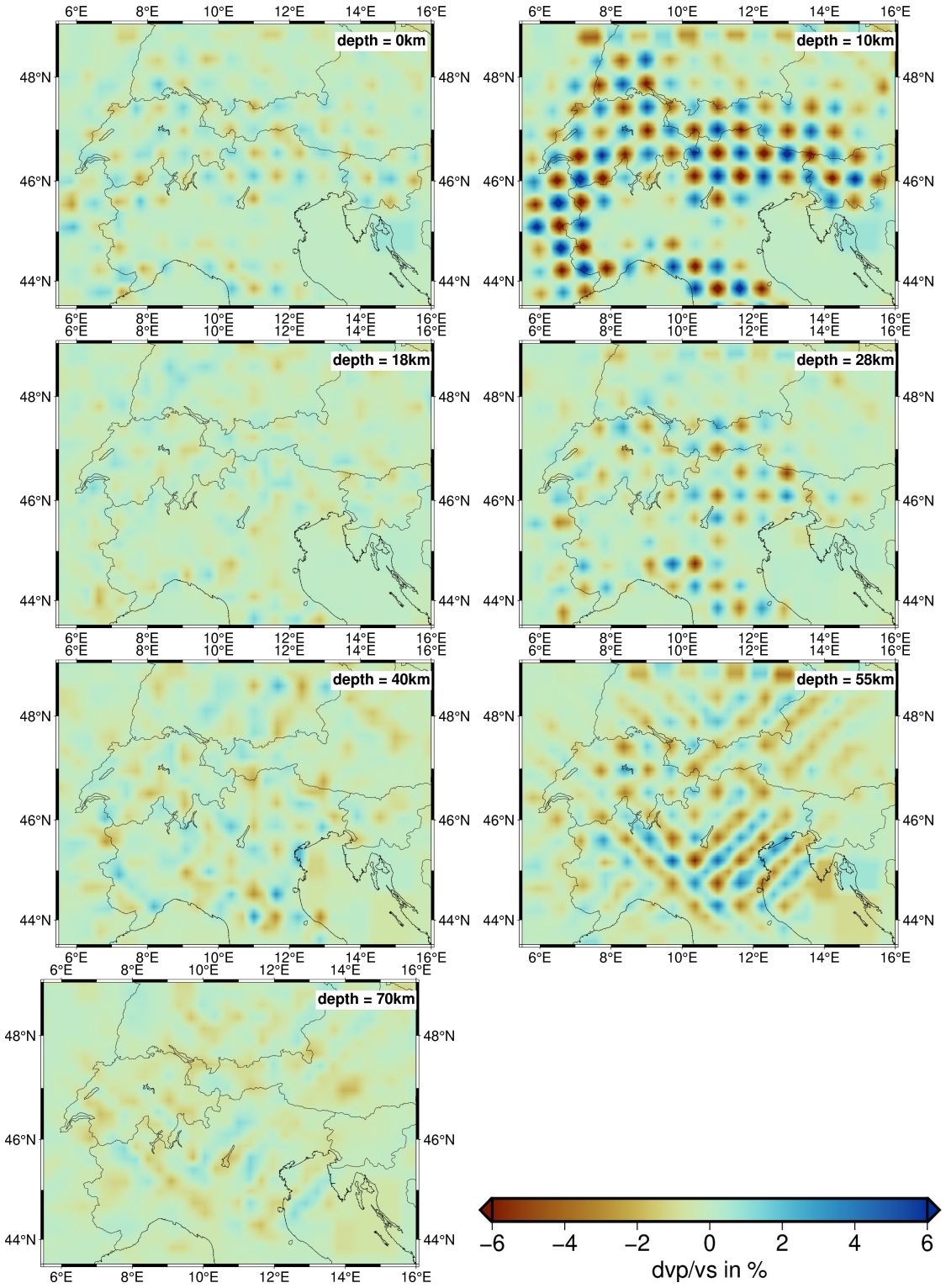

Figure B.10.: Recovery of checkerboard anomalies with ±10% *vp/vs* perturbations in even numbered layers (right column).

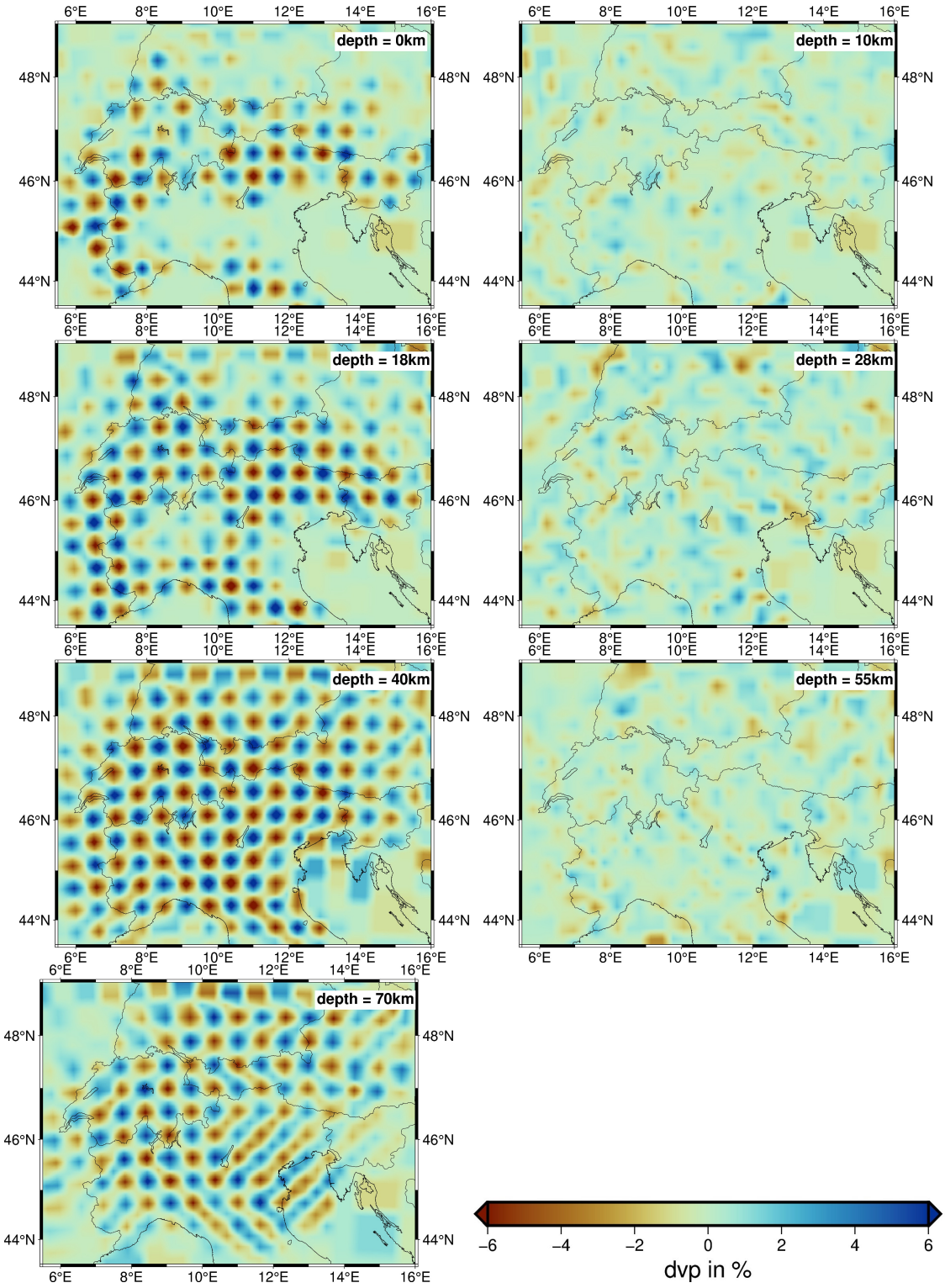

Figure B.11.: Recovery of checkerboard anomalies with ±10% *vp* perturbations in odd numbered layers (left column).

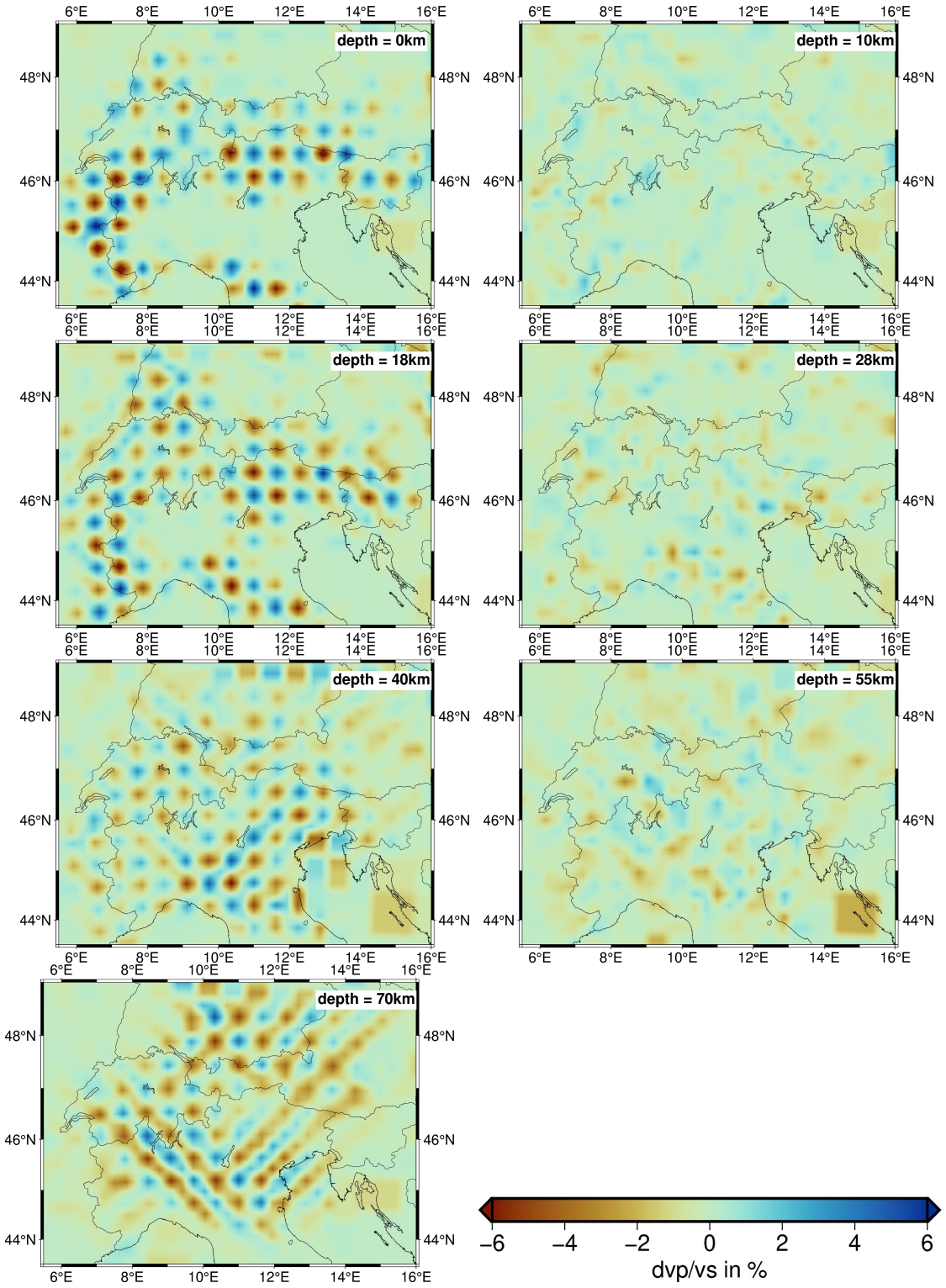

Figure B.12.: Recovery of checkerboard anomalies with ±10% *vp/vs* perturbations in odd numbered layers (left column).

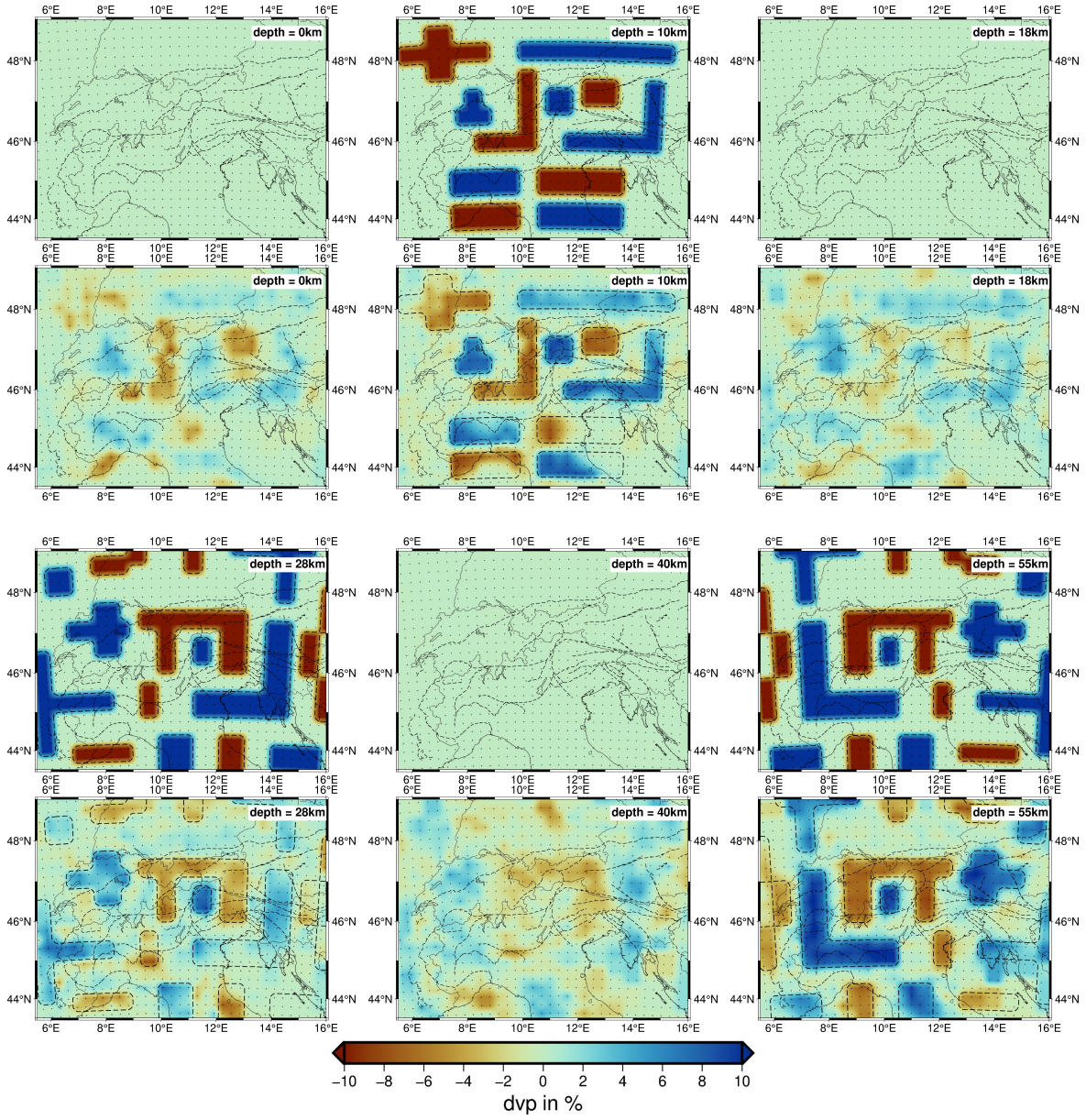

Figure B.13.: Reconstruction of irregular perturbations of $\pm 10\%$ in v_p in even numbered layers. Synthetic models are displayed in the first and third row. Reconstructed models are shown in the second and fourth row. Dashed lines mark the outlines of synthetic anomalies.

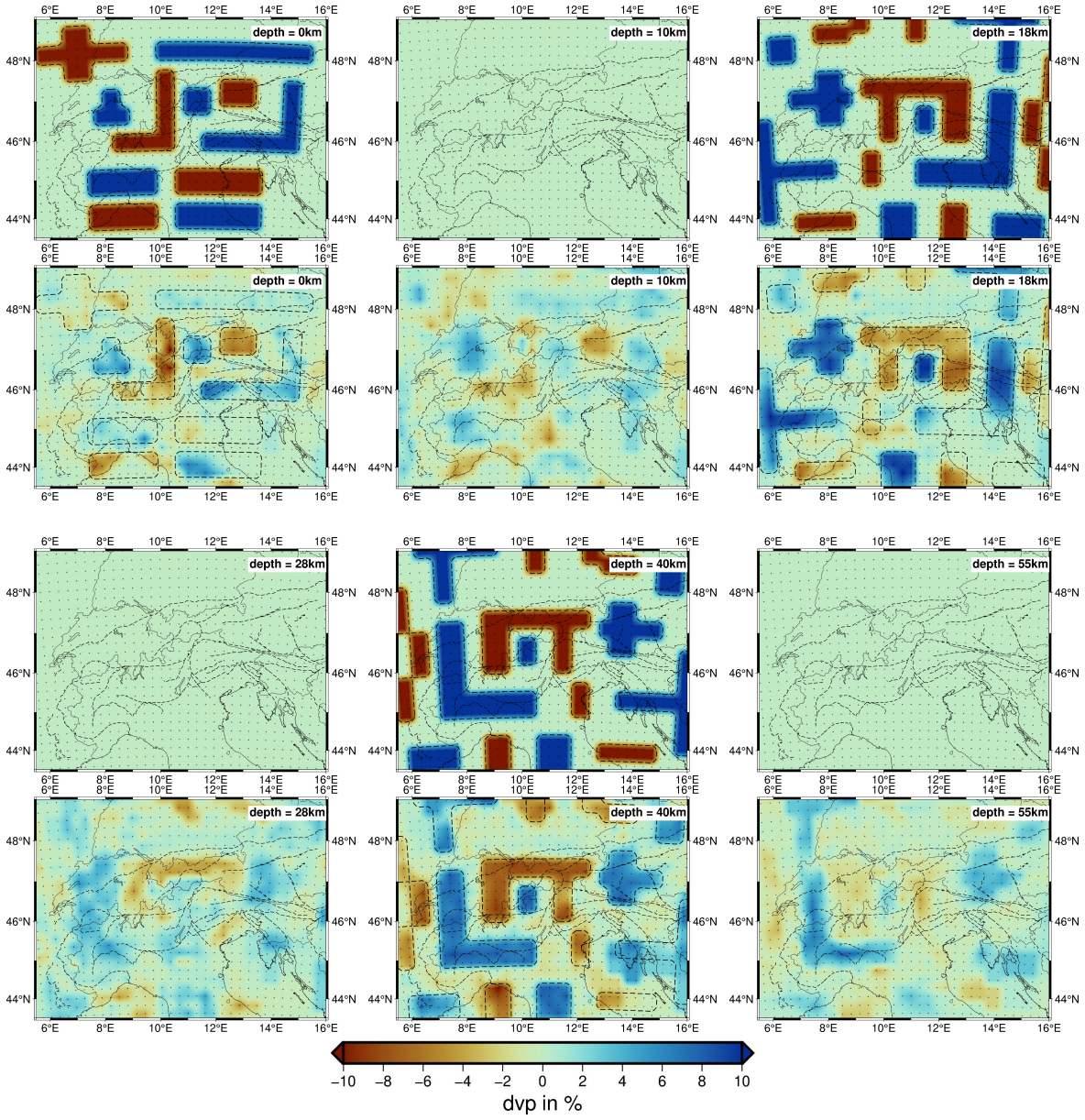

Figure B.14.: Reconstruction of irregular perturbations of $\pm 10\%$ in v_p in odd numbered layers. Synthetic models are displayed in the first and third row. Reconstructed models are shown in the second and fourth row. Dashed lines mark the outlines of synthetic anomalies.

C. List of Figures

D. List of Tables